Design and Applications of Multi-layer Meta-Optics

Anna Wirth-Singh

A dissertation
submitted in partial fulfillment of the
requirements for the degree of

Doctor of Philosophy

University of Washington

2024

Reading Committee:
Arka Majumdar, Chair
Mo Li
Matthew Yankowitz

Program Authorized to Offer Degree:
Physics

University of Washington

Abstract

Design and Applications of Multi-layer Meta-Optics

Anna Wirth-Singh

Chair of the Supervisory Committee:
Arka Majumdar

With rapid advancements in computational simulation tools and nanofabrication technology, the light-matter interaction can be explicitly controlled to create metasurfaces. Metasurfaces for optical applications are termed meta-optics, and they are composed of periodic arrays of sub-wavelength scatterers that modulate the phase of light. Numerous studies have leveraged the compact form-factor and sub-wavelength phase control for applications including imaging, beam steering, optical sensing, and optical computing. In particular, compression of multiple optics into a single meta-optical layer for compact, multi-functional imaging systems has been extensively studied. The challenges, limitations, and successes of single-layer meta-optics are well-understood, but extension to multi-layer meta-optics is less explored. This thesis presents developments in design and applications of single- through multi-layer meta-optics. First, we demonstrate singlet meta-optics for single-wavelength and broadband imaging at thermal wavelengths. Then, in a more complex application, we use a single layer of meta-optics to optically perform a convolution operation as part of a hybrid optical-electronic convolutional neural network for image classification. Using this hybrid approach, we estimate a reduction in latency and power consumption by over two orders of magnitude while maintaining 93% classification accuracy on the MNIST dataset. For doublet meta-optics, we demonstrate wide field of view imaging at both thermal and visible wavelengths. In the thermal range, we demonstrate 80° full field of view at 10 μm wavelength by combining a meta-optic with a 1 cm diameter external aperture. In the visible, we demonstrate

a wide field of view (greater than 60°) and large aperture (2.1 cm) eyepiece consisting of two layers of meta-optics for augmented/virtual reality and night vision applications. At the design wavelength of 633 nm, the meta-doublet eyepiece achieves comparable performance to a refractive lens-based eyepiece system. Finally, we present a meta-optics triplet for zoom imaging in the mid-wave infrared. By varying the axial distances between the optics, the meta-optic triplet achieves high quality imaging over a zoom range of 5×, with 50° full field of view in the widest configuration. These applications demonstrate the potential for meta-optics to replace conventional components in complex optical systems, and in particular we demonstrate the success of multi-layer meta-optics for wide field of view imaging.

TABLE OF CONTENTS

LIST OF FIGURES

ACKNOWLEDGMENTS

First and foremost, I most sincerely thank my advisor, Professor Arka Majumdar, for a wonderful PhD experience. Arka is deeply deserving of his many academic and professional successes. His scientific accomplishments are the result of decades of hard work, natural talent, and superhuman efficiency. Everyone in the research group works hard, but Arka works the hardest. I am always impressed by his personal attention to each project and frequent communication to check on updates, remove roadblocks, and provide direction. I also wish to emphasize how beneficial it was for me as a student to work on a broad range of topics and to have my very own projects from the first day I joined the lab. It has been an honor to work with Arka and I am sure he will continue to lead great research in any topic of his choosing.

Secondly, I thank my colleagues that contributed to this work. Postdoctoral researchers Johannes and Minho both contributed significantly by lending their valuable time, effort, and technical expertise. Johannes is an expert in his field and got me up to speed on meta-optics when I first joined the lab. Minho possesses a rare combination of technical competency, professionalism, and good spirit that make him an invaluable member of the group, and I am grateful to him for covering my projects while I was away on internship. It has been a pleasure to work with all my other colleagues on the meta-optics projects, including Rose, Romil, Max, Huang, Zhihao, Virat, Quentin, Zheyi, Saswata, and Aurelia. In particular, Quentin and Zheyi taught me nanofabrication, Huang wrote much of the code that we use every day, and Rose, Zhihao, and Aurelia have quickly developed their skills and are the future of our meta-optics at this lab. I am grateful to have worked with three exceptional Master's students - Erik, Vladimir, and Tina - who made lasting contributions to the group's

research by developing nanofabrication processes and setting up new laboratory equipment. I have many friends in the group including Hannah, David, Abhi, Arnab, Jayita, Ren, and Rui. I'm especially grateful to Hannah for her friendship and conference travel companionship.

In addition, I wish to thank the physics department at UW for their advising and administration of a wonderful PhD program. I especially want to thank my committee - Professors Mo Li, Matt Yankowitz, Lukasz Fidkowski, and Bruce H. Robinson - for their valuable time and attention as I've progressed in my academic milestones. I spent the initial years of my PhD in Subhadeep Gupta's ultracold atoms lab and am grateful for my time there. I have a great appreciation for the complexity of that experiment and gained a lot of experience and confidence working with lasers and optics. Deep is a kind person and careful scientist, and I am especially grateful for his grace and kindness when I chose to pursue my first internship. I am grateful to have learned from senior students Dan, Katie, Xinxin, and Tahiyat.

Many collaborators outside Arka's group have also contributed significantly to this research. In particular, it has been an honor to work with Professor Juejun Hu and Dr. Tian Gu at MIT on the wide field of view eyepiece project. Jinlin Xiang, from the CS department at UW, has been a patient and dedicated collaborator on the optical neural network projects. For MWIR and LWIR meta-optics, I've appreciated the consistent collaboration with Dr. Zachary Coppens and his team at CFD Research Corporation as well as Professor Ashok Veeraraghavan's group at Rice University. I would also like to thank the WNF staff for their dedication and expertise for maintaining the fabrication machines and training us students. I would like to especially thank Jean Neilsen, who has always been kind and patient with us as we use the laser writer.

I am grateful to have had two fantastic internship experiences during my PhD. Firstly, I would like to thank Gurkan and Urcan at Raytheon who introduced me to research on photonics topics. I enjoyed the subject so much that I took a class in the subject upon returning to UW, which was taught by Arka and hence led to my joining his lab. It was

also during this internship that I really learned how to read papers. Secondly, I would like to thank Xi and her team at Google. When I first started my PhD, I never would have imagined working in such a position, and I am so grateful for the opportunity to work with their optics team on such an exciting project within their hardware engineering team.

I grew up in a small town in West Virginia and, while I was lucky to have a number of educators in my early years who encouraged opportunities in physics and engineering, the world is quite a bit larger and more competitive than my hometown. I want to thank the physics department at my undergraduate institution, Case Western Reserve University, for a stellar academic preparation. CWRU brought me up to speed and then some. In particular, I'm grateful for being pushed to meet the high standards of Professors Lambrecht, Berezovsky, Hinczewski, Hinterbichler, Copi, Meckes, and Brown. I am also most grateful for my physics study group and friends - Megan, Steve, and Ted - for helping me along the way. Additionally, I benefitted greatly from a summer research opportunity at the University of Michigan with Professor Kuzmich and his student at the time, Huy Nguyen. Kuzmich's lab and CWRU instilled in me a work ethic and appreciation for efficiency that has been critical throughout my PhD and beyond.

Finally, I am fortunate to have the most wonderful parents, Douglas and Suzanne. They gave me all the tools I needed to reach where I am today, especially an excellent undergraduate education. They certainly had a large influence on my general well-roundedness as a person and I am most grateful for that.

I've saved my most sincere thanks for Jay, who has been with me throughout the entire PhD. Jay excels in all the areas I do not - understanding people, incentives, and the big picture - so with him I am able to navigate the world in a way I would not be able to do alone. I'm grateful that I can share my PhD interests, complaints, and everything in between with him. Thank you for the weekend adventures and everyday joys, and thank you for taking me along in life.

Chapter 1
INTRODUCTION

The light-matter interaction is one of the most extensively studied and well-understood areas of physics. Maxwell's equations for electromagnetic waves and Snell's law for ray optics have been applied for hundreds of years, unfazed by developments in general relativity, quantum mechanics, and high energy particle physics. Today, thanks to advances in nanofabrication techniques and computer simulations, this interaction can be explored at the nanoscale level and explicitly designed to create a new class of materials called metasurfaces. Aside from being scientifically interesting, metasurfaces have vast practical applications. Metasurfaces focused on optical applications are termed meta-optics.

1.1 Meta-Optics

Interest in meta-optics has surged since the mid-2010s [1] despite the physical principles underlying meta-optics being known for decades. What has changed in recent years and fueled interest in meta-optical systems is an improvement in nanofabrication techniques that enables the patterning of sub-wavelength structures. For visible meta-optics, this requires lithography capable of producing features down to 100 nm or smaller, which became possible with relatively recent developments in electron beam lithography. Since then, meta-optics has become an exciting field, with research efforts at large research groups at leading universities (Majumdar group at the University of Washington, Capasso group at Harvard, Hu group at MIT, Faraon group at Caltech, and many others), major technology companies (Apple, Google, and Meta), and numerous startup companies (Tunoptix and Metalenz). Commercial entities are pursuing meta-optics for their applications in compact cameras and augmented/virtual reality, and defense funding agencies are investing in meta-optics tech-

nologies for lightweight infrared optics and remote sensing applications.

Meta-optics consist of nanoscale pillars arranged on a flat surface. Each pillar, also called a "scatterer" or "meta-atom," can be thought of as a unit cell that locally imparts a phase shift to the incident light. By tuning the geometry and arrangement of the scatterers, the incoming light can be modified to achieve a desired global operation such as steering, lensing, encoding, or a combination of these. There are two key areas in which meta-optics offer distinct advantages over existing refractive optics: their compact form-factor and their sub-wavelength phase control.

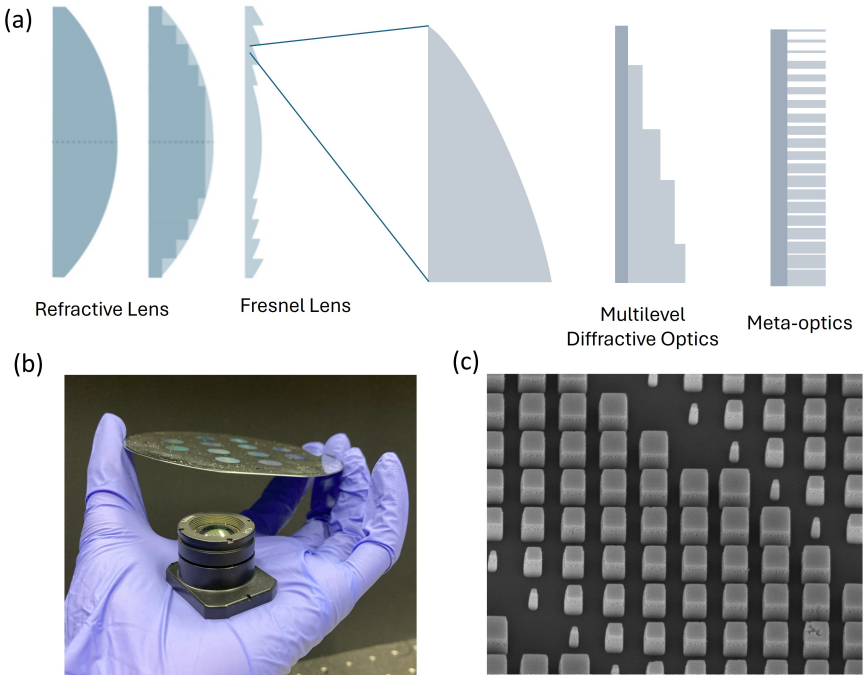

Figure 1.1: From refractive lenses to meta-optics. (a) Schematic illustration from traditional refractive optics (left), to Fresnel lenses (middle left), to multilevel diffractive optics (middle right), to meta-optics (right). (b) A photograph showing the thickness comparison between a compound refractive lens (resting on the hand) and a wafer filled with meta-optics, both for imaging at thermal wavelengths. (c) Scanning electron microscope image of exemplary meta-optics pillars.

The first key advantage of meta-optics over their refractive counterparts is their extreme lightness and thinness. The active layer of pillars is only on the order of the wavelength of the light. Including the substrate on which the active structure is supported, the meta-optic is only $100 - 500$ microns thick, which is orders of magnitude thinner than traditional refractive optics. The progression from thick refractive lenses to ultrathin meta-optics is illustrated in Figure 1.1. A refractive lens bends light according to Snell's law; at the interfaces between the high-index lens material and the low-index air, the light is bent according to the relative angle between the incident light and the interface. The key functional part of the lens, then, is the curvature of the surface. Recognizing this fact, Fresnel lenses were developed by dividing the lens into zones of similar curvature and removing the unnecessary bulk material in the middle.

Taking this idea further, these zones can be made smaller and smaller and the thickness can be discretized into levels for what is known as "multilevel diffractive optics". In multilevel diffractive optics, each phase level is typically larger than the wavelength of light, so ultra high resolution lithography is not required. However, producing multiple thickness levels does require multiple iterations of lithography and etching, so the number of phase levels is typically limited to ensure practical fabricability.

Meta-optics take a step further and reduce the thickness to a single level. Rather than adjusting the local refractive index by changing the thickness of the high-index material, the size and geometry of pillars within a single level is adjusted. One only needs to find a set of unit cells which can provide 0 to 2π phase coverage and then the phase can be fully controlled. To completely avoid higher-order diffraction, patterning with a period of $\lambda/2$ or smaller is required; however, in practice somewhat larger periodicity is acceptable without deleterious effects. Those in the meta-optics community argue that meta-optics fabrication is easier than that of multilevel diffractive optics because only one etching level is required; however, those in the multilevel diffractive optics community might equally argue that multilevel diffractive optics are easier to fabricate because the required spatial resolution is lower.

This point leads into the second significant advantage of meta-optics as compared to

both refractive optics and multilevel diffractive optics: the sub-wavelength phase control that enables multi-functional optics. With traditional optics, only smooth phase profiles can be implemented. With meta-optics, however, each unit cell can provide a different phase value for arbitrary pixel-by-pixel control of the phase, which does not at all have to be continuous. Further, the polarization- and wavelength-dependence of the unit cells can be tuned using the cell geometry for control of the light far beyond that which is possible with traditional (or multilevel diffractive) optics. This unique property of meta-optics has been leveraged for applications including edge detection, spectroscopy, and optical computing, just to name a few.

1.2 Thesis Outline

Throughout my time in Arka's group, I have worked on meta-optical systems for a variety of applications ranging from visible to thermal wavelengths. Upon reflecting on my work, I have concluded that my key contribution to the field is in the development of multi-layer meta-optic systems; that is, two or more layers of meta-optics stacked together. Having worked on single, double, and triple layer meta-optics, I think that this dissertation is an appropriate venue to further eludicate these findings.

As previously stated, one of the primary advantages of meta-optics is their compactness. Stacking multiple optics in series, in doublet or triplet configurations with some gap in between, does weaken the argument for thinness in meta-optics. However, a significant reduction in weight as compared to refractive lens systems is still achieved. Similarly to traditional refractive lenses, meta-optics can be stacked to improve performance or to achieve additional functionalities; in fact, most optical systems today are composed of several refractive elements. The field of single-layer meta-optics has matured and the fundamental concepts are now well-known. It is reasonable, then, to expand meta-optical studies to doublet and triplet configurations and see what can be achieved. Since singlet meta-optics can perform functions beyond singlet refractive optics, it is expected that multi-component meta-optical systems can also perform functions beyond the refractive counterparts with improved

performance.

Therefore, my dissertation is organized as follows. In Chapters 2 through 4, I present general meta-optics design, fabrication, and characterization, as these concepts and techniques comprise the foundation for the specific applications discussed later. While the design principles of meta-optics are agnostic to the wavelength, I pay particular attention to mid- and long-wave infrared (MWIR and LWIR) meta-optics fabrication and characterization. In Chapter 5, I discuss meta-optic singlets. I begin with the simplest meta-optics – hyperboloid meta-optics – which we made for testing our new MWIR fabrication and characterization facilities. I also discuss two more complex applications of singlet meta-optics: metalenses for broadband imaging, with a focus on our work at thermal wavelengths, and meta-optics as a front-end for a convolutional neural network. I discuss meta-optic doublets in Chapter 6. Doublet configurations are particularly useful for extending performance at wide FoV, and to that end I present a wide field of view optic for LWIR imaging and a wide FoV meta-optic eyepiece for augmented/virtual reality applications at visible wavelengths. I discuss some doublets that worked well, and some which did not work as well as expected, and hypothesize why certain inverse design techniques have thus far not produced doublets as successful as inverse-designed singlets. Finally, I report our demonstration of a MWIR triplet for dynamic zoom imaging.

Chapter 2
DESIGN AND SIMULATION

Design and simulation of meta-optics is uniquely challenging due to the vast spatial scales involved. The individual unit cells are sub-wavelength, but the larger array of those unit cells - and the distance over which light propagates after interacting with those unit cells - is on the order of 10^4 wavelengths. Therefore, designing meta-optics is a multi-scale problem and simulation tools operating at different scales is required. The design problem is typically broken into two steps: (1) designing the global phase profile and (2) designing a set of unit cells to physically realize that phase profile.

2.1 Global Phase Profile

The global phase profile determines what overall effect the optic has on the light. There are a few phase profiles that are analytically derived. Firstly, the hyperboloid phase profile is given by [2]:

$$\phi(r) = -\frac{2\pi}{\lambda}(\sqrt{r^2 + f^2} - f) \tag{2.1}$$

where r is the radial coordinate, f is the desired focal length, and λ is the design wavelength in free space. The hyperboloid phase profile is the solution for a flat lens to achieve diffraction-limited focusing at one wavelength and normal incidence. However, the focusing performance deteriorates quickly away from these conditions, making hyperboloid lenses typically unsuitable for applications requiring broadband, large field of view, or extended depth of focus applications.

Another commonly used phase profile is the quadratic phase profile given by [3, 4]:

$$\phi(r) = -\frac{2\pi}{\lambda}\frac{r^2}{f} \tag{2.2}$$

The quadratic phase profile trades off diffraction-limited resolution in favor of wider field of view (FoV).

Additionally, meta-optics can be modeled and optimized as phase masks in commercial ray tracing software. In Zemax OpticStudio, meta-optics are modeled as a Binary-2 type surface. The phase of this surface is parameterized by a radially-symmetric polynomial:

$$\Phi(\rho) = \sum_{i=1}^{N} A_i \left(\frac{\rho}{M}\right)^{2i} \tag{2.3}$$

where M is a normalization constant, ρ is the radial coordinate, and A_i are polynomial coefficients. The coefficients A_i are optimized for a particular quality such as spot size or wavefront error, over set incident wavelengths and angles of incidence.

For continuous phase profiles (with a well-defined derivative), the light can be propagated through the optic using ray tracing. Ray tracing is the standard method for modeling refractive optics; it is very fast, and commercial solvers (for example, Zemax and CodeV) are highly optimized, making the global phase mask design a quick and straightforward process. The bending angle that occurs as the rays intersect the optic are determined by Snell's Law. The generalized form of Snell's Law can be used to determine the bending angle in the case of meta-optics [5]:

$$n_i sin(\theta_i) - n_o sin(\theta_o) = \frac{\lambda}{2\pi}\frac{d\phi}{dx} \tag{2.4}$$

where the phase gradient $\frac{d\phi}{dx}$ determines the bending angle. Note the dependence on the wavelength λ, which leads to the strong chromatic behavior in meta-optics and other forms of diffractive optics. Refractive lenses may exhibit some chromatic aberration due to wavelength dispersion in the material refractive indices n, but this effect is small compared to the factor of $\frac{\lambda}{2\pi}$ that accompanies the phase gradient.

It is worth noting that Equation 2.4 is closely related to the differentiated form of the usual equation for for first-order diffraction (m = 1) in a blazed grating:

$$d \cdot sin(\theta) = m\lambda \tag{2.5}$$

where d is the distance between 2π phase resets. However in Equation 2.5, the phase gradient is assumed to be linear. That is, if $\frac{d\phi}{dx} = \frac{2\pi}{d}$, then Equation 2.4 can be rearranged to derive Equation 2.5.

The same equation may be rearranged to express the phase required to steer light to a desired angle. That is, the required phase ϕ required to bend light to desired angle θ is given by:

$$\phi(x) = k \cdot x \cdot cos(\theta) \tag{2.6}$$

where $k = \frac{2\pi}{\lambda}$ and x is the position on the phase mask.

Most often, smooth and continuous phase profiles are suitable for applications where meta-optics are replacing traditional refractive optics. However, part of the beauty and utility of meta-optics is their ability to realize completely arbitrary phase profiles on a pixel-by-pixel scale that is smaller than the wavelength. Inverse design, wherein a solution is optimized by working backwards from a desired result, leverages this ability of meta-optics to produce a solution which may be non-intuitive. The resultant phase profiles are generally not smooth and therefore do not have a well-defined derivative, so ray tracing fails to model them accurately. Wave-based propagation methods are required.

A number of wave-based propagation methods have been developed and can handle discontinuous phase profiles. (These methods can be used for continuous phase profiles as well, but they are usually significantly more time and memory consuming than ray tracing.) The "gold standard" simulation method is finite difference time domain (FDTD), which numerically solves Maxwell's equations in discretized steps in space and time. Aside from time and space discretization, it makes no simplifying assumptions and is therefore, in theory, completely accurate if sufficiently small steps are taken. However, this is a computationally costly approach and it is not typically used to model the propagation of light over more than a distance of approximately 100λ.

For propagation over intermediate and longer distances, electromagnetic fields are propagated with angular spectrum method [6, 7] or Rayleigh-Sommerfeld method. To propagate light from a phase profile using one of these methods, one typically defines an input electro-

magnetic field E_{in}. In most cases, this is a plane wave simply modeled as an array of 1's but it may be any complex field. As that complex electromagnetic field E_{in} passes through a meta-optic, it accumulates a phase delay according to the phase profile ϕ of the optic:

$$E_{out} = E_{in}e^{i\phi} \tag{2.7}$$

The resulting electric field E_{out} can then be propagated. Angular spectrum multiplies the field by e^{ikr} in Fourier space to quickly propagate an input field to the desired plane. The Rayleigh-Sommerfeld method is an integral which performs a convolution. I primarily used the angular spectrum method based on [7]. When using this method, one common mistake I have seen (both in my own work and the work of others) is insufficient padding around the simulation area. Due to the nature of Fourier transforms, any light that exits the simulation area on one side will reappear on the other side, which is a completely unphysical result! Care should be taken to check for this error during design. Some implementations of angular spectrum method have a filter to correct for this issue but padding the simulation area also works.

While not as fast as ray tracing, the angular spectrum method is fast enough to support inverse design of non-intuitive meta-optics. Inverse design works backwards from a desired solution to the phase mask of the meta-optics. In this area, I have worked with the Gerchberg-Saxton (GS) algorithm [8] and developed the lab's custom code in TensorFlow (TF) to design optics which produce a desired intensity pattern in a particular plane. You may wonder why one cannot simply back-propagate from the desired field, $|E_{out}|$, to E_{in} and then obtain the required phase of the field at the meta-optic plane. The reason is that the fields E_{in} and E_{out} are complex quantities, so one must consider both the amplitude and the phase to fully define the problem. After back-propagation, taking the phase of E_{in} neglects the amplitude information. In order to achieve the desired field E_{out} exactly as desired, one would need to encode both amplitude and phase information into E_{in}, which is a significantly more difficult task than encoding only the phase. Since it is most often the amplitude E_{out} that is the desired result and the phase of E_{out} will not be measured, the practical approach is

to iteratively solve for $|E_{out}|$ with some constant amplitude $|E_{in}|$ and variable phase. This is the basis of the Gerchberg-Saxton phase retrieval algorithm, which I used to design the meta-optics discussed in Section 5.4.

2.2 Unit Cell Design and Simulation

Once the desired global phase profile has been defined, the next step is to design a library of unit cells to physically realize that phase profile. The meta-optic unit cells interact with the light at a much smaller scale than the global phase mask, and therefore different physical models and simulation tools are required to design them.

There are two main types of meta-optics, classified by the mechanism by which the unit cells modulate the phase: propagation phase meta-optics and geometric or Pancharatnam-Berry (PB) phase meta-optics [9]. In PB-based meta-optics, the unit cell has some directionality associated with it and the rotation of the unit cell rotates the polarization. The unit cell may be a bar or fin-like pillar. Such lenses typically require circularly polarized incident light to work, so they cannot be used for ambient illumination unless a polarizer is introduced, which incurs some loss in signal. All main results in this thesis are based on the other type, propagation phase meta-optics, which are insensitive to polarization as long as the unit cell is rotationally symmetric. The pillars may have a simple square, rectangular, or circular cross-section or they may be more complex. In my work, I have used primarily simple square pillars. Square is preferred over circular because the fabrication machines process square shapes much faster than circular shapes, and this improvement becomes important in large aperture designs (circles or other curved shapes are discretized into many small squares). Complex pillars are commonly used in dispersion engineering to tune the chromatic effects of the unit cells (for example, see [10]). In my opinion, simple square pillars are the most practical choice for most meta-optics applications. Complex-shaped pillars require more extensive simulation, are more difficult to fabricate, and furthermore are less tolerant to fabrication errors.

For simple square pillars, designing the scatterer library typically involves choosing the

scatterer material, height, periodicity, and an appropriate range of pillar widths. The geometry of a pillar unit cell is illustrated in Figure 2.1a. The ultimate goal is to find a set of scatterers that cover 0 to 2π phase range while maintaining high transmission. The chosen material should have a high index of refraction ($n > 2$) for high contrast with the surrounding air ($n = 1$) but transparent at the wavelength of interest. We typically use silicon nitride ($n \approx 2$) for pillars in the visible wavelengths and crystalline silicon ($n \approx 3.5$) for pillars at infrared wavelengths.

The unit cell periodicity should be $\frac{\lambda}{2}$ or smaller to avoid higher-order diffraction and remain in a regime where the light experiences the net refractive index of the unit cell rather than diffracting off the pillar / air interface. If the periodicity becomes too large, then the phase is not as well controlled. Larger periodicity can be helpful on occasion since it increases the range of available pillar widths, potentially enabling greater phase coverage if the pillar height is constrained. The fabrication constraints must be kept in mind when setting the periodicity, since pillars or gaps that are too small are not possible to fabricate. The pillar height should be as tall as necessary to cover 0 to 2π phase range, but within fabrication constraints. If the pillars are too tall, they will likely fall over during etching. Ideally, the aspect ratio (pillar height divided by pillar width) should be kept below 7:1, but up to 10:1 is typically doable. For our all-silicon meta-optics in MWIR, we use deep reactive ion etching which produces scalloped sidewalls that have a tendency to undercut very tall, narrow pillars and cause them to fall over. Etching processes that produce very straight sidewalls may support higher aspect ratio pillars.

To understand intuitively how the unit cell works, one can think of the unit cell like a waveguide of length L and refractive index n. As light passes through such a waveguide, it accumulates a phase delay

$$\phi = \frac{2\pi n L}{\lambda} \tag{2.8}$$

Therefore, we can approximate the phase delay accumulated using the effective refractive index of the unit cell. The approximate effective refractive index is

$$n_{avg} = \frac{n_{pillar}A_{pillar} + n_{air}A_{air}}{A_{total}} \tag{2.9}$$

where A_{pillar} and A_{air} are the cross-sectional areas of the pillar and surrounding air, respectively.

This provides an intuitive understanding of the meta-optic unit cell – as the fill factor of the high-index pillars becomes larger, the effective refractive index increases, causing more phase delay. However, this effective refractive index approach is typically not sufficient to capture the more complex behavior arising from the interfaces between the pillar and the air. Hence, numerical simulators are needed. These include rigorous coupled wave analysis (RCWA) and finite difference time domain (FDTD).

We most commonly use RCWA to calculate the unit cell phase and transmission. RCWA is a fast, semi-analytic method to simulate the phase or transmission through a stack of materials. Specifically, we most often use the S4 implementation [11]. On the other hand, FDTD iteratively solves Maxwell's equations in small steps in space and time. It is theoretically 100% accurate if infinitely small steps are used. While accurate, FDTD simulations are computationally costly, so they are typically reserved for complex structures and final verifications. Lumerical provides an excellent unit cell starting simulation in their application library, although I recommend changing the boundary conditions from periodic to Bloch in order to properly model off-axis illumination.

Especially for simple pillars, RCWA and FDTD results are nearly indistinguishable. In Figure 2.1b, I plot the phase and transmission calculated by both RCWA and FDTD for an example scatterer (in particular, this one is 1.5 μm tall cSi square pillars on sapphire substrate at 3.4 μm wavelength). The phase calculated by RCWA (solid lines) and FDTD (circular markers) are in close agreement. There is some difference in the transmission, which may be due to the fact that the entire substrate is not modeled in FDTD. The transmission is much less consequential to the performance of the optic than the phase. For reference, I also plot the phase calculated from the approximate analytical expression Equation 2.8 as a red dashed line for comparison. The analytical expression agrees with RCWA and FDTD

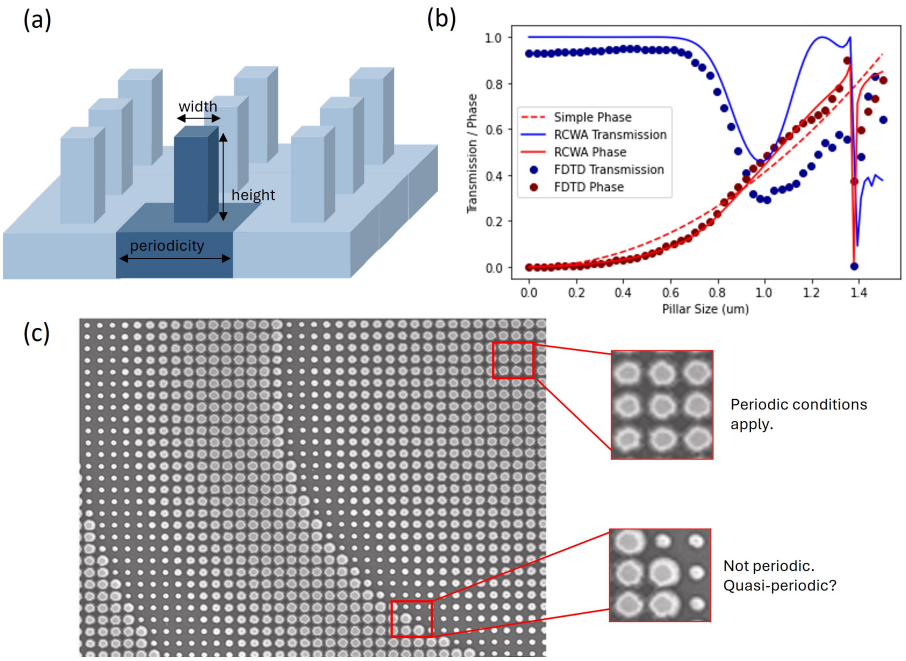

Figure 2.1: Unit cell simulation. (a) Schematic highlighting a single unit cell (dark blue) in an arrangement of unit cells (light blue). (b) Simulated phase (red, in units of 2π) and transmission (blue) for an exemplary unit cell for different simulation methods. The RCWA and FDTD simulations are in good agreement. (c) Scanning electron microscope image of a typical meta-optic, with insets illustrating the local periodicity.

quite well near the endpoints of the pillar width range, where the unit cell is either mostly pillar or mostly air. In the middle, the interface between the two becomes important so the simple approximation breaks down.

Finally, it is important to note an assumption which is commonly applied to make these numerical simulations tractable. In simulating the unit cell using RCWA or FDTD, periodic boundary conditions are commonly applied; that is, an infinite array of identical pillars is simulated, rather than a single unit cell. This is called the "local phase approximation" since it assumes that the adjacent (local) pillars are identical. This is an excellent approximation for slowly-varying phases where the geometry of the adjacent pillars is changing slowly, but

it may break down when they change suddenly, such as near a 2π phase discontinuity. This is illustrated in Figure 2.1c; across much of the surface, the pillars are indeed locally periodic, but this assumption is generally not true near the phase wraps. In Zhelyeznakov et al. [12], we show that slightly higher focusing efficiency is achieved when a lens is designed not using the local phase approximation. However, we almost always use this approximation when designing meta-optics and the experiment and theory usually agree very well, so we suggest this approximation is valid in most situations.

2.3 GDS File Generation

For single-wavelength meta-optics, determining the arrangement of pillars required to physically realize the desired phase profile is only a matter of mapping between desired phase and pillar width using the simulated results from RCWA or FDTD. That being said, this task is not trivial, especially in the case of large aperture meta-optics involving many scatterers. For example, a 1 cm diameter visible meta-optic sampled at 350 nm periodicity contains on the order of 10^8 unit cells. If no measures are taken, this becomes an incredibly memory-hungry task. Much of my GDS generation code is based on former PhD student Luocheng Huang's code, who I would like to sincerely thank for this.

A flowchart of the GDS generation procedure is shown in Figure 2.2. For radially-symmetric meta-optics, it is best to work with only a quarter of the full aperture and utilize symmetry at the end to bring the design back to full aperture. When working with a quarter aperture, I define 2D arrays xx and yy which hold the x and y coordinates of each point in the 2D aperture. Another array of the same size and shape holds the phase data, where the index of the array indicates the location of each pillar and the value at that index gives the phase. If the phase profile is described by an equation, it can be evaluated from xx and yy. If the optic was inverse-designed, the phase mask values would just be loaded (from a text, numpy array, or Matlab file) while ensuring that xx and yy are the same size and sampled at the same periodicity as the loaded phase mask. To prepare the phase mask for mapping, it should be wrapped modulo 2π.

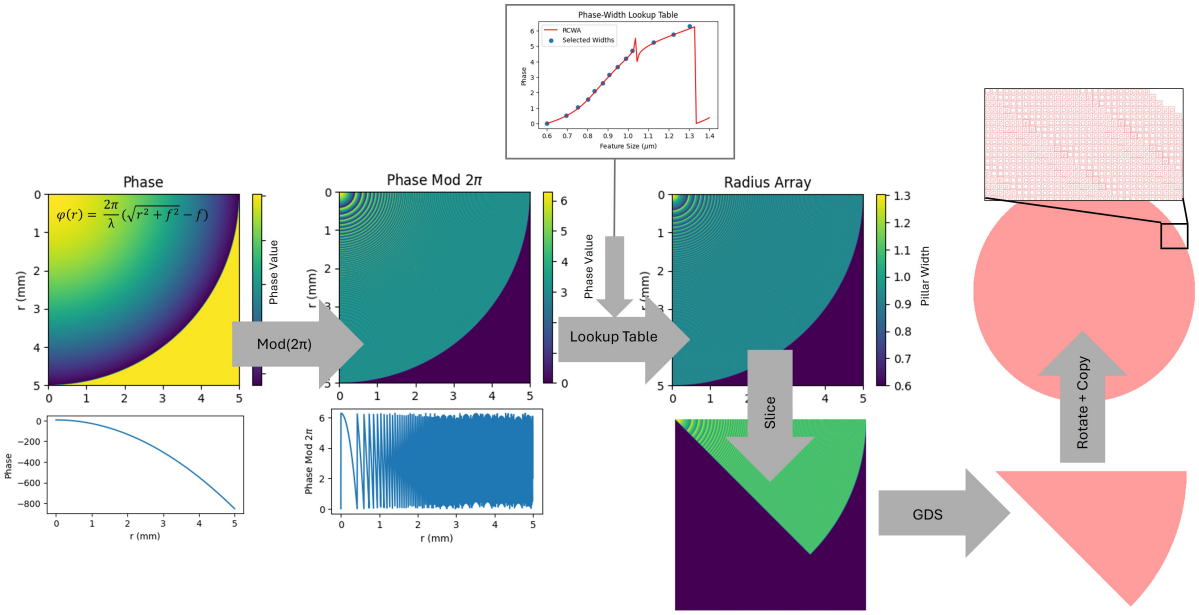

Figure 2.2: Meta-optics design flowchart. Beginning from the left, a phase mask is wrapped modulo 2π. To reduce computation time, only a quarter of a circular mask is used for radially symmetric designs. Then, the phase-width lookup table (obtained from RCWA or FDTD simulations) is used to map from phase to pillar width, resulting in an array of pillar widths. This array is further reduced to a 1/8 slice to reduce file size. A GDS file is written by iterating through the array and building the structure according to the pillar widths in the radius array. Finally, the 1/8 slice is appropriately rotated and copied to return the optic to a full circle.

The RCWA simulations typically contain 100 pillar widths covering the full range of available pillars. We typically select a subset of 10-20 pillar widths to comprise the pillar library. The chosen pillars should provide 0 to 2π phase shift in approximately equal steps while maintaining high transmission. Widths near abrupt phase gradients or dips in transmission (the two are typically correlated) are generally avoided. It is also good practice to select pillars from a range where the phase-width relationship is approximately linear - this supports resiliency to fabrication imperfections. Discretizing into 10-20 phase levels (and

accordingly, discrete pillar widths) reduces the GDS file size and computation time in the phase-width mapping step, outlined below.

After the pillar library has been chosen, I iterate through the phase mask array and convert it to an array which holds the desired pillar widths (also called "radius array"). The steps below are iterated over every element in the phase mask array to convert it to the radius array[1]:

1. Calculate the phase distance between the value in the phase array and the 10-20 discretized phase values in the lookup table.

2. Search through the difference list and find the smallest phase difference (this is where it is helpful to discretize into fewer pillar widths! Otherwise, searching through the list to find the one with the least phase error can take a long time.)

3. Select the pillar width corresponding to that smallest phase error.

The above step of converting the phase array to radius array is typically the slowest part of this process. If the radius mask is square in shape and a circular optic is desired, the array is multiplied by a binary mask to circularize it. Additionally, I typically multiply by another binary mask at this point to reduce the quarter to a one-eighth circular slice.

Finally, the GDS file is generated using the gdstk package (https://heitzmann.github.io/gdstk/ [13]). The gdstk package is the newer (and much faster!) version of gdspy, although their usage is similar. First, a library of unit cells is made corresponding to the selected pillars, with the name of the cell being the width (or some other unique parameterization) of the pillar. Then, I iterate through the radius array and place the required cell at each location, with the cell's origin being set by xx and yy. Once this has been accomplished for the 1/8 slice, that slice is appropriately rotated and copied to return to the full circular aperture.

[1]Dispersion-engineered meta-optics follow essentially the same process, but dispersion engineering involves calculating phase difference for each wavelength and attempting to minimize the error at all wavelengths simultaneously by drawing from a large library of pillars with varied wavelength response.

In the early days of my PhD, I tried several methods to produce a GDS of minimal size, and the method described above is the most efficient I have encountered. As an example, the GDS file size of the 3 cm diameter LWIR lens discussed in Section 6.1 is 2.7 Gb when written "brute force." Discretizing from 100 to 10 pillar widths reduces the file modestly - to 1.8 Gb (the discretization is more useful to increase speed during the phase-width mapping, and it is also greatly improves file conversion speed on the lithography machines). The more significant reduction comes from utilizing the symmetry of the design - once a complete quarter or an eighth is made, it takes only 1 kB to make a rotated and copied version. Accordingly, using 8-fold symmetry reduces the 1.8 Gb file by a factor of 8 for a final file size under 250 Mb. While these steps may seem cumbersome, they are well worth the factor of 10 reduction in file size.

In order to make extremely large meta-optics within limited RAM, it is possible to generate the files section-by-section. In this case, all of the steps above can be placed in a loop and evaluated in spatial sections, from the center of the optic outwards. Combining the sections can be done within KLayout using much less RAM than generating the entire file at once. For optics that are not rotationally symmetric (for example, the ONN optics in Section 5.4), I am not aware of any helpful size-reducing measures. However, the design of such optics is computationally limited just as the generation of the GDS files is, so generating a GDS for non-symmetric optics is typically not too cumbersome.

Chapter 3

FABRICATION

In many ways, nanofabrication is like baking a cake. You follow a recipe, load a device into machines for a set amount of time, try to avoid contaminating your product, and if you miss a key ingredient you may get an unexpected result. Someone experienced in nanofabrication - like an experienced baker - knows what substitutions can be made and where short cuts can be taken, but for the beginner it is best to stick to the recipe as closely as possible.

My contribution to the lab's fabrication efforts focused primarily on MWIR and LWIR meta-optics fabrication with direct laser write lithography. In this section, I provide a brief overview of meta-optics fabrication techniques and discuss the MWIR / LWIR processes in greater detail.

3.1 Meta-optics Fabrication Overview

The overall fabrication process flow is largely dependent on the lithography method, typically one of the three summarized in Table 3.1. Of the three methods, electron beam lithography (EBL) provides the highest resolution. Many new foundries achieve resolution down to a few tens of nanometers with this method, although we typically fabricate meta-optics under conditions that promote faster writing at the expense of limiting the resolution to around 80 nm. Still, this resolution is sufficient for all but the most complex meta-optics designs at visible wavelengths. The drawback of EBL is its very high cost and slow writing speed. Due to this high cost and concerns about machine stability over extended writes, we typically limit the write area to a maximum of 1 cm^2. To fabricate larger aperture optics, another method is required.

Direct laser writing uses a laser beam - usually in the UV range - to expose the photoresist

Table 3.1: Meta-optics lithography methods.

Method	**Resolution**	**Max Aperture**	**Cost**	**Scalability**
Electron Beam	80 nm*	1 cm	$$$	Very Low
Laser Writing (HiRes)	350 nm	25 mm	$	Low
Laser Writing (4 mm)	1000 nm	100 mm	$	Medium
DUV Stepper Lithography	350 nm	21 mm per die**	$$	Very High

* Sub-20 nm resolution is possible using electron beam lithography. However, for meta-optics, we typically increase the electron beam current for faster write time at the cost of slightly lower achievable resolution.

** Multiple dies can be aligned and stitched together for larger aperture overall.

directly on a substrate, rather than an electron beam as in EBL. Laser writing is orders of magnitude faster and less expensive than EBL, but its resolution is limited to the wavelength of light being used. New foundries are continually pushing deeper into the ultraviolet to achieve higher resolution. At our facility, the Heidelberg DWL-66+ is specified to achieve 350 nm resolution in its high resolution ("HiRes") write mode.

Deep ultraviolet (DUV) stepper lithography is another UV-light based method. In contrast to direct laser writing - wherein the laser writes the pattern directly on a substrate - DUV stepper lithography utilizes a photomask that is flooded with illumination to transfer the pattern from the mask onto the substrate below. The machine can "step" from substrate to substrate in quick succession. After the initial investment of a high-resolution photomask, DUV stepper exposures are very fast. Therefore, DUV stepper lithography is a much more scalable approach than direct laser writing, and often can achieve higher resolution as well. At this time, a DUV stepper is not available at our fabrication facility, but we have collaborated with the UCSB Nanofabrication Facility to fabricate some optics (see Section 6.2) with an ASML 5500 DUV Stepper. In this particular machine, the maximum exposure area (also called "die size") is 21 mm square. It is possible to stitch multiple dies together, but

care must be taken to ensure die-to-die alignment. This approach has been used to fabricate ultra large area visible metalenses [14].

I will briefly mention one other method with promise to produce high-resolution meta-optics at scale. Nanoimprint lithography utilizes a resin that is shaped using a mold and cured using UV illumination. Similarly to DUV lithography, the approach is scalable to mass production with the initial investment of a high-quality mold that could be fabricated using more expensive methods, for example EBL and dry etching. However, this approach has not widely been used for metalenses because (a) the refractive index of available resins is low (around 1.5) and (b) the aspect ratio is limited to around 3:1 due to the somewhat viscous nature of the polymer. While these two issues compound to make it quite difficult to achieve the required 0 to 2π phase shift to efficiently modulate the light, these practical issues are both solvable with advancements in material science. If a high-index polymer supporting high aspect ratio can be developed, I believe that nanoimprint lithography is a promising method for mass production of metalenses.

3.2 MWIR / LWIR Meta-optics with Heidelberg DWL-66+

The group's first MWIR meta-optics were fabricated in crystalline silicon (cSi) on sapphire substrate using e-beam lithography. This approach was chosen initially because the group already had experience working in this platform. However, e-beam lithography is very expensive compared to Heidelberg lithography, the e-beam process requires a hard mask that adds significant time and complexity to the fabrication process, and cSi on Sapphire wafers are extraordinarily expensive ($>$ \$1500 per wafer). Furthermore, e-beam lithography is suitable only for meta-optics 1 cm in diameter or less due to the slow write time. These factors motivated our decision to develop a more sustainable process using Heidelberg direct write lithography in all-silicon platform.

Former PhD student Zheyi Han had previously developed a successful process for LWIR meta-optics using Heidelberg. In addition to the time-saving benefits of the laser writer instead of the e-beam lithography tool, the Heidelberg process has the additional benefit of

directly using photoresist as a mask for etching rather than requiring a hard mask. However, adapting Zheyi's LWIR process for MWIR optics still required significant process development. This development was greatly assisted by the efforts of MS student Vladimir Yarmolik and PhD student Rose Johnson, as well as the WNF staff tool owner Jean Nielsen.

For LWIR, the minimum required feature size (smallest pillar or smallest gap) is around 1.2 μm. For this, the 4 mm write mode with 1 μm minimum feature is sufficient resolution. In our first attempt to develop a process for MWIR, we attempted to push the resolution of the 4 mm write head to smaller feature size - around 800 nm. However, we found that 1 μm was a hard limit - we were unable to push the resolution any further. Therefore, we focused our efforts on developing a new process with the HiRes write head, specified to achieve resolution as good as 300 nm, but 500 nm minimum is sufficient for MWIR meta-optics. [1]

To promote higher resolution, it was necessary to switch to a thinner photoresist. We used AZ1512 with the 4 mm write head, which results in a resist layer that is around 1.2μm thick. Thicker photoresist is advantageous because it provides a thicker mask for etching, and the additional thickness renders it more resilient to small variations in exposure dosage. However, photoresist generally only supports a spatial resolution of about the same amount as the resist thickness, so thinner resist is required to achieve higher resolution. We tested two thin photoresists, AZ 701 11cps and AZ 1505, and achieved better performance with AZ1505. When spun at 4000 rpm, its thickness is around 400 nm, which supports our resolution requirements. It is critical to note that both AZ 1512 and AZ 1505 are positive-tone photoresists, meaning that the exposed area develops away after exposure. Therefore, rather than write the pillars themselves, we need to write the area around the pillars. This can be accomplished by pre-inverting the GDS file or by inverting the file in Heidelberg

[1] In another effort, we worked to develop a HiRes process for ultra large aperture visible meta-optics in silicon nitride. Zheyi worked on this, then I worked on it, and finally MS student Erik Petersen made substantial progress. The process that emerged was quite complex, involving an anti-reflective coating to promote higher resolution and a hard mask that needed to be etched away. There were three separate etching steps to etch the hard mask, the anti-reflective coating, and finally the silicon nitride pillars. Ultimately, we struggled to achieve consistent results and good etching quality and the process was rarely used. This experience led to my initial hesitation in developing a HiRes process for MWIR, but with a much simpler process we had much better results with the HiRes write head.

during the conversion, but it is preferable to pre-invert the GDS during file generation to minimize the chances for errors to occur.

To determine the optimal exposure parameters on the Heidelberg tool, we perform an intensity / focus matrix. There are four parameters that are typically adjusted to achieve good exposure:

- Laser Power: This sets the maximum power of the laser. A typical value is 120 mW, and a high value would be around 200 mW. It is preferred to set the power slightly higher than required and use a lower intensity filter to reduce the power at the sample rather than adjust the laser power during the scan because the tool must re-calibrate every time the power is adjusted.

- Transmission: This filter controls the laser power by orders of magnitude. There is generally one setting that works for a particular substrate and photoresist, and all other settings will not work at all. It should be set to 1 for AZ 1505 (this resist requires very little intensity to expose) and 5 for AZ 1512 (a thicker resist that requires more laser intensity).

- Intensity: This is a finer way to tune the laser intensity at the sample. It is coupled to laser power; for example, 80% intensity setting at 100 mW set power should be equivalent to 100% intensity setting at 80 mW set power.

- Focus: This sets a focus offset for the write head. Typical values are between -30 and $+30$.

In an intensity / focus matrix, the laser power and transmission settings are fixed while the intensity and focus settings are swept over a range of values, creating a 2D matrix. A small design (less than 1 mm) is typically used for this purpose.

Additionally, there are two focus mode options on the Heidelberg: pneumatic and optical focus. Pneumatic focus reads the pressure coming from a puff of air directed towards the

sample to determine the distance to the sample. Pneumatic mode is not related to the optical properties of the substrate, so it may be preferred for highly reflective or highly transparent substrates that may confuse the optical autofocus. Pneumatic is also the safest mode to use because the autofocus is less likely to fail and cause a head crash. On the other hand, optical focus mode is more precise, which enables higher resolution. We use optical focus mode in the developed MWIR processes.[2]

Table 3.2: MWIR Fabrication Process with Heidelberg DWL-66+.

Step	**4 mm Process**	**HiRes Process**
HMDS Prime	Standard HMDS in lithography bay	Standard HMDS in lithography bay
Photoresist coat	AZ 1512 at 3000 rpm	AZ 1505 at 4000 rpm
Bake	100C for 90 seconds	100C for 90 seconds
Exposure*	No CD bias, T 5, P 120, I 100, F -30	CD bias -100nm, T 1, P 120, I 40, F -10
Bake	100C for 60 seconds	100C for 60 seconds
Develop	AZ 726 60-90 seconds	AZ 726 60 seconds
Inspect	Nikon or Keyence	Nikon or Keyence
SPTS-DRIE Etch	Etch to desired depth at 330 nm / loop	Etch to desired depth at 330 nm / loop
Photoresist strip	Oxygen plasma	Oxygen plasma

* These values were optimal as of April 2024; they do drift over time. The CD bias refers to the critical dimension bias; this setting shrinks or enlarges all features by a set amount. T refers to the transmission setting, P refers to the power setting (in mW), I refers to the intensity setting (%), and F refers to the focus setting (%).

After exposing the photoresist, it is developed in a compatible developer (AZ 726 MiF or AD-10) for 60 to 90 seconds. The exposed photoresist is developed away, leaving a pattern of

[2]In one write using optical focus in HiRes mode, the write head encountered a flake of material on the substrate that caused it to defocus and it failed to recover, ruining the remainder of the write. Pneumatic focus is likely more resilient to blemishes on the wafer. However, we only once observed complete failure to recover after defocus.

hardened photoresist on the surface. The photoresist is typically not sufficient to be used as an etching mask in inductively coupled plasma fluorine (ICP-F) etching due to low selectivity between the photoresist and the target silicon. Thankfully, selectivity in deep reactive ion etching (DRIE) is high - around 20:1 - which supports etching with photoresist only as a mask. This greatly simplifies the etching process. Since sidewall structure is critical for small pillars, we modified the default DRIE recipe to have a higher polymer ratio for better protection of the sidewalls at each loop. The final recipe etches silicon at a rate of 330 nm per loop. After etching, any remaining photoresist is removed with oxygen plasma and then the meta-optic is complete. The general fabrication process is depicted in Figure 3.1 and the steps are described in greater detail in Table 3.2. [3]

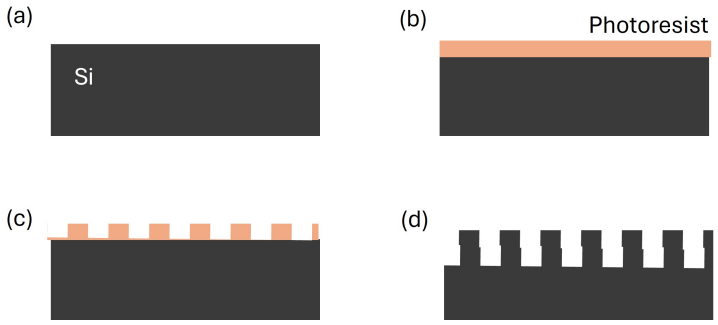

Figure 3.1: Fabrication process diagram. (a) We begin with a double-side polished silicon wafer. (b) A photoresist layer is applied via spin coating. (c) The photoresist is patterned via exposure with a laser writer and developed. (d) The pillars are etched to the desired thickness and remaining photoresist is stripped.

While the HiRes write head on the Heidelberg writes significantly faster than e-beam lithography, it is not fast enough to write an entire wafer. The HiRes write head writes at approximately 0.86 cm^2 per hour, or 1 hour and 10 minutes for a 1 cm aperture optic. In order to cover an entire wafer, we estimate an intractable write time of 92 hours. In

[3]In particular, the wafers I use are ID No. 2345 from UniversityWafer.

comparison, the 4mm write head writes at 14.4 cm^2 per hour, or only 5 minutes for a 1 cm aperture optic. A full wafer can be written in approximately 6 hours. Therefore, for large optics (greater than 25 cm^2), we designed a low-resolution scatterer to accommodate the 1 μm resolution of the 4 mm write head. These scatterers are presented in Section 5.1 along with a discussion of the trade-offs. Due to larger periodicity, the phase control and transmission are poorer, which results in a lower efficiency optic. At the same time, the lower periodicity enables larger aperture, which can increase optical performance.

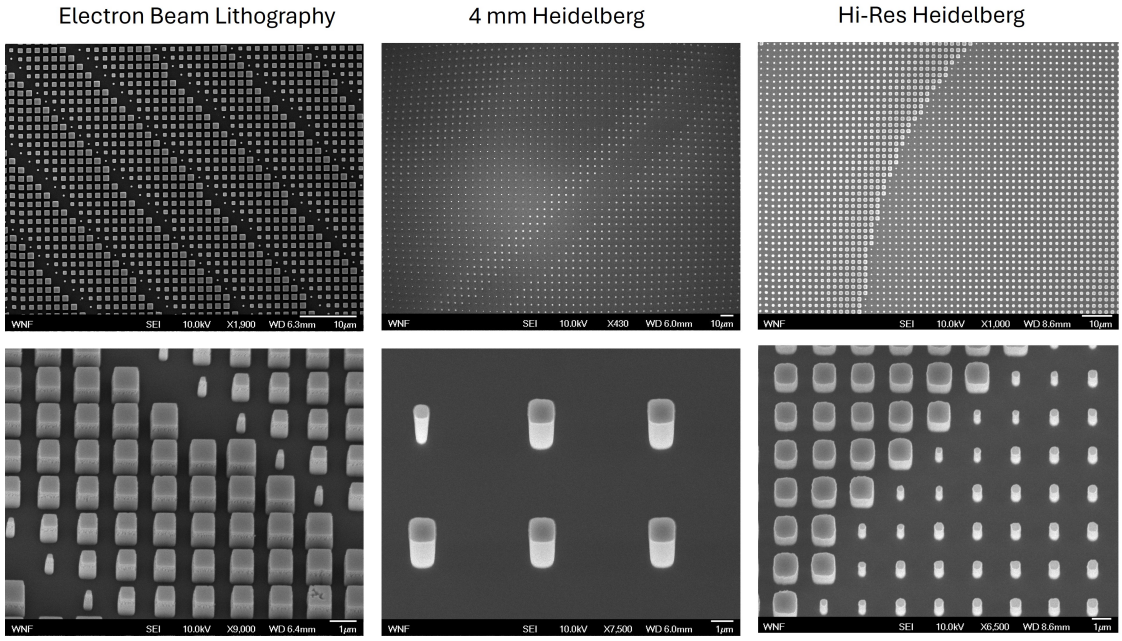

Figure 3.2: SEM images of fabricated MWIR meta-optics using e-beam lithography (left), the 4mm Heidelberg process (middle), and the HiRes Heidelberg process (right).

In Figure 3.2, we show scanning electron microscope (SEM) images of fabricated MWIR meta-optics using three methods - cSi on sapphire with e-beam lithography, all-Si with the 4mm Heidelberg process, and all-Si with the HiRes Heidelberg process. The highest fabrication quality is achieved with e-beam lithography, as evident by the sharp corners and smooth sidewalls of the pillars. The Heidelberg-written pillars exhibit somewhat rounded

corners, but still reasonably good fabrication quality. The height of the pillars is 1.5 μm for e-beam, 7.9 μm for the 4 mm Heidelberg, and 3 μm for the HiRes Heidelberg.

3.3 ZnS Antireflection Coating

While the all-silicon platform has many benefits, including CMOS-compatible fabrication and high availability, the large refractive index contrast results in significant Fresnel reflection loss. Applying an anti-reflection coating is an effective way to reduce this loss, with zinc sulfide (ZnS, n = 2.2 at 10 μm) being the preferred choice at thermal wavelengths [15]. Recently, it has been shown that such a single layer of ZnS coating increases the efficiency of a germanium-based meta-optic from 75% to 97% [16].

Following this idea, we developed a process to sputter coat ZnS as an anti-reflection coating on our LWIR meta-optics. To use it as a standard quarter-wave anti-reflection coating, we target a thickness of $\lambda_0/(4n) = 1.1$ μm. Following the recommendation of the sputter tool owner, we sputtered at RF power of 120W at room temperature. To establish the deposition rate, I covered portions of the wafer with vacuum tape and peeled off to form a sharp edge that could be measured. After an initial 20 minute test, we established the etching rate to be 3.5 nm per minute. Therefore, we sputtered the product wafers for 5 hours, 14 minutes to achieve the target thickness of 1.1 μm.

To characterize the effectiveness of the ZnS coating, I used Mo Li Lab's Fourier Transform Infrared Spectroscopy (FTIR) machine to measure the transmission through coated and uncoated areas on a wafer. These results are shown in Figure 3.3. The measurements demonstrate a 20% improvement in relative transmission at the design wavelength. This is consistent with optical measurements; by imaging the hot plate through the wafer with the LWIR camera (see Figure 3.3), we estimate the transmission to be 50% without the ZnS coating and 75% with the coating, which is a significant improvement. In this case, due to the long sputter time required, we coated only one side of the wafer. Further improvement would be expected if both sides of the wafer were coated.

However, despite significant improvement in the measured transmission through the

wafer, notable improvement in imaging quality was not observed. The ZnS coating may perhaps increase the signal to noise ratio slightly, but it does not seem to significantly improve the imaging performance and therefore we did not pursue this application further.

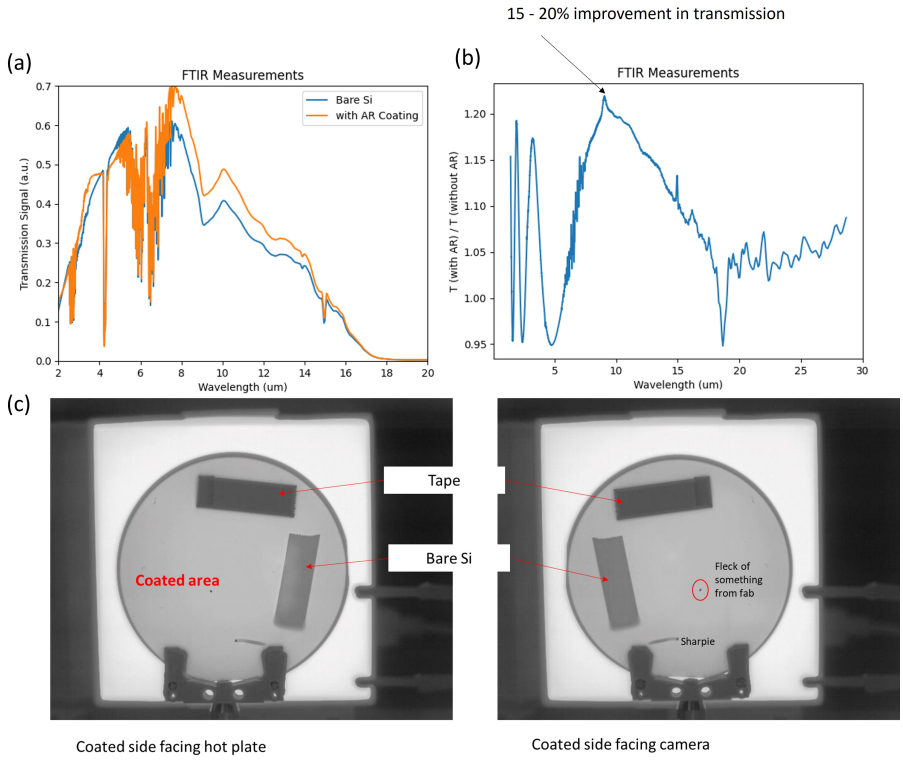

Figure 3.3: ZnS antireflection coating characterization. (a) Absolute transmission spectra of bare Si (blue) and Si with the ZnS coating (orange). (b) Relative transmission spectra showing a 20% improvement in transmission at 10 μm wavelength. (c) Optical characterization showing higher transmission in the ZnS-coated area versus the bare Si. A piece of tape, present during deposition, has been removed to reveal the bare Si. Bare Si is also visible at the edges of the wafer because it was blocked by the wafer clamp during deposition.

3.4 Tolerance to Fabrication Errors

In myself and others, I have observed that newcomers to the field of meta-optics often worry about the error which may be incurred by not matching the desired phase with the unit

cell exactly due to fabrication errors. I would like to alleviate this concern by describing a number of factors which fortunately support robustness in meta-optics, especially those with smooth phase profiles.

Firstly, it is not the absolute phase value of the unit cell that matters – it is the phase gradient, or the relative phase difference between different parts of the surface which cause the bending of light. Therefore, fabrication errors which affect all the pillars equally – by making them all slightly taller or shorter, or narrower or wider – simply adds a constant offset to the phase, which does not affect the performance of the optic. Secondly, it has been shown that discretizing into only 4 phase levels can still provide a Strehl ratio of 60% [17]. This equivalently means than an average phase error of 15% on each pillar is expected to produce $> 60\%$ focusing efficiency.

To illustrate the resiliency of meta-optics, Figure 3.4 shows a series of microscope images of fabricated metalenses and the corresponding image achieved with them. In the case of (c), nearly 40% of the pillars fell over due to non-optimal fabrication conditions, but the lens still works surprisingly well. The image is dimmer relative to the background, indicating reduced focusing efficiency, but it still produces an image. Lenses with smooth phase profiles are likely more resilient to fabrication inconsistencies than those with irregular phase profiles. In my experience, unless the fabrication errors are quite severe, fabrication issues have not been the primary reason an optic has not worked. Meta-optics more typically fail due to some design error. In one case, I found that a particular optic did not work because the designer made it for crystalline silicon (n = 3.5), but the fabricator made it in silicon nitride (n = 2).

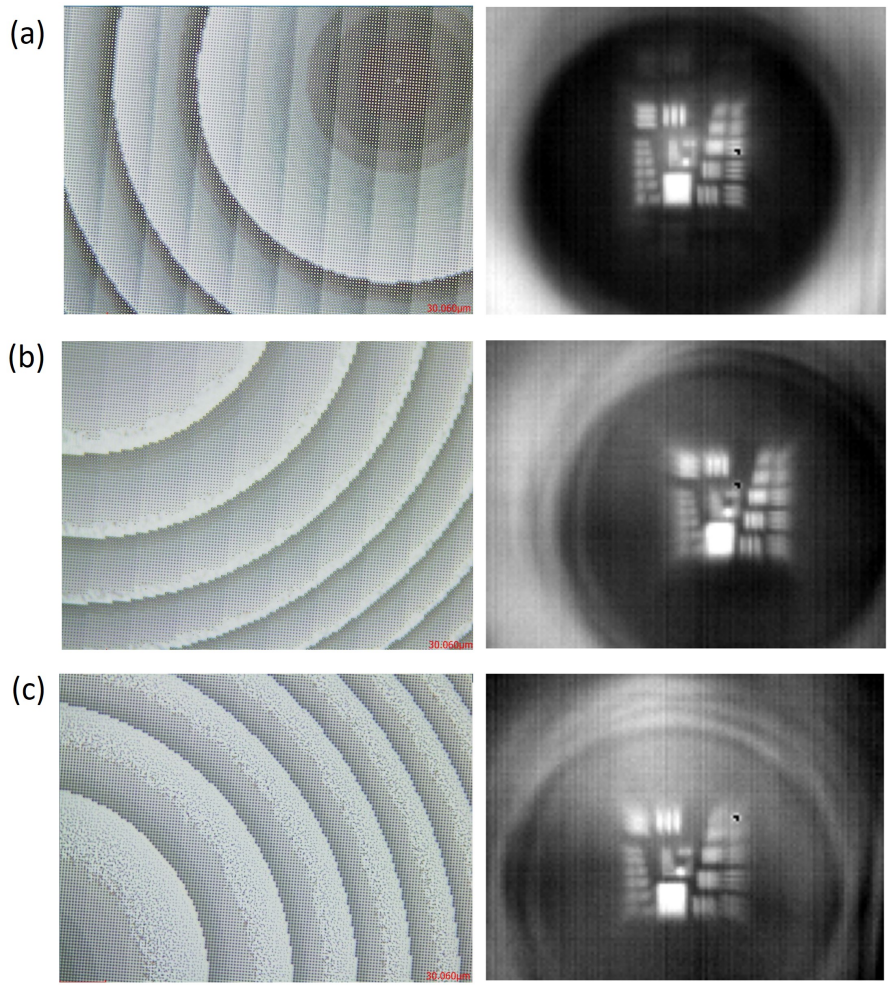

Figure 3.4: Resiliency to fabrication errors. Left panels show optical microscope images and right panels show the experimental imaging result using that meta-optic. (a) A meta-optic with striping errors. As a result of the striping errors, the image produced by this meta-optic has a double or "ghost" image. (b) A meta-optic with mostly good fabrication, but approximately 40% of the pillars missing. (c) A meta-optic with nearly half of the smaller pillars missing. Despite this, the optic still produces an image.

Chapter 4
EXPERIMENTAL CHARACTERIZATION

A number of quantitative and qualitative measurement techniques are used to analyze optical performance. Two most commonly used quantitative metrics for characterizing optics are the point spread function (PSF) and modulation transfer function (MTF). Imaging experiments are used to more qualitatively assess the performance of optics.

4.1 PSF and MTF

The point spread function (PSF) of an optic is simply how well the optic focuses a point source. An fictional perfect lens focuses a point source back to a point. A real lens is fundamentally limited by diffraction effects; the theoretically smallest resolvable distance is approximately

$$d = \frac{\lambda}{2NA} \tag{4.1}$$

where NA is the numerical aperture of the lens. A lens that achieves this resolution is "diffraction-limited." In reality, most real lenses have aberrations that distort and broaden the PSF from this limit. A point spread function measurement, depicted in Figure 4.1a, is a quantitative measurement of these aberrations. In a point spread function measurement, the imaging object is a point source located at infinity. This can be accomplished by focusing laser or LED illumination through a pinhole, creating an actual point source, or creating an effective point source using collimated laser illumination. This is because the wavefront from a point source at infinity is approximately collimated from the perspective of the optic. Then, the lens is simply placed its focal distance away from the collecting optics and the sensor to image the point source.

The PSF is a "function" because it is usually a function of conditions such as wavelength

and the location of the source. As the point source is moved such that the incident light is off-axis, the PSF is typically distorted. To fully characterize a lens, it is common to measure the PSF at many angles of incidence.

The PSF is also useful for image simulation. When an object is imaged, the expected result is the input convolved with the optic's point spread function. To capture the effects of the optic's field of view, it is common to generate a PSF grid, convolve the input with the PSF corresponding to that source location, and stitch the results together. Convolution with only the central PSF is a common approximation that generally works if the field of view is small so the object is at approximately normal incidence.

Another metric is the Modulation Transfer Function (MTF). The MTF describes how line pairs of given spatial or angular frequencies are resolved; this is illustrated in Figure 4.1b. In other words, it is the contrast of a line pair as a function of spatial (in line pairs per millimeter) or angular (in terms of cycles per milliradian) frequency. A typical optic exhibits high contrast at low frequencies (corresponding to larger lines) and reduced contrast at higher frequencies (corresponding to smaller lines). The contrast of a line pair is defined as $\frac{I_{max}-I_{min}}{I_{max}-I_{min}}$, where I_{max} and I_{min} are the maximum and minimum pixel values in the line pair. The conversion between spatial and angular frequency is straightforwardly obtained by multiplying the spatial frequency by the optic's effective focal length.

The MTF can be experimentally obtained in a number of ways. The MTF can be calculated from the Fourier transform of the PSF; this is most commonly how I have measured MTF. When using this method, it is important to correct for background noise since a nonzero background will depress the MTF. This is especially important for thermal cameras which may have a significant nonzero background reading due to the ambient temperature. To do a background correction, the preferred method is to take an image with the source turned off (or blocked) and subtract that image from the signal image. Alternatively, one can also calculate the average value of the background from a corner of the PSF image, where the reading should be zero, and subtract that average value from the data to zero the background. The MTF can also be determined directly by imaging a resolution chart. For

example, the USAF-1951 resolution chart pictured in Figure 4.1c shows line pairs at specified sizes. Knowing the line pair sizes and the distance of the chart from the optical system, the MTF cutoff frequency can be qualitatively assessed by determining the smallest discernible line pair, or quantitatively by taking cuts across line pairs and calculating the contrast of the image.

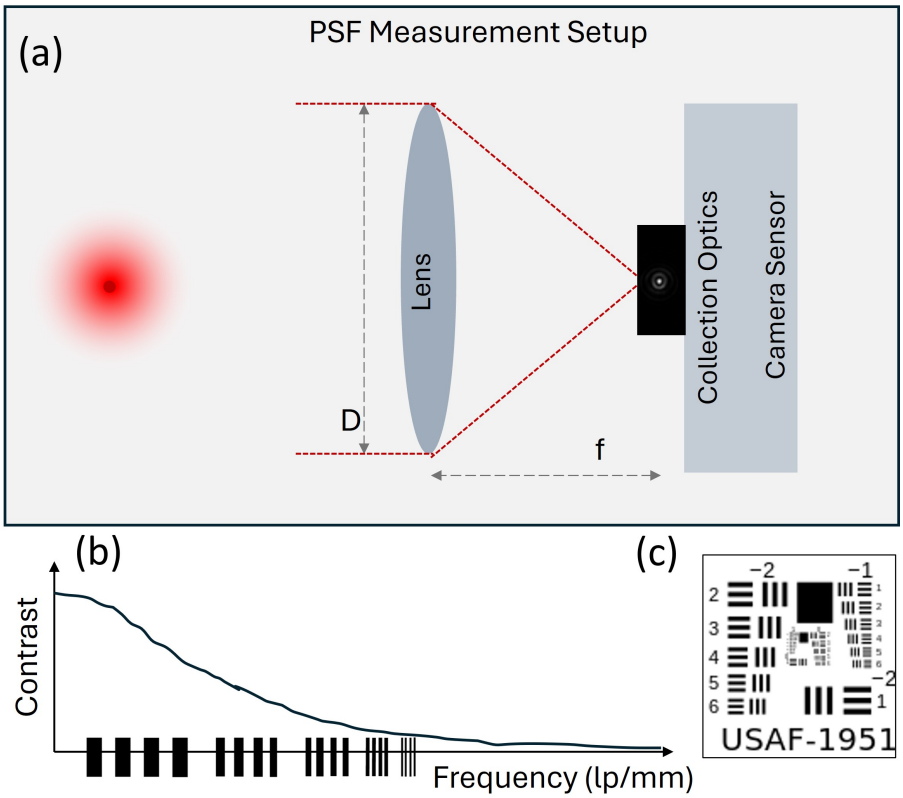

Figure 4.1: PSF and MTF characterization. (a) Schematic of a PSF measurement setup. A point source (at left) at infinity produces a wavefront that is approximately collimated when it reaches the imaging lens. This lens is focused onto a camera, possibly with the addition of collection or relay optics, to acquire the imaged point. (b) MTF schematic illustrating typical behavior where the contrast decreases as the frequency of the line pairs increases. (c) USAF-1951 resolution chart for quantitative and qualitative imaging experiments.

4.2 NA and Relay Optics

It is worthwhile to take an aside to discuss numerical aperture of a lens in greater detail. The numerical aperture describes the angles of light that the optical system can accept. If the maximum accepted angle is θ, then the NA of the system is given as $NA = n \cdot sin(\theta)$, where n is the background refractive index (typically air, $n = 1$). For the lens in Figure 4.1a, for example, suppose the lens diameter and focal length are equal. Then the maximum accepted angle of the light is $\theta = arctan(\frac{D}{2f}) = arctan(1/2)$. Then the NA of the lens is $NA = sin(arctan(1/2)) = 0.45$. The NA is related to F-number, which for a simple lens is the ratio of an optic's focal length to its aperture. As the aperture is increased for fixed focal length, the F-number is decreased, the NA is increased, and accordingly the resolution is increased. Microscope objectives have a relatively high NA around 0.7. For compound optical systems consisting of several elements, an effective F-number (and effective focal length) can be calculated from the angles of the rays.

Due to relatively large camera pixel size, it is often desirable to magnify the PSF prior to collecting the signal on the camera. Our visible GT-1930C cameras have a pixel size of 5.86 μm, which is too large to measure a diffraction-limited PSF on the order of 500 nm. Similarly, our FLIR A6751 camera for MWIR measurements has a pixel size of 15 μm. Furthermore, the MWIR camera has the additional complexity of protective housing that prevents placing optics very close to the sensor; for most of our meta-optics with focal length on the order of a few centimeters, this makes it practically impossible to measure the PSF without the aid of relay optics.

Relay optics serve several purposes: they can magnify the PSF to accommodate finite camera resolution, they can extend the distance between the measured optic and the camera sensor, and they can be used to aid in alignment. However, using relay optics comes at the significant cost of a more complex optical system. Relay optics may introduce aberrations and complicate measurements of already complex optical systems, making it difficult to determine if issues are arising from the optics being measured or from the relay optics. To avoid

introducing aberrations, the relay optics must provide high-quality imaging, and in addition the NA of the relay optics should be larger than that of the optics being measured. In visible setups, we typically use a microscope objective to provide high-quality large magnification for PSF measurements. Such microscopes are not available at thermal wavelengths, so those relay systems must be built from singlet lenses.

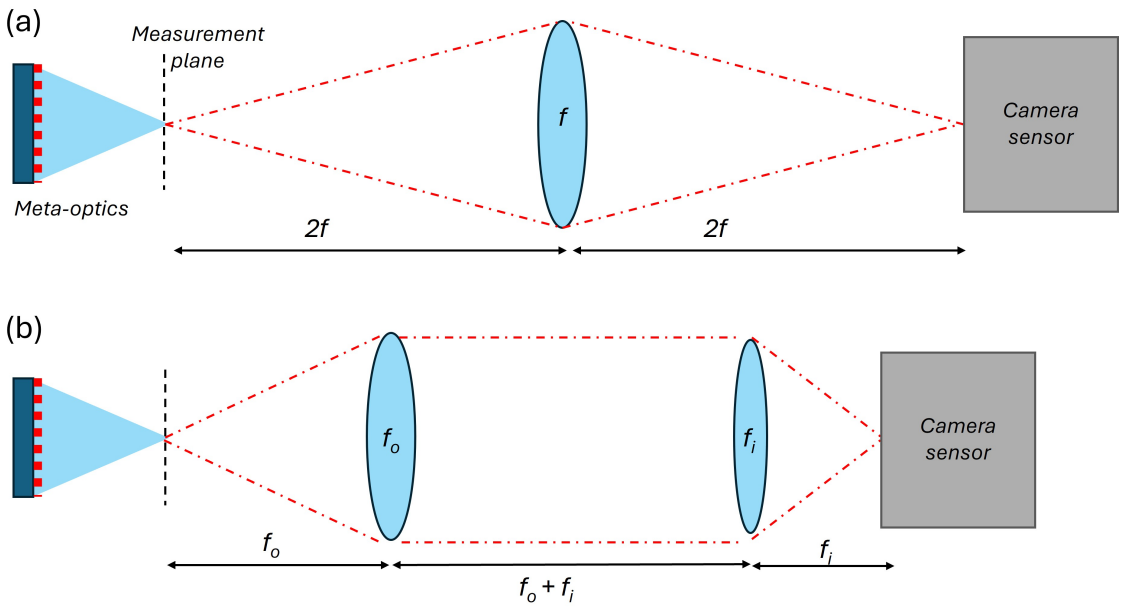

Figure 4.2: Common relay optics configurations. (a) A single lens $2f - 2f$ system: A single lens is placed a distance $2f$ from the plane of measurement and $2f$ from the camera sensor to image the measurement plane onto the sensor. If both distances are $2f$, then the magnification is 1. (b) A two-lens telescope system: An objective lens is placed its focal length f_o away from the measurement plane, thereby collimating the light. After propagating some distance, the light is focused onto the sensor via an image lens with focal length f_i. The magnification is given by $M = \frac{f_i}{f_o}$

Common relay optics configurations are shown in Figure 4.2. At the left, the meta-optics produces an image that we wish to relay back to the sensor on the right. The simplest

configuration (Figure 4.2a) uses a single lens. To achieve a magnification of 1 (the recorded image on the sensor is the same size as that produced by the meta-optics), the lens should be placed $2f$ away from the meta-optics image and $2f$ away from the camera sensor, where f is the focal length of the relay lens. To achieve a magnification that is not 1 (for magnifying the PSF, for instance), the singlet lens can be placed according to

$$\frac{1}{f} = \frac{1}{d_o} + \frac{1}{d_i} \tag{4.2}$$

That is, a lens of focal length f placed a distance d_o away from the object will produce an image at d_i on the other side of the lens with magnification $M = \frac{d_i}{d_o}$. Therefore, by moving the lens from $d_o = 2f$ to $d_o = f$, the magnification can be arbitrarily increased (as long as the camera sensor is also moved accordingly to capture the image). A second common configuration is the telescope configuration shown in Figure 4.2b. In this case, two lenses are used: an objective lens with focal length f_o placed its focal distance away from the measurement object, and an imaging lens with focal length f_i placed its focal distance away from the sensor. In this case, the magnification is given by $M = \frac{f_i}{f_o}$.

4.3 MWIR Setup

During my time in Arka's lab, we received a significant amount of funding to support the development of MWIR meta-optics. In this section, I will briefly review the capabilities of this setup. More details and examples are included in the sections covering the optics measured with this setup; in particular, see Sections 5.1 and 7.1. For a more detailed overview of the instruments, please see the full SOP that I wrote with MS student Tina Teichmann.

The laser is a Daylight Solutions MIRcat MWIR QCL. This laser offers both continuous-wave (CW) and pulsed operation, but I have only ever used it in CW mode. For CW and pulsed at moderate power, cooling is required, which is accomplished using the chiller that we set up. The laser has three modules, each covering a particular wavelength range for a total combined range covering 3.9 μm to 5.1 μm. The optical power output is dependent on both the current setting and the desired wavelength. This means that the amount of optical power

may change unexpectedly as the wavelength is changed, so particular care must be taken when changing the wavelength to avoid oversaturating the sensitive camera. At maximum current, each module can output a power of several hundred mW CW. This is significantly more power than is required for meta-optics. Meta-optics characterization requires only a few hundred μW, but the laser output is unstable at such a low current setting. To resolve this, we typically set the laser to the current required to output around 5 mW of optical power and use a neutral density filter (OD = 1, 10% transmission) to reduce the amount of light directed at the camera. The light that is reflected off the filter is directed at a thermal power meter for optical power monitoring.

In addition to the laser, we have several other MWIR sources on hand. We use a Torrey Pines Scientific hot plate to provide diffuse, broadband blackbody radiation for imaging experiments. Running the hot plate at higher temperature pushes the blackbody spectrum towards MWIR, but it would require an impractical temperature around 800K to achieve maximum radiation in the MWIR range. We typically run the hot plate around 130C (400K) for MWIR imaging experiments, which is results in a spectrum that is more heavily weighted towards longer wavelengths. To restrict this broadband thermal radiation to a desired wavelength range, we can use narrowband filters. At this time, we have filters centered at 3.5 μm and at 4.5 μm, each with 500 nm FWHM spectral bandwidth. Finally, we have two LEDs that output at 3.4 μm and at 4.3 μm, also with approximately 500 nm FWHM bandwidth.

The MWIR camera is a FLIR A6751 InSb Cooled camera. In contrast to the laser that is liquid-cooled, the camera is simply fan-cooled. The camera comes with a compound refractive lens assembly with effective focal length of 25 mm. The camera has 640 $\times$ 512 pixels at 15 μm per pixel resolution and has a specified wavelength coverage of 3 - 5 μm.[1] One key practical note is that the camera sensor is located about 5.4 cm inside the camera's protective housing; this means that it is not possible to directly measure meta-optics with

[1]However, we have determined that the upper limit is really around 4.8 μm. While the laser can cover up to 5.1 μm, the camera is limited to slightly shorter wavelengths.

focal lengths under 5.4 cm. Hence, relay optics are required. For measuring very small optics, we have successfully used our 25 mm diameter, 12.5 mm focal length aspheric refractive lens in the configuration shown in Figure 4.2a to provide magnification around 50×. For general-purpose imaging, we have a 50 mm diameter, 50 mm focal length singlet that has sufficiently large NA to measure most of our meta-optics in a simple relay configuration. When using the telescope configuration shown in Figure 4.2b, we often use the FLIR compound refractive ($f = 25$ mm) as the imaging lens and an $f = 25$ mm singlet lens as the objective to achieve a magnification of 1.

Chapter 5

SINGLETS

The field of single-layer meta-optics has matured significantly since the first demonstrated meta-optics. In many cases, singlet meta-optics are designed to replace refractive lens elements for imaging with a thinner, lighter optical system. A significant amount of work has already been done in the field of full-color imaging [18, 19, 20, 21]. A wide variety of non-imaging applications have been demonstrated as well, which include spectroscopy [22] and optical computing [23, 24]. My contributions in this area have focused on imaging at thermal wavelengths and in applying meta-optics to perform convolution operations as part of a convolutional neural network for image classification. In this chapter, I begin with my work on the simplest singlets (hyperboloid metalenses) and build up to the more complex neural network application.

5.1 MWIR Hyperboloids Scaling Study

The hyperboloid phase profile has historically been used as baseline for first demonstrations and as a point of comparison for new materials and novel design strategies. To test our newly developed MWIR fabrication and measurement capabilities, we fabricated a set of all-silicon hyperboloid MWIR meta-optics of increasing apertures. The hyperboloid phase profile is given by

$$\phi(r) = -\frac{2\pi}{\lambda}(\sqrt{r^2 + f^2} - f) \tag{5.1}$$

The hyperboloid phase profile provides diffraction-limited resolution in theory. Recall from Chapter 3 that diffraction-limited resolution is given by $d = \frac{\lambda}{2NA}$, which is notably dependent only on the wavelength and NA of the lens. However, in realistic lens systems,

aberrations typically scale with the aperture of the lens [25]. To test whether aberrations scale with the lens in meta-optics, we fabricated a set of meta-optics with the same NA = 0.45 but different apertures. Specifically, we fabricated hyperboloid meta-optics where $D = f =$ 2 mm, 5 mm, 10 mm, and 20 mm for 4.5μm wavelength.

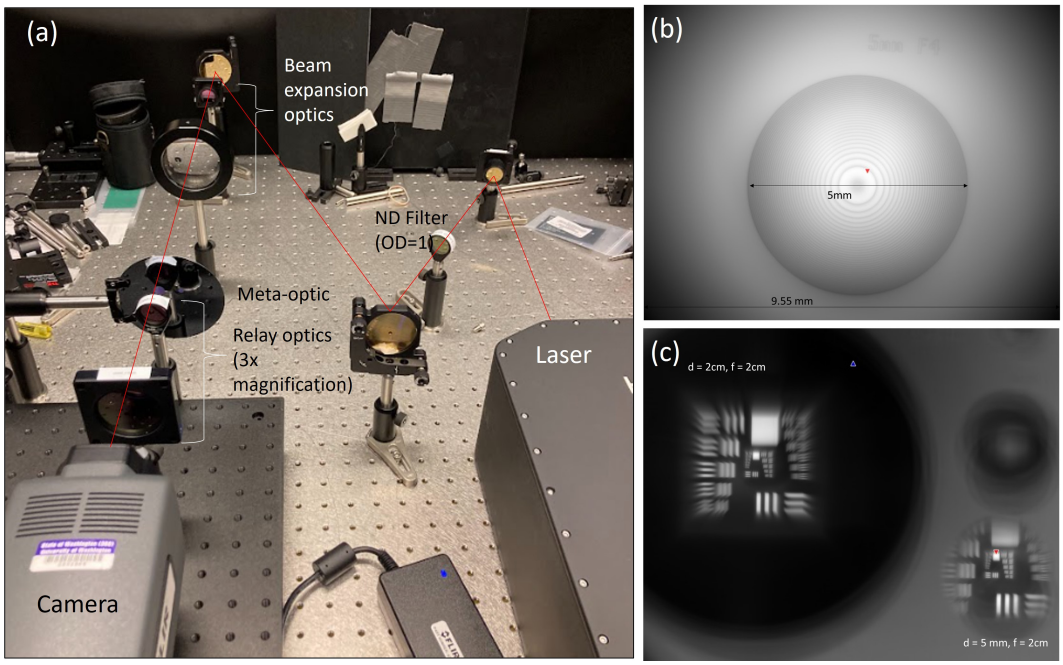

Figure 5.1: MWIR hyperboloids measurement setup. (a) Photograph of the optical setup. Light from the laser passes through an ND filter to reduce the optical power and three mirrors to align the beam to the camera and parallel to the table. Two refractive lenses are used to expand the collimated beam before it passes through the meta-optics. After the meta-optics, two refractive lenses are used as relay optics to collect and magnify the meta-optics PSF. (b) The relay optics are focused on a 5 mm diameter meta-optic. This image is used to calibrate the effective resolution of the camera given the relay optics. (c) Focusing on the images produced by two meta-optics fabricated on a single wafer.

The experiment setup for PSF measurements with laser illumination is shown in Figure 5.1. Output from the laser is collimated, but it must be aligned to the camera and the

beam must be expanded to fill the entire aperture of the meta-optics. For expansion, we used a 25 mm diameter, 50 mm focal length lens to focus down the beam followed by a 75 mm diameter, 150 mm focal length lens to collimate the magnified beam. Because the MWIR beam is invisible to the human eye, alignment and collimation is not trivial. First, we use the red alignment beam onboard the laser to align the beam to the camera, ensuring it propagates parallel to the optical table as well as being laterally aligned. Secondly, to set up the expansion optics, we use the camera's compound refractive lens to image the beam. With the compound refractive lenses focused on the aperture of the larger lens, we attempt to place it such that the beam fills up as much of the optic as possible.

The relay optics are aligned separately. In this case, the relay optics consist of a 25 mm diameter, 25 mm focal length lens followed by a 50 mm diameter, 75 mm focal length lens in telescope configuration. The magnification of this system is a factor of 3. To ensure the relay optics are well aligned, we set up the hot plate to provide diffuse MWIR illumination and place a meta-optic at the object plane of the relay system. By focusing onto the surface of the optic like a microscope, the relay optics can be tuned to achieve the best imaging quality. An image of the relay optics focused onto the surface of a 5 mm diameter meta-optic is shown in Figure 5.1b. In the upper right, there is some text written on the surface of the wafer.

The camera and relay optics are mounted on a micrometer translation stage so that the relay and camera system can be translated back for measurement in various focal planes. For example, the camera stage positioned to focus at the surface of the meta-optics is shown in Figure 5.1b, and the camera stage moved backwards to focus on the image produced by the meta-optics is in Figure 5.1c.

Using this setup, we measured the PSFs of the hyperboloid metalenses, with the aim of determining whether aberrations worsen for larger apertures (despite keeping the same NA). The experimentally measured PSFs are shown in Figure 5.2a, with line cuts shown in Figure 5.2b. The PSFs are relatively high quality, with a faint Airy disk around the center and low noise near the exterior. Notably, the width of the PSFs does not change with increasing aperture; this indicates that aberrations are not worsening with incrased

aperture, which is a promising result for large aperture meta-optics. However, the measured PSFs are approximately a factor of two larger than the diffraction-limited (theoretical) PSF. We attribute that this is most likely due to experimental conditions such as the limited size of the camera sensor, pixel-to-pixel contamination, or misalignment of the laser beam. In Figure 5.2c, we show the maximum PSF intensity as a function of aperture. As expected, larger apertures collect more signal for a brighter PSF and improved signal to noise ratio in imaging. The 10 mm lens seems to be an outlier to the general trend, which is unsurprising because the 10 mm aperture metalens was fabricated on a separate wafer from the 2 mm, 5 mm, and 20 mm aperture metalenses. Therefore, the unexpectedly low intensity on the 10 mm aperture lens is likely due to sub-optimal fabrication conditions.

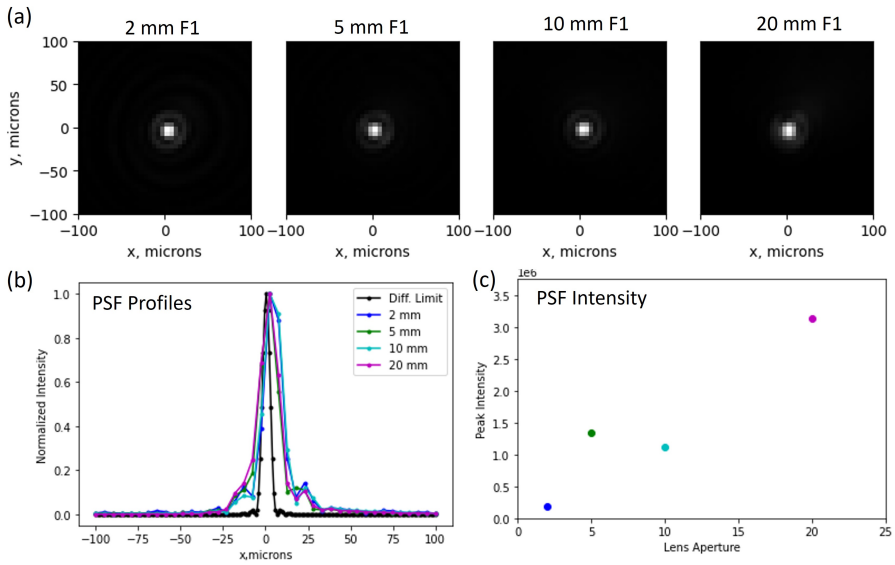

Figure 5.2: Hyperboloid PSF measurement results. (a) Experimentally captured PSFs for 2 mm, 5 mm, 10 mm, and 20 mm (all F-number equal to 1) aperture hyperboloid meta-optics. The displayed PSF size is 200μm $\times$ 200μm. (b) Profiles extracted from the PSF images in (a). A diffraction-limited PSF is shown in black for comparison. (c) Peak PSF intensity as a function of metalens aperture.

5.2 Sparse Aperture

There are two key advantages of large aperture optics. Firstly, a large aperture lens collects more light for higher signal-to-noise ratio (SNR). This is especially important for thermal wavelengths where the ambient signal is low and the sensors are noisy. Secondly, a larger aperture (while keeping a fixed focal length) increases the NA for higher angular resolution. Meta-optics are an attractive replacement for large aperture refractive lenses because meta-optics can increase aperture without adding significant weight due to their thinness. However, patterning a large surface area at high resolution is practically challenging.

Therefore, following a similar synthetic aperture approach to Zhao et al. [26], we are collaborating with Rice University to develop ultra large aperture meta-optics. In this way, several smaller aperture meta-optics are arranged to create an effectively larger aperture optic. While this approach does not address the first benefit of large aperture (higher SNR) since it does not increase the amount of light modulated through the optics, it does increase the resolution by covering an effectively larger aperture.

This project is being led by Jing Wang at Rice. I primarily developed the fabrication with the assistance of MS student Vladimir Yarmolik. In this initial phase of the project, we are fabricating several sub-apertures on a single wafer (up to 8 cm effective aperture). The ultimate goal of this project is to scale up to an effectively 50 cm metalens wherein each sub-aperture consists of a full-wafer meta-optic, for high-resolution long-range MWIR imaging.

5.2.1 Fabrication Constraints

Fabrication of large area meta-optics is challenging because a large area must be patterned while maintaining high resolution. As discussed in Chapter 3, we developed two laser writing processes for the 4 mm and the HiRes write heads. While the HiRes write head provides higher resolution, it writes too slowly to cover an entire 100 mm diameter wafer. On the other hand, the 4mm write head can write a full wafer in under six hours but is limited to around

1μm resolution. Therefore, we designed new scatterers compatible with this restriction and fabricated simple hyperboloid meta-optics to test their effectiveness. As shown in Figure 5.3a, the ideal MWIR scatterers with 2μm periodicity and 3μm pillar height exhibit a relatively smooth relationship between phase and pillar width and high transmission. To be compatible with the limitations of the 4mm write head, we designed scatterers with 5.6μm periodicity and 7.9μm pillar height, with the response shown in Figure 5.3b. The phase is not as well controlled and the transmission is lower, but nevertheless the required 0 to 2π phase shift is achieved. An additional consideration is that the large periodicity (greater than $\lambda/2$) can introduce aliasing effects if the desired phase gradient is large; this effect is studied more closely in Section 6.2, where we used similarly larger-than-wavelength periodicity.

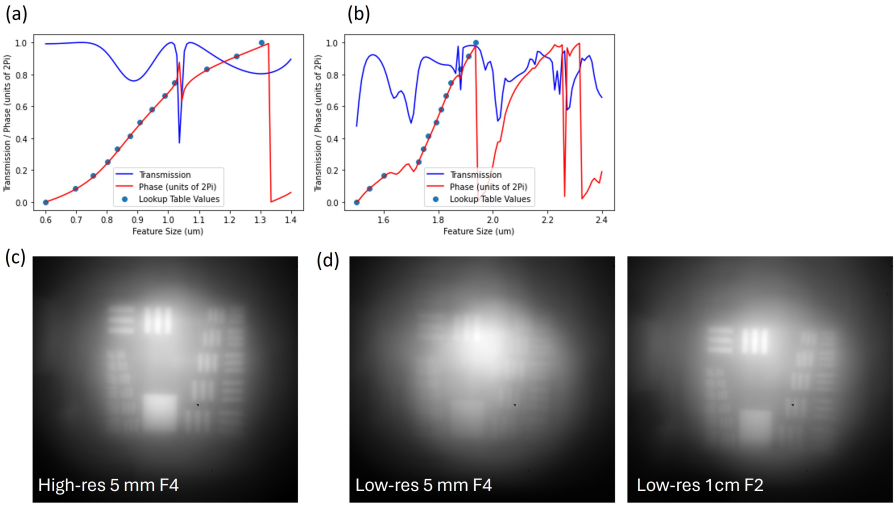

Figure 5.3: Low-resolution versus high-resolution MWIR fabrication results. (a) The ideal MWIR scatterers with 2μm periodicity and 3μm pillar height. (b) The low-resolution MWIR scatterers with 5.6μm periodicity and 7.9μm pillar height. (c) The experimentally obtained image produced by a 5 mm diameter, f = 2cm hyperboloid metalens that was fabricated with the HiRes scatterers shown in (a). (d) Experimentally obtained images produced by 5mm diameter and 1 cm diameter f = 2 cm hyperboloid metalenses fabricated with the low-resolution scatterers shown in (a).

To test these scatterers, we fabricated a set of test hyperboloid metalenses with 5 mm aperture and 2 cm focal length using each scatterer, and the imaging results are shown in Figure 5.3c and 5.3d. As expected, the higher-resolution scatterers exhibit better imaging quality, which I attribute mainly to their higher efficiency. The low-resolution scatterers themselves have lower transmission, and reduced phase sampling due to larger periodicity also reduces efficiency. However, the larger aperture enabled by the 4mm write head can compensate for these effects. A low-resolution metalens with the same focal length but larger (1 cm) aperture has similar performance to the high-resolution metalens. For this project, full-wafer fabrication is required and therefore the low-resolution scatterers must be used.

5.2.2 Results

We designed, fabricated, and tested four configurations as shown in Figure 5.4. In each case, broadband hot plate illumination is used through a USAF resolution target and the images were reconstructed using simulated PSFs. Firstly, as shown in Figure 5.4a, we show the result for the center aperture alone as a baseline. Since it has the smallest aperture in terms of both written area and spatial extent, this configuration has the lowest-quality imaging. We tested two different sparse aperture configurations: a triangle configuration (Figure 5.4b) and a Golay configuration (Figure 5.4c). Both performed similarly well in simulation, but the distribution of sub-apertures is more equally distributed radially. Therefore, the Golay PSF is expected to be more symmetric and we observed better performance in the Golay aperture in experiment. Both the triangle aperture and the Golay aperture wafers had some fabrication issues and will be re-fabricated. In the triangle aperture, the lithography had some striping artifacts that cause the double-image shown in the red circle. In the Golay aperture, two of the sub-apertures had photoresist streaking that ruined portions of those optics for reduced SNR. Finally, the effective aperture shown in 5.4c is a single aperture at the center with the same written area as the triangle and Golay configurations. However, due to the smaller spatial extent of this configuration, it has lower angular resolution.

The preliminary experiment results of this study are promising and a publication, led by

Jing, is in preparation.

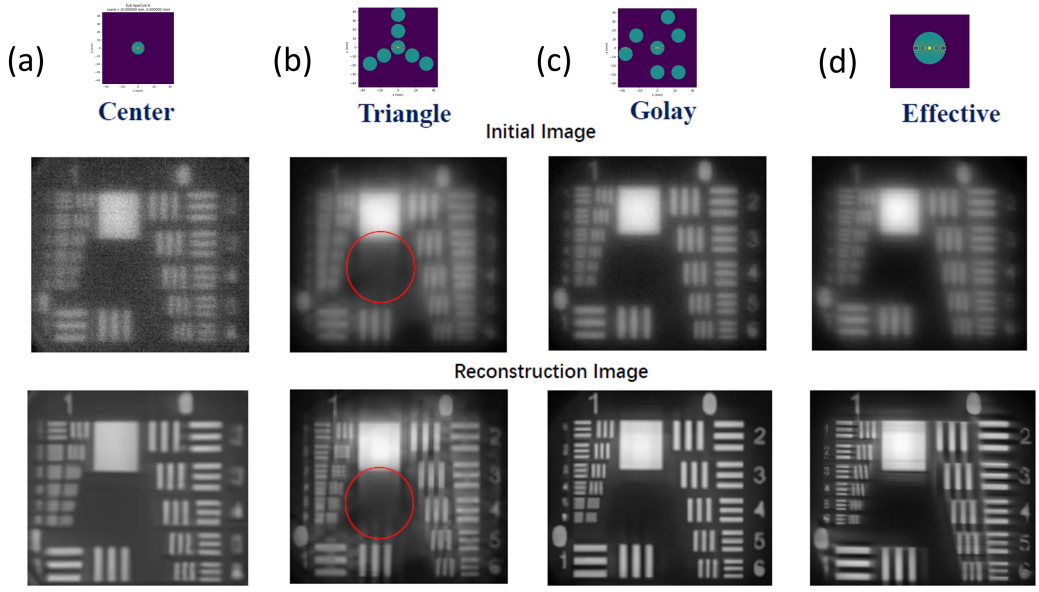

Figure 5.4: Experiment results for MWIR sparse aperture imaging. For each configuration, the top row is the raw experiment result and the bottom row is the image computationally reconstructed with the simulated PSF. (a) The center aperture alone serves as a baseline. (b) The triangle configuration has six sub-apertures arranged around the center aperture in three arms. (c) The Golay aperture has the six outer sub-apertures arranged in a more radially symmetric configuration. (d) The effective aperture has a single aperture at the center of the same written area as the triangle and Golay configurations.

5.3 Broadband Thermal Imaging

A common goal of meta-optics is broadband imaging, but strong chromatic behavior is a characteristic of meta-optics and other forms of diffractive optics [19]. This effect can greatly deteriorate imaging performance, as it is impossible to focus light at different wavelengths in the same focal plane. The chromatic behavior of meta-optics originates from two sources: dispersion due to phase wrapping in the phase mask and dispersion of the scatterers themselves. These effects are described in Figure 5.5.

Of the two effects, the dispersion from the phase mask itself is much more severe than the dispersion of the scatterers. That is, light of different wavelengths propagating through the same phase mask experiences different effects. Recall the expression for the bending angle of light through a meta-optic:

$$n_i sin(\theta_i) - n_o sin(\theta_o) = \frac{\lambda}{2\pi} \frac{d\phi}{dx} \tag{5.2}$$

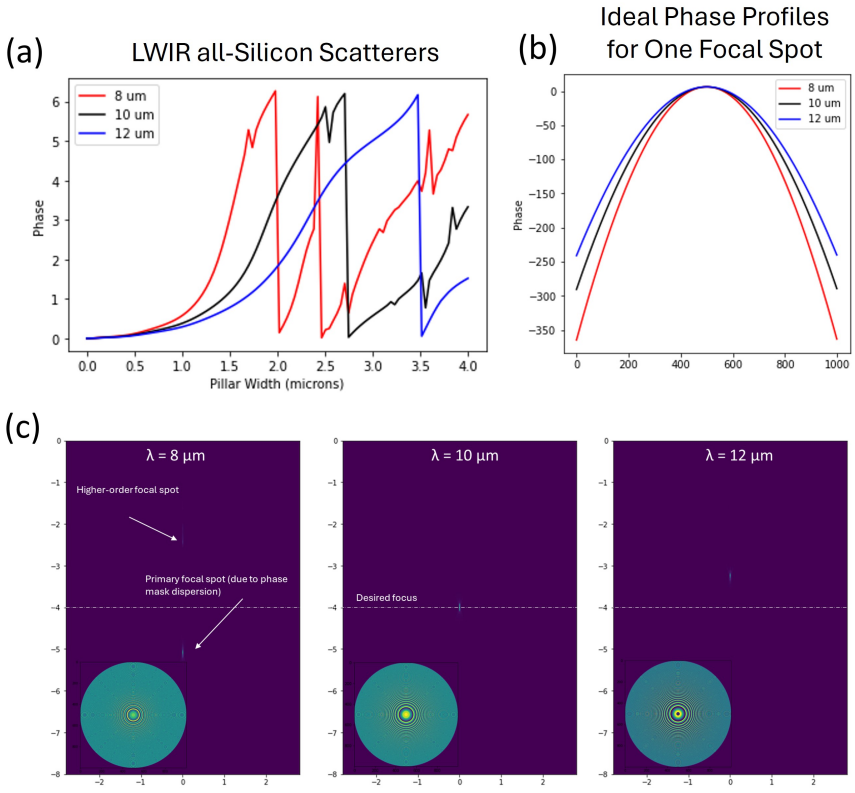

Figure 5.5: Chromatic aberrations in meta-optics. (a) Exemplary dispersion in scatterers. For all-Si pillars with 4 μm periodicity and 10 μm pillar height, light of different wavelengths experiences different phase shifts. (b) Different phase profiles are required to focus light of different wavelengths at the same focal spot. (c) Simulated chromatic aberrations for a 4 mm diameter, 4 mm focal length LWIR hyperboloid metalens composed of the scatterers in (a). The metalens design wavelength is 10 μm.

The factor of $\frac{\lambda}{2\pi}$ implies that light of different wavelengths will have different bending angles θ_i upon experiencing the same phase gradient $\frac{d\phi}{dx}$. Now, it is true that the scatterers themselves typically have some dispersion such that $\frac{d\phi}{dx}$ will not be exactly the same for each wavelength. However, in most forward-designed meta-optics, the phase is wrapped modulo 2π according to the design wavelength, and these phase wraps are then "baked in" to the optic. Effectively, what is then achieved is a blazed grating with nearly ideal 0 to 2π gradient at the design wavelength and a less efficient grating at non-ideal wavelengths. The distance between phase resets has already been set by the phase wrapping. In order to focus light of different wavelengths in the same focal plane, a different phase mask for each wavelength must be realized.

A number of works in the visible have addressed this issue using dispersion engineering [10], computational imaging [18, 21], and hybrid meta-optic / refractive systems [27]. Dispersion engineering is the most common approach. In dispersion engineering, a scatterer library is designed to contain pillars with a wide range of dispersive behavior. To accomplish this, either complex-shaped meta-atoms or very high aspect ratio pillars are often employed. The scatterers are then placed to minimize the phase error at the design wavelengths. However, there are several limitations of this approach. Firstly, as shown in Figure 5.5b, the required dispersion towards the edges of the optic becomes large, quickly exceeding the possible dispersion in the meta-atom library. This imposes fundamental trade-offs between NA, bandwidth, and pillar thickness [28]. As a result, most dispersion engineering reports are limited to small aperture meta-optics.

In our development of meta-optics for broadband thermal imaging, we have not taken the dispersion engineering approach. Rather, we combine phase mask engineering with light computational image reconstruction to circumvent the NA/bandwidth limits inherent in other approaches.

5.3.1 LWIR Broadband Imaging

Former PhD student Luocheng Huang developed a design framework that we term MTF-engineering. This work is reported in [29]: *Luocheng Huang, Zheyi Han, Anna Wirth-Singh, et al. Broadband thermal imaging using meta-optics. Nature Communications* ***15****, 1662 https://doi.org/10.1038/s41467-024-45904-w, February 2024.* I had a supporting role in this project (experimental characterization and data analysis) so I will report only the key results here.

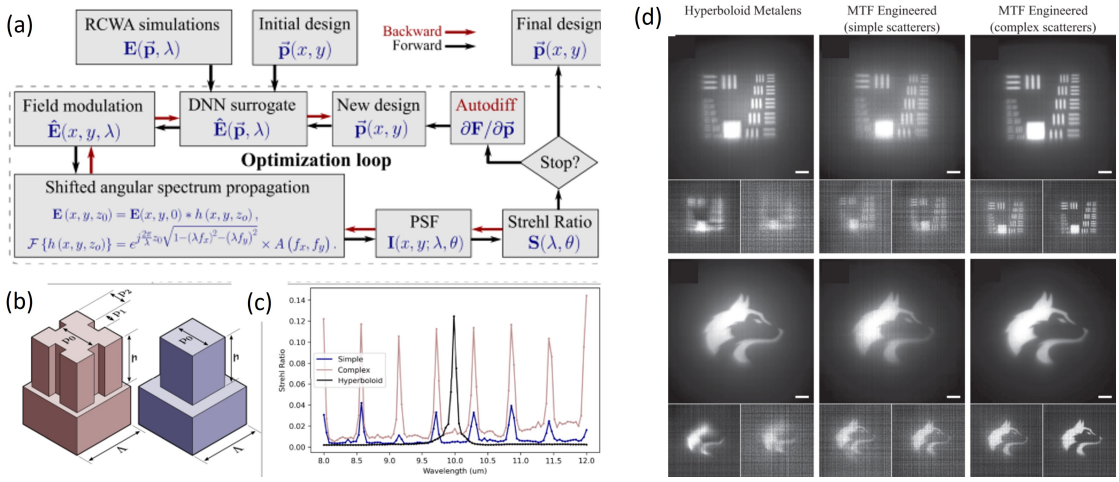

Figure 5.6: LWIR broadband imaging via MTF-engineering. (a) Schematic of the inverse design process. (b) Schematic of the complex (red) and simple (blue) meta-atoms. (c) Simulated Strehl ratio versus wavelength for a hyperboloid metalens (black), complex scatterers (red), and simple scatterers (blue). (d) Experimental imaging results for a hyperboloid metalens, simple scatterer MTF-engineered optic, and complex scatterer MTF-engieered optic. In each trio, the upper image is unfiltered hot plate illumination. The lower left image is under 10 μm filtered illumination and the lower right is under 12 μm filtered illumination.

The design strategy is described in Figure 5.6a. The approach is termed "MTF-engineering" because the figure of merit is related to the area under the MTF curve. The goal is to pass as much information as possible through the lens to obtain an image that can be more easily

reconstructed using a light computational backend. The figure of merit is inherently optimized when all wavelengths perform equally well, therefore constraining the optics to have uniform performance over the design wavelengths without explicitly defining uniformity as an optimization criterion.

A key challenge in inverse design is the scatterer-to-phase mapping. In gradient-descent based optimization schemes, all operations must be differentiable in order to calculate the gradients. Typical electromagnetic simulations, like RCWA and FDTD, are not differentiable, and are also typically too slow to be used in an optimization loop. [1] To solve this problem, Huang uses a deep neural network model to quickly map between scatterer and phase in the optimization loop. To do this, he simulated a large library of meta-atoms and used that data to train a deep neural network. The neural network is then called in the optimization loop to quickly map between scatterer and phase.

In this work, Huang designed broadband LWIR meta-optics with both simple and complex-shaped scatterers as shown in Figure 5.6b. As expected, the complex-shaped scatterers performed slightly better in experiment as shown in Figure 5.6d due to the larger number of degrees of freedom. However, due to computational limitations, only eight wavelengths were optimized. Figure 5.6c shows the Strehl ratio (defined as the ratio of focal spot intensity relative to an ideal lens) versus wavelength. The clear peaks in performance indicate the optimized wavelengths. In the experimental results shown in 5.6d, the top image is the result under unfiltered broadband LWIR illumination. In this case, the bandwidth is limited to that of the camera sensor, which is 8 - 14 μm. In the two insets below each larger image, we show the imaging result with 8 μm and 12 μm narrowband filters (without adjusting the focal plane)[2]. While the hyperboloid metalens image appears to perform relatively well under broadband illumination, its performance is greatly deteriorated with the filters in place.

---

[1] There has been work to develop differentiable RCWA frameworks, but to my knowledge they have not been used to demonstrate broadband meta-optics.

[2] It is almost always possible to get the metalens to focus well at a different wavelength if the focal plane is adjusted. However, for broadband imaging, it is not possible to adjust the plane for each wavelength. Therefore, it is key to hold the focal plane constant when performing these measurements.

This is because the hyperboloid has excellent performance at its design wavelength of 10 μm, so this wavelength overwhelms others in a broadband measurement. However, if the illumination is filtered to a different wavelength, the superior broadband performance of the MTF-engineered optics is clear.

5.3.2 MWIR Broadband Imaging

A similar undertaking is underway to develop large aperture broadband MWIR meta-optics. In an initial demonstration, we designed a set of three optics with 1 cm diameter and 1 cm focal length: a forward-designed hyperboloid, which is expected to have nearly diffraction-limited performance at its designed wavelength but poor broadband performance; a inverse-designed extended depth of focus (EDOF) lens, which is expected to have better broadband performance; and an inverse-designed MTF-engineered lens, which is expected to have the best broadband performance. These phase profiles are shown in Figure 5.7. The two inverse-designed broadband meta-optics were fabricated in cSi on sapphire platform using e-beam lithography. In this case, the pillars are 1.5 μm tall on 460 μm sapphire substrate with a periodicity of 1500 nm. A cSi hyperboloid was also attempted but failed due to a design error; it was later re-made, but using the HiRes all-Si process. So while the three optics presented in this section are consistent in diameter and focal length, the material platforms are mixed. The cSi on sapphire optics have higher quality fabrication and better transmission.

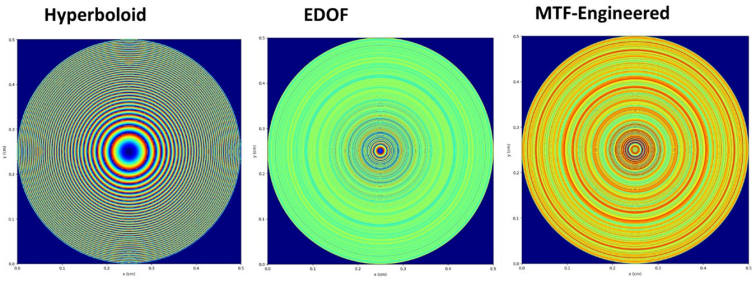

Figure 5.7: Phase profiles of a hyperboloid meta-optic, inverse-designed EDOF optic, and inverse-designed MTF-engineered optic.

The hyperboloid phase profile is given by Equation 5.1. As apparent by the factor of $\frac{1}{\lambda}$, a different phase profile to achieve focal length f is required for different wavelengths, leading to strong chromatic aberrations. The hyperboloid lens provides a baseline for comparison to our broadband lens designs.

The idea behind the EDOF lens is to extend the focal spot into a line so that chromatic aberrations become less severe. Our group previously fabricated and tested forward-designed EDOF lenses in the visible spectrum [30], but we have found that inverse-designed lenses have superior results [18]. To inverse-design the EDOF lens, we assume normally incident illumination and radial symmetry of the optic. This allows us to reduce the 2D phase mask to a radial profile, dramatically reducing memory requirements and increasing the optimization speed. We define an initial phase mask guess and propagate light to the focal plane, using Hankel transforms and Rayleigh-Sommerfeld propagation. We iteratively update the phase mask and propagate to the focal plane. We define our merit function to maximize the intensity of the light at the focal plane for a range of wavelengths, resulting in a lens with EDOF properties. Crucially, the assumption of on-axis illumination and rotational symmetry to reduce the 2D phase mask to a radial profile allows us to optimize larger aperture meta-optics at a fraction of the computational resources necessary to simulate the entire lens. For this lens, we optimized 500 wavelengths over 20,000 iterations, for a relatively large aperture of 1 cm and 1.5 micron periodicity (3,333 scatterers radially).

The MWIR MTF-engineered lens uses the same approach as the broadband LWIR work described in Section 5.3.1. This inverse design approach optimizes the volume under the Modulation Transfer Function (MTF) for improved lens performance. Unlike the EDOF method, the MTF-engineered method does not assume normally incident light. This allows for optimization at various angles of incidence, but the increased computational complexity reduces the number of wavelengths that can be optimized and also limits the aperture of the optic.

One key distinction between the EDOF the MTF-engineered inverse design processes is that the MTF-engineering approach takes scatterer dispersion into account, while the

EDOF approach does not. While scatterer dispersion certainly has some effect on chromatic behavior, the much more significant chromatic source of chromatic aberration is the phase mask itself.

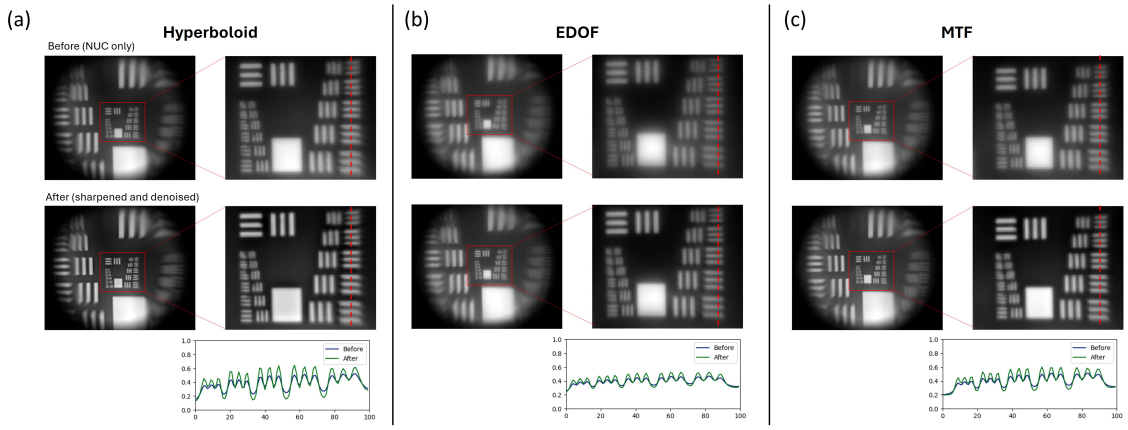

Figure 5.8: Broadband MWIR imaging with a hyperboloid metalens, an EDOF-designed singlet, and an MTF-engineered singlet. All meta-optics are 1 cm in diameter and have 1 cm focal length. The top row shows the essentially raw images (background correction only) and middle row shows those images after processing with a Gaussian sharpening filter and bm3d [31] denoising algorithm. (a) Hyperboloid metalens designed for 4.5 μm illumination.

Hot plate imaging results with these optics are shown in Figure 5.8. The MTF-engineered optic exhibits slightly better performance than the hyperboloid and EDOF-designed meta-optics. However, the explicitly designed broadband optics did not dramatically outperform the simple hyperboloid metalens in this case. At present, we attribute this to experimental conditions that are favorable for the hyperboloid. In this case, we used a hot plate set to 130C as the source, which emits a spectrum that is significantly stronger towards longer wavelengths. Since we designed the hyperboloid for 4.5 μm and the broadband optics were designed for 3-5 μm, the source spectrum is skewed in favor of the hyperboloid. I hypothesize that the excellent performance of the hyperboloid at 4.5 μm is overwhelming that of the non-optimal wavelengths, so the hyperboloid performs relatively well under these experimental

conditions. Ongoing and future work will investigate whether a flatter spectrum source will improve the imaging performance of the broadband MWIR meta-optics.

While the relative performance of the inverse-designed broadband meta-optics relative to the simple hyperboloid is unclear in the imaging experiment, PSF measurements indicate that the MTF-engineered optic is functioning as expected. Using the MWIR laser as a source, I measured the PSF of both optics for wavelengths between 4 and 5 μm as shown in Figure 5.9. While the hyperboloid metalens has excellent performance at the design wavelength of 4.5 μm, it deteriorates quickly at non-design wavelengths. On the other hand, the MTF-engineered singlet lens has more consistent performance across all wavelengths. In this figure, each image is scaled to its own maximum for visualization so the relative brightnesses of the different wavelengths is not reported.

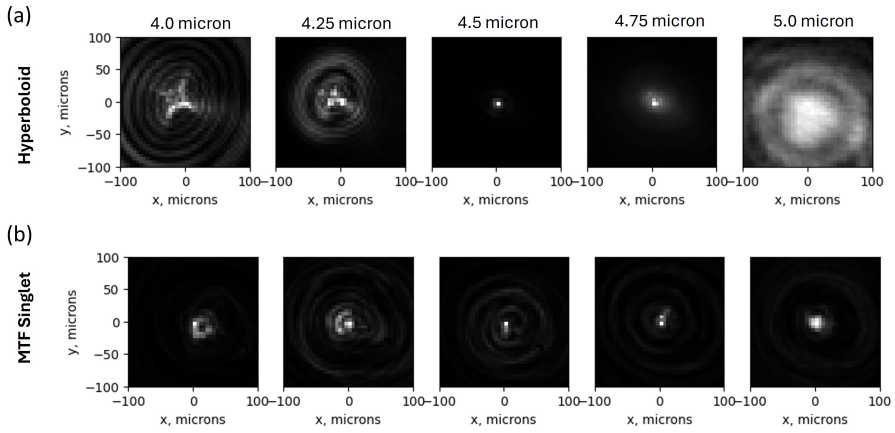

Figure 5.9: Broadband MWIR singlet PSF measurements. (a) PSFs of the simple hyperboloid metalens from 4 μm to 5 μm. (b) PSFs of the MTF-engineered singlet.

5.4 Meta-Optical Encoder for Hybrid Convolutional Neural Network

So far, I have presented meta-optics only for imaging applications. In this section, I present something dramatically different: meta-optics as part of a hybrid optical-electronic convolutional neural network for image classification. This highlights a unique application of

meta-optics. The contents of this chapter are adapted from [32]: *Anna Wirth-Singh, Jinlin Xiang, Minho Choi, Johannes E. Fröch, Luocheng Huang, Shane Colburn, Eli Shlizerman, and Arka Majumdar. Compressed Meta-Optical Encoder for Image Classification. arXiv Preprint, https://doi.org/10.48550/arXiv.2406.06534, June 2024*, with permission from the authors.

This project was a collaborative effort between me, Jinlin, and Minho; we all contributed equally. It is not possible to discuss my work on this project without also including the significant contributions from Jinlin and Minho. Specifically, Jinlin developed the knowledge distillation approach, optimized the convolutional kernels, and conducted the ablation studies and principal component analysis in the published work. I developed the PSF engineering approach, designed the meta-optics, and generated the comparisons between optical and electronic results. Minho fabricated the meta-optics and conducted the experiment. I led writing this manuscript, and in the next iteration of this project (where we developed polychromatic meta-optics for classifying the more complex CIFAR-10 dataset), Minho is taking the lead.

5.4.1 Introduction

Convolutional neural networks (CNNs) are a network structure commonly used in machine vision tasks, especially image classification [33]. In a CNN, an input image is convolved with a kernel (a matrix) that works to identify key features in an image. Most CNNs are composed of several convolutional layers that identify features of images and pass them to the next steps of the network, ultimately leading to the classification of the input into one of the defined classes. While powerful, the convolution operation is computationally expensive, leading to high latency and power consumption. In fact, it has been estimated that about 80% of the total runtime of CNNs is used in performing convolution operations [34]. Reducing this latency and as a result power consumption has become an active area of research, with multiple works proposing free-space optical systems as a solution [35, 36, 37, 38]. Beyond latency reduction and power consumption, optical information processing

features qualities including high bandwidth, spatial parallelism, and low-loss transmission which have led to a surge of interest in the field [35].

For decades, it has been known that a $4f$ lens system can be used to perform convolutions optically by placing an appropriate filter at the Fourier plane of the lens [39, 40, 41, 36]. This was demonstrated in 2018 [36] using a diffractive optical element as the filtering element and traditional refractive lenses composing the $4f$ system. Spatial light modulators [38] and digital micromirror devices [42] can also be used as the filtering element. However, one drawback of the Fourier-based $4f$ approach is that it requires three elements (two lenses and a spatial filter), resulting in a bulky optical system with greater propensity for misalignments than single-element optical systems. Such misalignments from each optical convolutional layer cannot be ignored even when weights are trained with noisy inputs. In addition, the filtering optics must be contained within a compact area at the focal plane in the $4f$ system, which limits parallel processing ability unless creative measures are taken such as utilizing naturally present diffraction orders [42] or lenslet arrays [37].

Advantageously, the convolution operation can also be performed using free-space optics and requires only a single element. The resultant image produced by any optics is the input convolved with the point spread function (PSF) of the optics [43, 44, 45]. Therefore, by engineering optics to produce a particular PSF, convolution can be performed optically simply via passing light through the optics. Further, by passing the input through several of these optics in parallel, multiple convolution operations can be performed simultaneously at the speed of light [37, 46]. This approach leverages the inherent parallelism of light enabling the passive processing of a vast amount of data without increasing computation time [35, 42, 37]. This unique optical capability circumvents scalability issues when handling high-resolution images in traditional electronic-based CNN systems.

However, a challenge to all optically-implemented CNN approaches is that nonlinear layers are interspersed with the linear layers. For example, AlexNet (a standard CNN structure) consists of five convolutional layers followed by three fully connected layers [47]. Without the particular nonlinear layers that are effective in CNNs (e.g., ReLu), the classification ac-

curacy of the CNN drops by about 20% [48]. The nonlinear layers cannot be implemented using simple lens-like optics; to implement them optically, some physical nonlinearity must be introduced, for instance by using an atomic vapor cell [38, 49] or image intensifier [50]. Hybrid approaches involving repeated transduction of the signal to perform linear operations in optics and nonlinear operations in electronics provide little benefit due to large latency and power consumption in signal transduction [37, 50, 41]. Implementing only one of many required convolution operations does not provide much benefit in terms of speed and latency. Alternatively, there have been recent breakthroughs in using end-to-end designs for physical and hybrid networks designs which perform image classification or other tasks without explicitly using convolution [51, 35, 52, 53]. Such an approach can effectively implement multiple linear layers in one optical frontend. While novel, these end-to-end neural networks are computationally expensive to train and are applicable only to the physical system for which they were specifically designed.

In this work, we experimentally demonstrated a hybrid optical-electronic CNN consisting of a single optical convolution layer with an electronic single fully connected layer to achieve similar accuracy as AlexNet on hand-written digit classification tasks. To overcome the limitation from the absence of optical nonlinearity, we applied knowledge distillation to remove the nonlinear layers, and compressed multiple layers into a single linear layer [48]. Knowledge distillation circumvents the need for nonlinearity without a significant reduction in the performance by transferring knowledge from a larger, pre-trained network (the 'teacher' network) to a more compact network (the 'student' network). Here, we use a modified AlexNet, denoted AlexNet-Mod, as the teacher network and a single convolutional layer coupled with a single fully connected layer as the student network. We use this architecture to demonstrate a hybrid meta-optical platform, wherein an optical frontend based on a single meta-optic performs the linear convolution operation, followed by an electronic backend which contains a linear calibration layer and a fully connected layer. In such a way, the most computationally expensive operation is performed optically to leverage the benefits of optical computing, namely high spatial bandwidth and low power consumption. The use of a single meta-optic

layer drastically simplifies the experimental setup and provides a compact geometry.

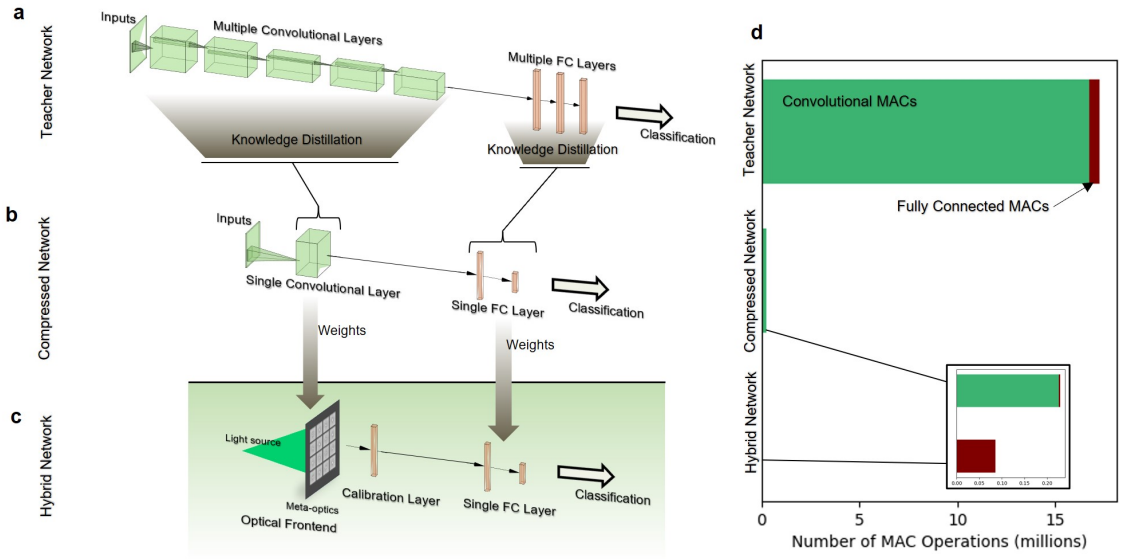

Figure 5.10: Schematic of convolutional neural networks for image classification tasks. (a) All-electronic multi-layered CNN. (b) All-electronic compressed CNN. (c) Hybrid CNN which combines an optical meta-optic front end and electronic backend. (d) The number of multiply-accumulate (MAC) operations of each network configuration, with convolutional MACs in green and fully-connected (FC) MACs in brown.

The optical frontend of this network is realized using inverse-designed meta-optics. Here, we designed meta-optics to realize a phase mask which performs the desired convolutional steps of the CNN by engineering the PSF. The hybrid CNN is described in Figure 5.10, where we compare the architectures of multi-layer electronic CNNs, compressed electronic CNNs (a linear single layer CNN), and our hybrid system. The number of multiply-accumulate (MAC) operations in the entire network is reduced by over two orders of magnitude through compressing multiple convolutional layers into a single layer and implementing them optically. The classification accuracy of the compressed hybrid CNN is reduced by only 5% from AlexNet-Mod (98% accuracy) to achieve 93% classification accuracy on the MNIST dataset.

5.4.2 Compressing Multiple Convolutional Layers using Knowledge Distillation

In each convolutional layer of a CNN, an optimized kernel is convolved with the input to generate a feature map which is then passed to the next layer. Using the knowledge distillation approach, we optimized eight convolutional kernels (each 6×6 pixels in size) for the MNIST dataset of handwritten digits. This is in stark contrast to AlexNet, which uses over 300 kernels [33]. However, complex models are prone to overfitting, and optically implementing a large number of kernels intruduces many practical challenges so we limit the number of kernels to eight in this work.

To obtain a network that could be implemented optically, we used knowledge distillation to compress a AlexNet-Mod as a base model. AlexNet-Mod consists of 5 convolutional layers and 3 fully connected layers (8 total layers) which we compress to the desired structure of one convolutional layer and one fully connected layer (2 layers). The knowledge distillation approach assumes that the teacher network is already trained and performs the desired task with high accuracy; in this case, we use AlexNet-Mod as the teacher network, which achieves 98.9%$\pm$ 0.33% on training and 98.4%$\pm$0.32% on testing classification accuracy MNIST datasets over repeated trials. Additionally, AlexNet-Mod employs nonlinear activation functions (ReLU) to optimize performance; these are circumvented by knowledge distillation for a result that is compatible with our optical setting. After training, the compressed electronic network achieves an approximate classification accuracy of 96% on both training and testing datasets.

5.4.3 Optical Convolution using Meta-Optics

The optical component of this network is implemented using inverse-designed meta-optics. In short, each sub-optic (of the single-layer set of meta-optics) is designed to have a point spread function (PSF) that resembles the convolutional kernel. Then, a convolution is performed automatically simply by imaging with that optic. This concept is explained generally first, and then I provide the details of the optics designed specifically for this work.

Explanation of PSF and Convolution

The point spread function (PSF) of a lens-like imaging system describes how the system focuses point sources. Simply, for an input point source, $PSF(x, y)$ is the amplitude of the electric field measured in the image plane. A perfect imaging system focuses light from a point source back to a point, mathematically represented by a delta function $\delta(x, y)$. More generally, for realistic lenses which have a PSF of finite size, we can denote $PSF(x, y)$ to describe the point spread function. Further, the PSF may be spatially-varying; that is, a point source located at (x_1, y_1) may produce $PSF_1(x_1, y_1)$ which is different (not simply translated) from $PSF_2(x_2, y_2)$ which is a measurement of a different point source located at (x_2, y_2). However, here we assume that a spatially invariant PSF is sufficient to describe our optical system and therefore are concerned with only a single $PSF(x, y)$ for each optic.

In Fig. 5.11a, we illustrate an input point source which produces an arbitrary example PSF in Fig. 5.11b. In a realistic lens system, the PSF is broadened from a delta function and may or may not be symmetric. For a more complex input object (for example, a two-dimensional image rather than a single point source), we can represent the light intensity in the object plane as an array of point sources denoted $O(x, y)$, illustrated in Fig. 5.11c. Then, the intensity in the image plane $I(x, y)$ produced by the optic is

$$I(x_0, y_0) = \int_{-\infty}^{\infty} \int_{-\infty}^{\infty} O(x, y) PSF(x_0 - x, y_0 - y)\, dxdy \tag{5.3}$$

For the case of a perfect lens $PSF(x, y) = \delta(x, y)$, we retrieve the expected output

$$I(x_0, y_0) = \int_{-\infty}^{\infty} \int_{-\infty}^{\infty} O(x, y) \delta(x_0 - x, y_0 - y)\, dxdy = O(x_0, y_0) \tag{5.4}$$

The convolution of continuous one-dimensional functions $f(x)$ and $g(x)$, denoted $f * g$, is defined by [54]

$$(f * g)(x_0) = \int_{-\infty}^{\infty} g(x) f(x_0 - x)\, dx \tag{5.5}$$

and is straightforwardly extended to two-dimensional continuous functions as

$$(f * g)(x_0, y_0) = \int_{-\infty}^{\infty} \int_{-\infty}^{\infty} g(x, y) f(x_0 - x, y_0 - y)\, dxdy \tag{5.6}$$

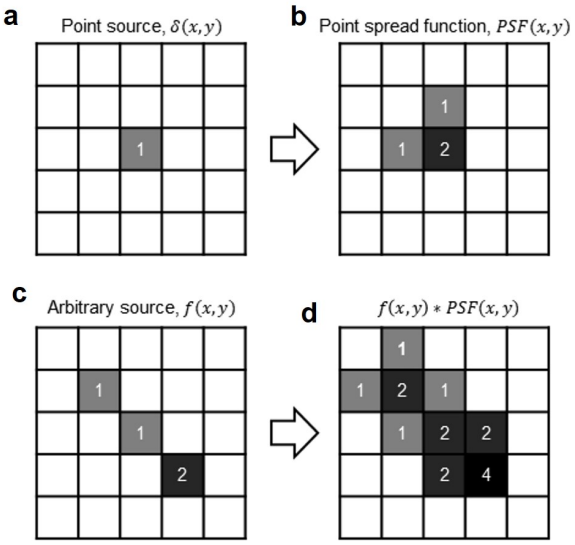

Figure 5.11: PSF and convolution illustrated with discrete matrices. (a) Illustrates a point source. (b) Represents an arbitrary PSF which may be obtained by imaging (a) through a realistic lens system. (c) An arbitrary source, or input image, which is an array of point sources. (d) The expected image produced by imaging the arbitrary source (c) through the lens system with PSF shown in (b).

Therefore, noting the similarities between Eqns. 5.3 and 5.6, we observe $I(x_0, y_0) = (O * PSF)(x_0, y_0)$. That is, the image produced by an optic is the input object convolved with the lens PSF.

Analogously, the two-dimensional discrete convolution is defined

$$(f * g)[n, m] = \sum_{j=-\infty}^{\infty} \sum_{i=-\infty}^{\infty} f[i, j] \cdot g[n - i, m - j] \tag{5.7}$$

And therefore we have, for discrete input $O[n, m]$ and discrete point spread function $PSF[n, m]$,

$$I[n, m] = \sum_{j=-\infty}^{\infty} \sum_{i=-\infty}^{\infty} O[i, j] \cdot PSF[n - i, m - j] \tag{5.8}$$

Figure 5.11d demonstrates a discrete convolution between an arbitrary input source (Fig. 5.11c) and optic PSF (5.11b).

In a convolutional neural network (CNN), the discrete convolution operation is used to extract features from an input image. The input is convolved with optimized kernels (or "filters") to produce an output with reduced dimensionality that is fed to the next layer in the network. In this work, we perform this convolution optically, with the (discrete) kernel analogous to our (continuous) optic PSF.

Meta-optics Specifications

In designing the optics, there are a wide range freedoms to choose parameters such as operating wavelength, optics size, desired PSF size, focal length, and meta-optic scatterer. We considered these choices carefully explain our rationale here, but many other possible configurations may also yield viable results.

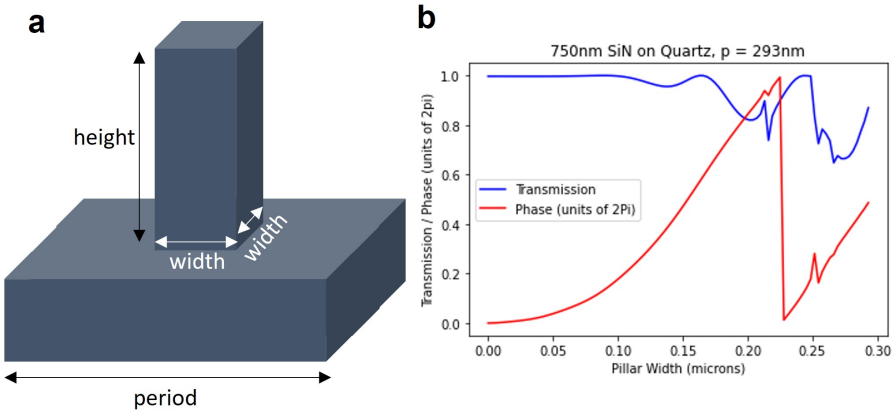

Figure 5.12: Scatterer response. (a) Diagram of the scatterer unit cell. The unit cell consists of a rectangular pillar of fixed height and variable width, sitting on a lattice of fixed period. (b) The simulated unit cell phase and transmission as the pillar width is changed, for fixed wavelength of 525 nm. A subset of unit cells with widths ranging from 80 nm to 225 nm were chosen to provide 0 to 2π phase coverage (red) which high transmission (blue).

The hybrid CNN can be adapted to operate at any wavelength; in this case, we chose 525

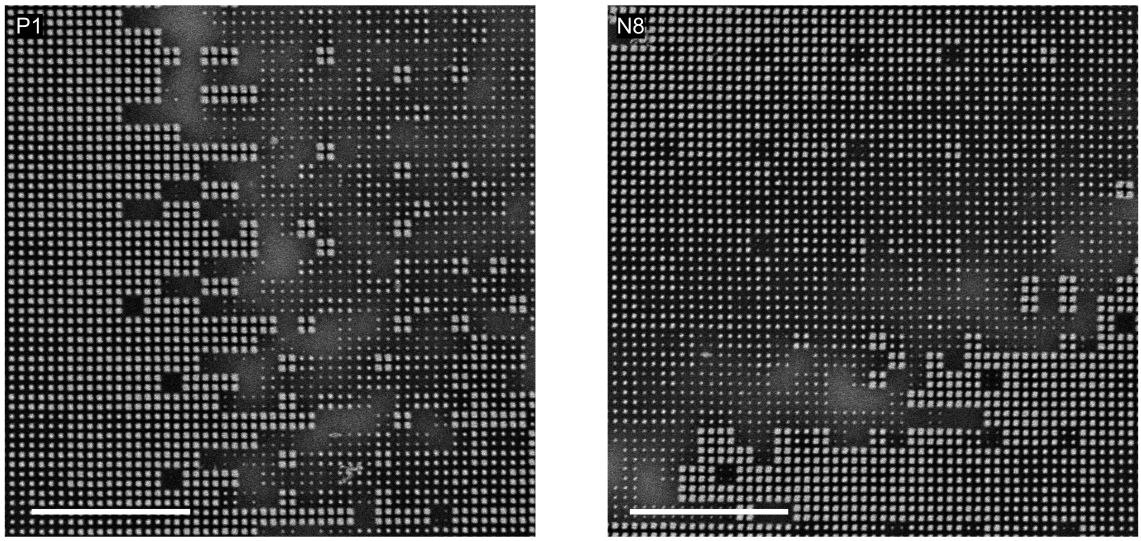

Figure 5.13: High-resolution SEM images of the scatters from the meta-optics. (a) Section of the meta-optic corresponding to the positive part of kernel number 1. (b) Section of the meta-optic corresponding to the negative part of kernel number 8. Scale bar: 5 μm.

nm to best align with the available light sources and camera sensitivity. The camera used in experiment is Allied Vision Prosilia GT1930C with 5.86 μm per pixel resolution. Based on these factors, we set the simulation grid size to 586 nm such that 10 simulation pixels = 1 camera pixel, and the simulation grid size is comparable to the operating wavelength. For phase mask propagation, deeply subwavelength pixel size is unnecessary and would increase the computational load of designing the phase masks. The meta-optic unit cells, however, are situated on a deeply subwavelength lattice size of 293 nm (exactly 1/2 simulation pixel size).

The optimized phase are physically realized as arrays of sub-wavelength scatterers. To be evenly divisible by the simulation grid size, we chose scatterer periodicity of 293 nm. The chosen scatterers are 750 nm tall square SiN pillars on quartz substrate, with pillar

widths ranging from 80 nm to 225 nm, as illustrated in Figure 5.12(a). The quartz substrate functions primarily as structural support for the pillars and is transparent at the wavelength of interest. We calculate the phase and transmission response of these scatterers using rigorous coupled wave analysis (RCWA), specifically the S4 implementation [11], as shown in Figure 5.12(b). By adjusting the scatterer width, phase shifts covering a 0 to 2π range can be achieved with high transmission. This phase-pillar width response was then used to map the optimized phase masks to physical geometries. In this case, each phase mask pixel (586 nm) corresponds to a 2×2 block of scatterers. The individual pillars are shown in high-resolution SEM images of the fabricated devices in Fig. 5.13).

Each optic was designed to produce an image of a particular convolutional kernel as its PSF. As described in the earlier sections, each electronic convolutional kernel is a 6×6 matrix which contains both positive and negative values. Since negative values cannot be represented when measuring the amplitude of the electromagnetic field on the camera sensor, we separated the kernels into two matrices, each also 6×6, one containing only the positive values and the other containing the (absolute value of) negative values. We present these electronic kernels, separated into positive and negative parts, in Fig. 5.14(a). The desired PSF was defined by shrinking one of these kernel matrices to the desired size and padding the remaining space with zeroes. So that the PSF remains point-like, it is desirable to shrink the PSF image as small as possible (down to a minimum resolution where one PSF "pixel" = one camera pixel). However, such a design would not be robust; to guard against misalignments, we defined the desired PSF to be such that each PSF "pixel" would correspond to 2x2 camera pixels and therefore the desired PSF image is 70.32 μm $\times$ 70.32 μm in physical size.

Finally, we chose the size of each kernel optic to be 468.8 μm (800 simulation pixels). A larger optic allows for more light collection and therefore higher SNR, but also undesirably increases the total optic footprint, so the chosen size reflects a tradeoff between these two factors. The focal length was chosen to be 2.4 mm based on our ability to place the optics as near the camera sensor as possible while allowing room to adjust the focal length and alignment to obtain the best image.

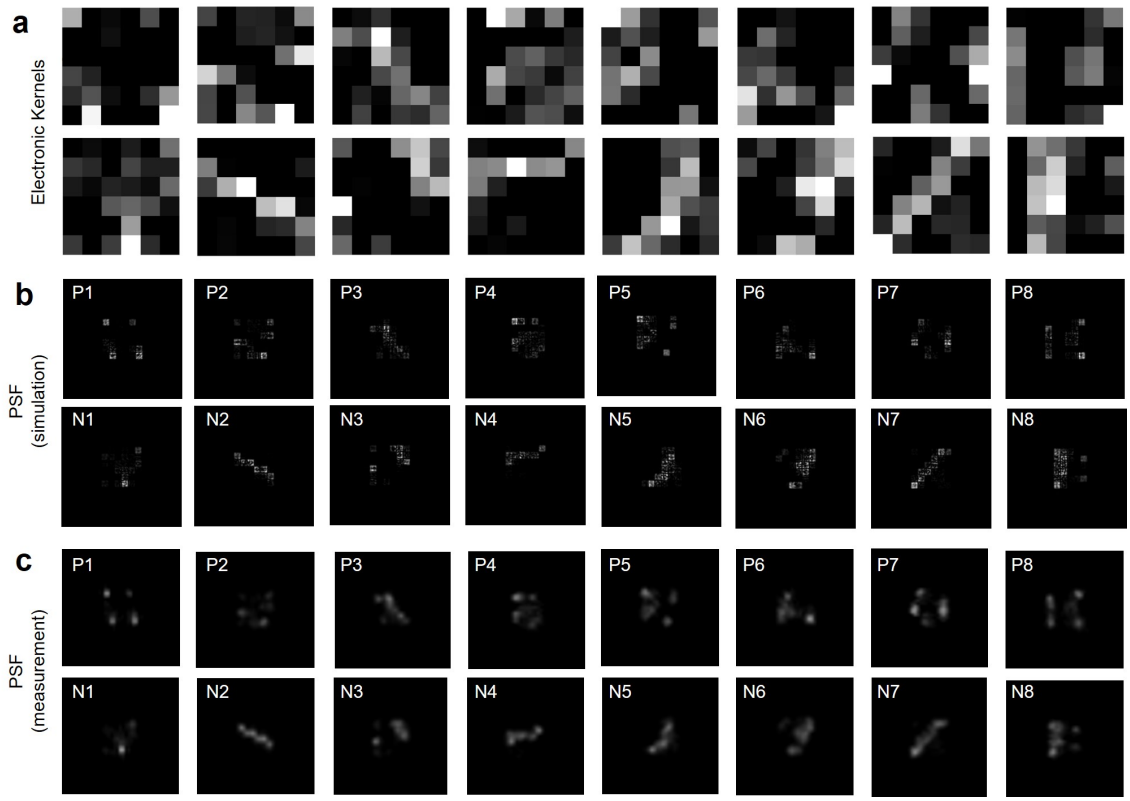

Figure 5.14: The convolutional kernels and corresponding PSFs. (a) The positive (top) and negative (bottom) parts of all eight convolutional kernels. Each kernel is a 6 by 6 matrix. (b) The simulated PSF results at imaging distance 2.4 mm for the positive (top) and negative (bottom) sub-optics. (c) The experimentally measured PSF.

Phase Mask Optimization

Once the desired PSF is defined, we aim to determine the phase required to produce it, modeling the meta-optic as a phase mask 2.4 mm in front of the desired plane. This is effectively a holography problem; both the input light and the desired PSF are specified by electric field amplitude only, and the complex phase in a particular intermediate plane must be determined to map between the two. This problem is solvable by the well-known Gerchberg-Saxton (GS) algorithm [8]. Here, we provide the details of the implementation.

All simulations were done at a single wavelength (525 nm) and on a lattice grid of 586 nm.

The designed phase masks corresponding to the positive and negative parts of the eight convolutional kernels are shown in Fig. 5.15(a). To implement the phase retrieval, we initialize the phase mask guess ϕ as constant 0 phase and the input light U as a plane wave (constant amplitude 1). Therefore, the initial field after it passes through the optic is $U_O = Ue^{i\phi}$. Our implementation of the iterative steps is based on that in [55, 56]:

1. Propagate the initial field U_O to the image plane to obtain U_I.

2. Calculate $U_I' = |PSF|e^{i*\Theta(U_I)}$, where $|PSF|$ is the amplitude of the desired point spread function and $\Theta(U_I)$ is the phase of the complex field U_I.

3. Backward propagate U_I' to the object plane to obtain U_O'.

4. Calculate $U_O\text{“} = |U_O|e^{i*\Theta(U_O')}$, where $|U_O|$ is the amplitude of the field in the object plane; here, this is a plane wave.

The process is iterated by inputting $U_O\text{“}$ to U_O, ultimately retrieving the final phase $\phi_{final} = \Theta(U_O\text{“})$. This process is quick to converge, requiring only 20 iterations to retrieve the desired phase to our satisfaction. In this process, the propagation function is Fourier-based band-limited angular spectrum propagation [7].

Additionally, we developed our own phase mask optimization code in TensorFlow and fabricated a second set of optics corresponding to these phase masks. The experimental PSFs and an example convolution from both sets of optics are shown in Fig. 5.17(b) and (c). While both optics produce the desired PSFs and perform the desired convolution, the optics designed using the GS method exhibit brighter and slightly clearer images on the camera. Therefore, we conducted this experiment using the GS meta-optics. However, the TensorFlow code has not gone to waste; in our ongoing efforts to extend this work to more complex datasets, we require meta-optics that can implement convolutions on color images. That is, we need a single meta-optic that produces three different PSFs at three different

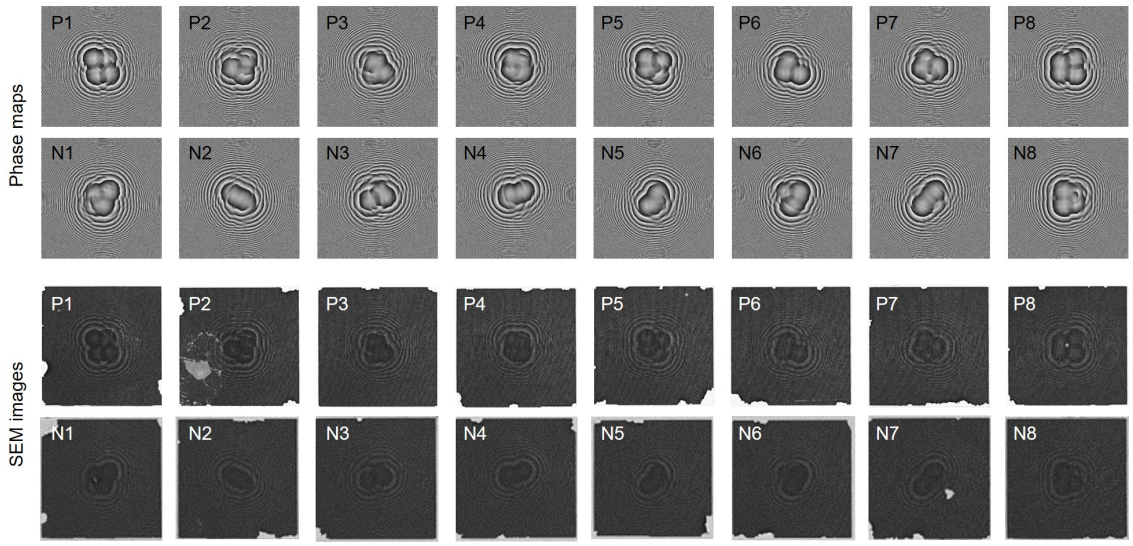

Figure 5.15: The designed meta-optics. (a) Optimized phase maps for each sub-optic. The phase values vary between 0 and 2π and each optic is 470 μm$\times$ 470 μm in size. (b) SEM images of all designed optics.

wavelengths corresponding to the red, green, and blue wavelengths of the display LEDs. Since the GS algorithm does not take the wavelength-dependent scatterer-phase mapping into account, it is insufficient to tackle this problem. In this new effort, we are using the TensorFlow code with a proxy function to map between scatterer and phase within the optimization loop.

For the TensorFlow based method, the Adam optimizer was used to optimize the phase mask. We model the input light U as a plane wave and again use the angular spectrum method to propagate the field to the desired plane. To facilitate faster convergence, we initialized the phase mask guess ϕ as the phase of the backward propagated PSF. Then, we iteratively updated the phase mask through the following steps:

1. Calculate the initial field $U_O = Ue^{i\phi}$, where U is the input plane wave and ϕ is the phase mask guess.

2. Propagate the initial field U_O to the image plane to obtain U_I.

3. Calculate the loss between the simulated image intensity $|U_I|$ and the desired field intensity $|PSF|$. To calculate the loss, we first L2 normalize both $|U_I|$ and $|PSF|$. We then calculate the difference between these two quantities, take the absolute value, and sum up the values in the difference matrix.

4. Update the phase mask.

This optimization continued for 500 iterations at a learning rate of 0.05. The phase masks designed using the TensorFlow method are qualitatively similar to those designed using the GS method in that they both exhibit lobe-like center structures and lens-like outer rings, but the TensorFlow optics exhibit slightly more randomness. We hypothesize that the TensorFlow-based optics exhibit more destructive interference than the GS-based optics, which is supported by the observation that the TensorFlow-based optics produce dimmer images.

5.4.4 Optical Experiment

The optical system is summarized in Figure 5.16. To verify the performance of the optics, we measured the PSF of each sub-optic using a single-mode fiber as a point light source, as shown in the Figure 5.16(a). The PSFs from all 16 sub-optics are simultaneously captured by the two-dimensional CMOS camera. Accordingly, the convolved images from all 16 sub-optics are also captured at the same time when we replaced the single mode fiber with the display, as described in Fig ure5.16(a). Exemplary electronic convolutional kernels, which represent the ground truth PSFs for the optically-implemented kernels, are shown in Figure 5.16(d). We also present the simulated PSFs from the meta-optics using angular spectrum propagation [6, 7]. The experimentally measured PSF shown in Figure 5.16(d) match well to the simulated PSFs, confirming fabrication accuracy.

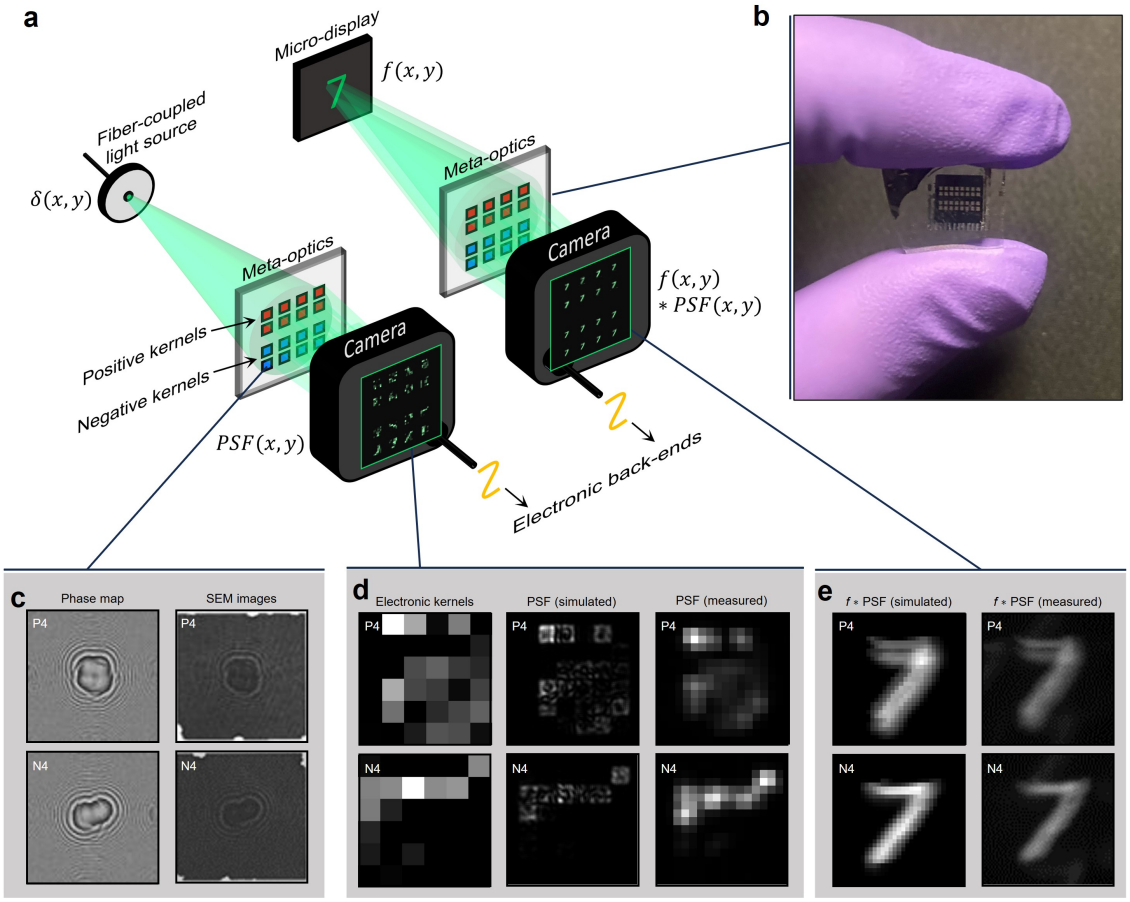

Figure 5.16: Schematic of the optical system. (a) PSF measurement setup using a monochromatic point light source (left) and optical convolution measurements using a micro-LED display (right). (b) A photograph of the fabricated meta-optics. The meta-optic contains 16 different sub-optics, spatially distributed in a single layer, operating in parallel for classification tasks. (c) Phase maps and SEM images of exemplary sub-optics corresponding to the positive and negative parts of a particular convolutional kernel. (d) The positive and negative parts of an example convolutional kernel (left) and the corresponding PSF simulation (middle) and right (experiment). (e) The simulated electronic output (left) and optical experiment (right) convolved output for the example kernel, for the case of an input "7" from MNIST.

In greater detail, all meta-optics are fabricated in a single layer, with different sub-optics corresponding to the different convolutional kernels. Since electronic convolutional kernels include both positive and negative values, we separated each kernel into positive and negative parts and designed meta-optics for each. The positive and negative images were computationally subtracted afterward to produce the net convolution. A photograph of the fabricated meta-optic is shown Figure 5.17a. In total, there are 32 sub-optics on the fabricated chip arranged in two sets of 16 (one set for each of the optimization methods). In each set, there is a positive and negative sub-optic corresponding to each convolutional kernel. Each kernel meta-optic is of size 470 μm $\times$ 470 μm and center-to-center distance of 705 μm. The optics are arranged in two rows of eight optics for a total footprint of 5.6 mm $\times$ 1.4 mm per set. In Figure 5.17b and 5.17c, we show the experiment output as it is captured on the camera. Figure 5.17b shows the PSFs of the optics that are designed to represent the convolutional kernels. In this image, the TensorFlow-optimized optics are on the left and the GS-optimized optics are on the right, with the GS-optimized optics producing brighter images. To perform convolution with an input image, the point source is replaced with a micro-LED screen; these results are shown for an example "5" in Figure 5.17c.

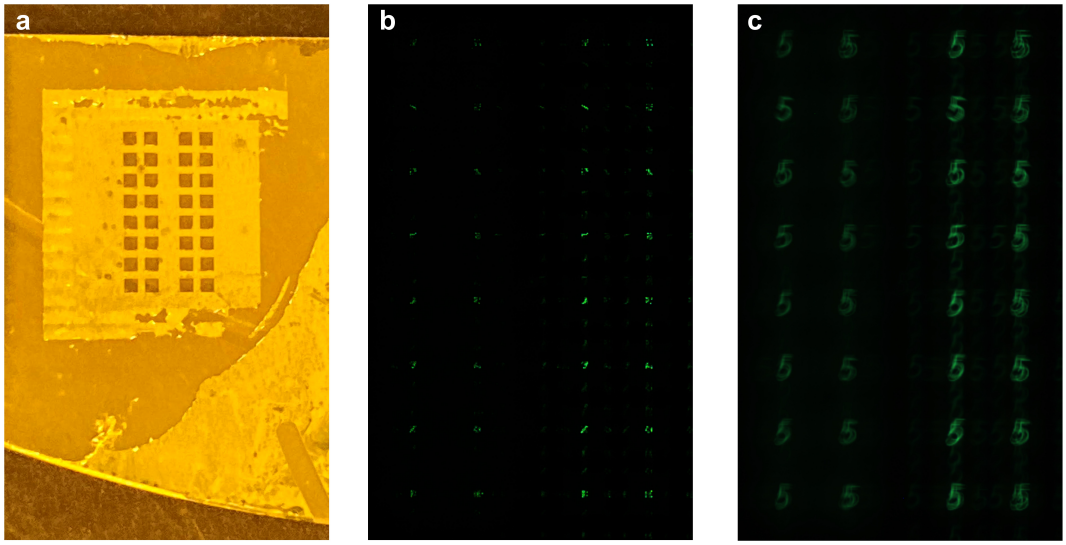

Figure 5.17: Multiple convolutional meta-optics on a single wafer. (a) Picture of the fabricated chip with a metallic aperture. (b) Measured PSFs of the meta-optics in a single shot. (c) Measured convoluted images from one of the MNIST datasets in a single shot. For both PSFs and convoluted images, 16 PSFs on the left are from the meta-optics designed by Tensorflow, and the other 16 PSFs on the right are from the meta-optics designed by the GS-algorithm, which were used with the computational backend for the classification experiment.

A further comparison between the convoluted images obtained in the experiment and the electronic convolution is presented in Figure 5.18. For a particular convolutional kernel (number 4), we illustrate the breakdown into positive and negative parts, as well as the net kernel (positive minus negative) in Figure 5.18a. In Figure 5.18b, we illustrate the optical experiment results obtained with the optic corresponding to this particular kernel. The negative image is computationally subtracted from the positive image to obtain the net result, shown at the right. Further, in Figure 5.18c, we compare the net electronic convolution (top row) to the net optical experiment convolution (bottom row). The results illustrate the effectiveness of the optical convolution, albeit with slight noise and differences

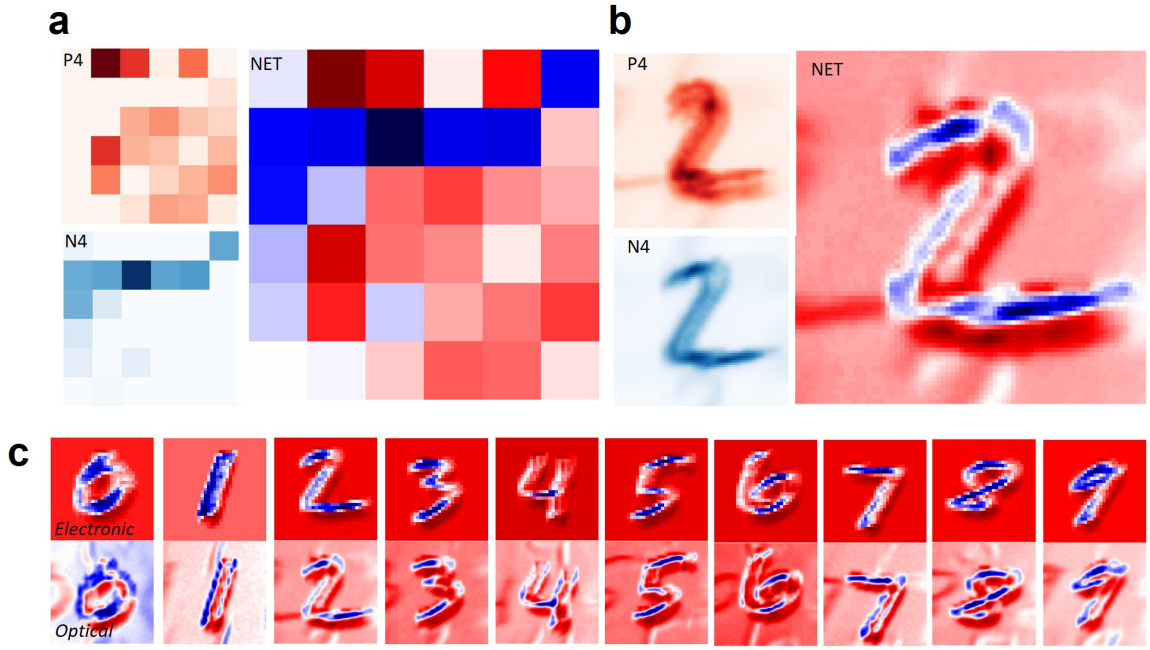

Figure 5.18: A sample of electronic and optical convolution results. (a) As an example, we plot convolutional kernel number 4, broken up into positive and negative parts as well as the net kernel with both positive and negative values. (b) The corresponding optical experiment convolution results for this kernel's positive (top) and negative (bottom) optics, as well as the computationally combined (right) net convolution. (c) A sample of MNIST digits convolved electronically (top) versus optically (bottom).

which are accounted for by the calibration function.

5.4.5 The Calibration Layer

To address noise and misalignments in the optical system that negatively affect classification accuracy, we introduce an additional fully-connected layer (called a "calibration layer") to shift the optical experiment results to the form expected by the electronic backend. For example, image centering and scaling issues could be corrected as well as calibrating the relative brightnesses of the positive and negative parts of the convolution. This additional

layer adds only 2,880 MAC operations but greatly improves the robustness of the hybrid network. The calibration layer was fine-tuned with only 10% of the training dataset and ensures that the computational backend does not need to be retrained. Therefore, the full electronic backend of the hybrid network consists of the calibration layer followed by the original compressed electronic backend.

We assert that the calibration layer only re-maps the optical representations and does not improve the performance of the electronic backend alone. To examine this, we further analyze the effect of the calibration layer and the overall performance of the hybrid network as compared to an all-electronic network using Principal Component Analysis (PCA).[3] PCA is a statistical method widely used in various fields, especially in analyzing the quality of neural networks [57], to project original, high-dimensional data into a new, simpler coordinate system for explicit interpretation. Specifically, PCA computes the eigenvalue decomposition of the covariance matrix or the singular value decomposition of input data to determine the principal direction (known as "principal components"). Principal component 1 denotes the axis of maximum variance, encapsulating the most substantial relationships among variables, while principal component 2, orthogonal to principal component 1, captures the second most significant variance direction. Notably, the first two principal components typically contain the most crucial information. In this study, we compress the output dimensions from electronic and optical convolutional layers into two principal components, respectively, to compare the classification efficacy of each approach; this is observed by comparing the clusters observed in PCA visualizations [58].

In Fig. 5.19, we use PCA to show that the raw experimental data do identify the fundamental components necessary for classification, but that the calibration function is necessary to shift optical representations to a form that is compatible with the pre-designed electronic backend. As shown in Fig. 5.19a and 5.19c, we observe that both the all-electronic CNN outputs and the uncalibrated hybrid network experimental results can effectively distinguish

[3]This analysis was completed by Jinlin.

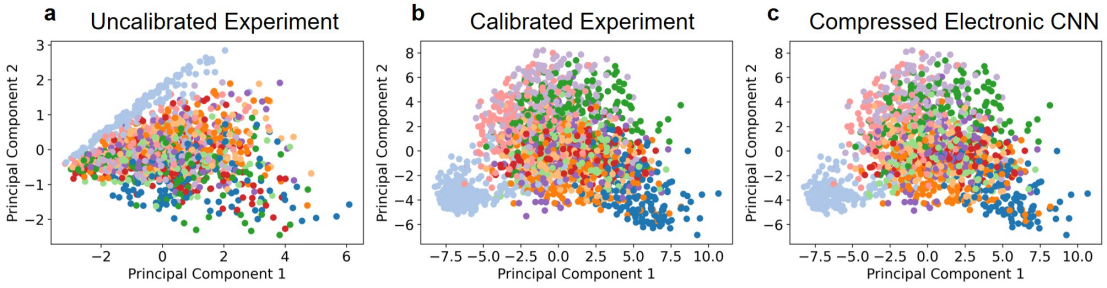

Figure 5.19: PCA of the hybrid CNN. (a) PCA of the uncalibrated experimental hybrid CNN classification data. (b) PCA of the calibrated experimental data, which has been re-mapped and exhibits clustering behavior similar to that of the compressed electronic CNN data. (c) PCA of the compressed electronic CNN data.

between different classes due to the clustering behavior of specific classes, e.g. light blue and navy blue. This clustering behavior indicates that despite any observable shifts in the PCA plot, the fundamental capacity of the hybrid network to classify data remains comparable to that of all-electronic networks. However, due to differences between the optical experiment output and the expected input to the electronic backend, directly using the original backend network results in a notable drop in accuracy, down to 16.3%. The calibration layer is designed to re-calibrate the outputs from the optical convolution layer back to the original outputs, thereby enabling the use of the original backend without retraining. As shown in Fig. 5.19b and 5.19c, the calibrated experiment result exhibits very similar clustering behavior to the all-electronic network, further demonstrating that the hybrid network classification is comparable to that of the all-electronic network.

5.4.6 Classification Results

The classification accuracy and MAC operations for the three network architectures (AlexNet-Mod, compressed electronic network, and hybrid optical-electronic network) are presented in Table 5.1. AlexNet-Mod achieves classification accuracy exceeding 98% on both training

and testing datasets. The number of MAC operations of this network is 17 million with 8 bit precision. The compressed electronic CNN achieves greater than 96% accuracy; this 2% decline reflects the inherent challenges of compressing multiple layers into a single layer. Primarily due to the compression of the convolution layers, the number of MAC operations is reduced to 228,672. The hybrid network, which integrates the optical convolution layer with the calibration layer and single fully connected layer electronic backend, experimentally achieves classification accuracy of 93.9% ($\pm$ 0.25%) and 93.4% ($\pm$ 0.22%) on the training and testing datasets, respectively, and requires only 85,824 MAC operations, which is 0.5% and 37% of that required for AlexNet-Mod and the compressed electronic networks, respectively.

Table 5.1: Classification Results

Network Architecture	Train (%)	Test (%)	MAC Operations
AlexNet-Mod	98.9 $\pm$ 0.33	98.4 $\pm$ 0.32	17,268,224
Compressed electronic CNN (without KD)	84.2 $\pm$ 0.47	82.1 $\pm$ 0.69	228,672
Compressed electronic CNN (KD)	97.2 $\pm$ 0.35	96.2 $\pm$ 0.29	228,672
Hybrid CNN (KD)	93.9 $\pm$ 0.25	93.4 $\pm$ 0.22	85,824

The number of MAC operations required of a network serves as a metric of computational complexity which is independent of the employed hardware technology. In a modern digital system, one MAC operation consumes approximately $1pJ$ [53, 50], so the hybrid network is expected to reduce the required power to classify an input from $17\mu J$ to $85nJ$ based on the reduction in MAC operations. The latency of such a classification task is also expected to decrease proportionately. For input which is already in the optical domain, the power and latency required to capture an image and convert it to digital input is the same regardless of the network. Specifically, the hand-written digits of MNIST were captured using a standard camera, and the optical frontend of our network uses a standard camera sensor with meta-

optics replacing the refractive camera lens.

The benefit of optically implementing the convolutional step becomes more significant as the number of input pixels is increased. The electronic computational complexity of each convolutional layer is determined by the height and width of the input images (H, W), as well as the size of the kernels (k), and is $\mathcal{O}(HWk^2)$ [48]. However, the computational complexity decreases to $\mathcal{O}(1)$ in the optical convolutional layer. For example, when the MNIST dataset's typical image size of 28×28 pixels is increased to 100×100 pixels, the electronic computational complexity of each convolutional layer is expected to increase 12.76 times (assuming the kernel size remains unchanged), but an optically implemented convolution would not incur any increase in computation time. Therefore, as the resolution of real-world images continues to increase, hybrid networks such as the one described offer a promising solution to scaling problems incurred by all-electronic networks.

5.4.7 Advantages and Limitations on the PSF Engineering Approach for Convolution

We emphasize two advantages of our PSF-engineering method to perform optical convolution. Firstly, we highlight the simplicity of the optical system, as this method requires only a display, a single layer of optic, and a camera, making it compact and simple to execute. Incoherent illumination is used, so this approach can be applied to real-world image classification scenarios. Secondly, we highlight the ease of integration with the optimized electronic system. One of the challenges faced by optical computing is that electronic computing is already extremely powerful, having had decades of research and development into algorithms and hardware [35]. In our approach, the optics are designed to implement the electronically-optimized kernels. These kernels may be modified to reflect improvements in electronic CNN models and architectures, and the optics can accordingly be adapted to implement convolutions with arbitrary kernel matrices.

Furthermore, the Gerchberg-Saxon (GS) algorithm [8] used to design the optics is a well-established technique. The GS algorithm is an iterative phase retrieval algorithm to determine the phase (in the optic plane) that produces an intensity pattern in another

desired plane (the focal plane). In other words, the meta-optics are phase-only holograms producing the desired PSFs as their images. Due to the fact that only amplitude, and not phase, contributes to the intensity pattern, the iteratively designed phase masks are not unique.

There are, however, two major limitations of the PSF-engineering approach. One limitation is that there is no guarantee that the desired PSF is physically realizable. That is, a single phase mask that satisfies the desired amplitude constraints may not exist. However, by introducing an electronic calibration layer, the resultant PSF does not need to be perfect in order to effectively classify the data. Alternatively, to ensure physically realizable PSFs, one could adopt an end-to-end optimization scheme wherein the phase mask is simultaneously optimized with a backend. However, training this large phase mask (on the order of $10^5 - 10^6$ unit cells per kernel optic) is prohibitively costly and the design space is potentially too large to attain convergence. In contrast, separately training the electronic convolutional kernels and the optics are both reasonable steps, which as demonstrated are effective when combined.

A second limitation of the described approach is that we assume the PSF is spatially invariant. In reality, light from different spatial locations on the imaging object intersects the meta-optic at various angles of incidence, resulting in a different PSF for the off-axis rays. In contrast, we design the optics assuming a normal incident illumination. To mitigate this discrepancy, we ensure the incoming angles of incidence are relatively small by placing the display far away from the optics (90 mm) relative to the focal length (2.4 mm). Therefore, for a displayed image size of 8 mm $\times$ 8 mm, we ensure that the maximum deviation from normal incidence is 3.6°, and therefore the assumption of spatial invariance is reasonable for our system. However, for a large field of view imaging system, we may need to explicitly model the spatially varying PSF. We note that Wei et al. [46] use reparameterization techniques to design spatially varying kernel optics and report higher classification accuracy using this method (73.8%) versus designing optics with the assumption of spatial invariance (71.6 %) on the CIFAR-10 dataset. In another variation of a PSF-engineering technique, Zheng et al.

[59] engineer the PSF of polarization-sensitive meta-optics to provide an array of focal spots which produce images of intensities relative to the kernel weights.

Chapter 6

DOUBLETS

We have developed a number of meta-optic doublet systems with the aim of achieving a meta-optical system with larger field of view, higher quality broadband imaging, or both. Doublet systems are highly successful at increasing the field of view. To this end, I present our results on two doublets for wide field of view: one for LWIR (Section 6.1) and one for visible (Section 6.2) wavelengths. We have also used a meta-optic doublet system to steer and collimate light from a photonic integrated circuit (PIC) as part of a hybrid spatial light modulator; this effort is discussed in Section 6.3. These doublets designs all worked very well and resulted in publications.

We have attempted to inverse design doublets for broadband imaging applications in both the MWIR and LWIR. Despite several attempts, these devices never performed as desired in experiment. The results are presented in Section 6.4 and I discuss my conclusions regarding doublet systems in Section 6.5.

6.1 LWIR Large Field of View

I begin with a pseudo-doublet: a large field of view system consisting of a meta-optic with an external aperture. This was my first independent project at the Majumdar Lab. The contents of this chapter are adapted from [60]: *Anna Wirth-Singh, Johannes E. Fröch, Zheyi Han, Luocheng Huang, Saswata Mukherjee, Zhihao Zhou, Zachary Coppens, Karl F. Böhringer, and Arka Majumdar. Large Field-of-View Thermal Imaging via All-Silicon Meta-Optics. Applied Optics* ***62****, 20, https://doi.org/10.1364/AO.493555, July 2023*, with permission from the authors.

Relative to visible and near-infrared wavelengths, the regime of mid- to long-wave infrared

large field of view (FoV) meta-optics has been relatively unexplored despite numerous applications for ultrathin LWIR lenses. From Planck's Law, the emission from thermal sources with temperatures in the range of 0°C to 100°C has a maximum in its spectral intensity distribution in the long-wave infrared range (LWIR, 8-12 μm). Hence this spectral range is commonly used to achieve high temperature contrast with high detection efficiency for thermal imaging. Particularly for some night vision applications, this capability is critical to identify objects from their environment or to sense small temperature differences.

At the same time, surveillance and imaging applications typically benefit from large field of view which allows a wide scene to be captured in a single frame. To achieve large FoV using traditional refractive optics, multiple lenses are often used to correct for Seidel aberrations, which leads to excess size and weight [61, 62]. However, reduced size and weight are often crucial requirements for mobile or miniaturized systems, such as night vision goggles or airborne remote sensing. Weight reduction in particular is challenging for such systems because the optical elements necessary for the above mentioned applications typically require larger apertures to achieve low f-number and to compensate for low signal intensities to facilitate imaging over larger distances. Therefore, the flat nature of meta-optics is particularly applicable to such scenarios where it is desirable to have large aperture without negligible added weight.

One approach towards realizing large FoV lenses is to use an external aperture to restrict incoming light such that beams of different angles of incidence interact with different parts of the meta-optic. Hence, each part of the meta-optic only needs to be optimized for a narrow range of angles of incidence. While reducing the diameter of the entrance aperture increases the spatial separation of the light, it also reduces the input light into the system and therefore the signal-to-noise ratio. This approach has been used to demonstrate very large FoV in the mid-wave infrared (near 170° at 5.2 μm wavelength), but for an extremely small entrance aperture of 1 mm ($\sim 200\lambda$) [63].

Following a similar approach, in this work we experimentally demonstrated an all-silicon large FoV meta-optic in the LWIR range. Our optical system has an aperture of 1 cm

($\sim 1000\lambda$), whereas the meta-optic itself has an aperture of 3 cm. LWIR meta-optics, including all-silicon meta-optics, have previously been demonstrated [64, 65, 66], but wide FoV was not reported until after this work was published, when Lin et al. [67] used a very similar approach involving an aperture and meta-optic to achieve wide field of view. In that work, they argue for the utility of a ZnS spacer between the aperture and the optic to improve performance.

6.1.1 Design

The large-scale configuration of the aperture and the design of the phase mask were optimized using Zemax OpticStudio. In detail, as shown in Figure 6.1a, we assume an entrance aperture of 1 cm, chosen to balance the trade-off between light collection (requiring larger apertures) and achieving spatial separation of rays for different angles of incidence (favoring smaller apertures). The phase profile was assumed to be radially symmetric, of the form

$$\Phi = M \sum_{i=1}^{12} A_i \rho^{2i} \tag{6.1}$$

where M is a normalization constant, ρ is the normalized radial coordinate, and A_i are polynomial coefficients. We defined input fields at incident angles of 0°, 10°, 20°, 30°, and 40°, while the polynomial coefficients A_i and the aperture-meta-optic distance were simultaneously varied to minimize the angle dependent spot sizes (all weighted equally). At the optimal aperture-meta-optic distance of 0.9 cm, the meta-optic diameter must be at least 3 cm to capture all the incident rays through the aperture to achieve a FoV of 80°. In other works [68, 67], a spacer with higher refractive index was used between the aperture and the meta-optic, reducing the spatial separation of beams at larger FoV, thus reducing the necessary diameter of the optic. However, we did not take this approach to maintain a lightweight design. The arrangement of the optimized aperture-meta-optic system is shown in Figure 6.1a. The designed system has a Strehl ratio of 0.11 as calculated by the Huygens PSF in Zemax.

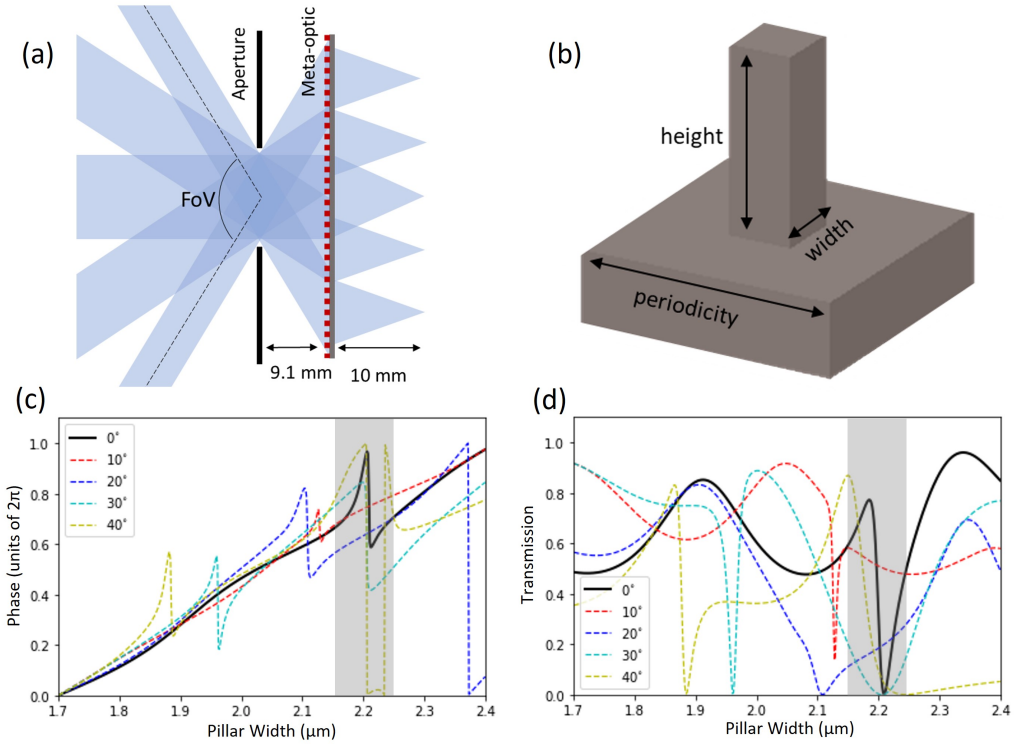

Figure 6.1: Lens system design. (a) Schematic illustrating the entrance aperture and the meta-optic, with the path of light rays depicted by shaded blue regions. (b) Meta-atom schematic. The meta-optic consists of a periodic array (fixed periodicity) of square pillars of uniform height and variable width. (c) Scatterer phase and (d) transmission responses calculated using rigorous coupled wave analysis, for various angles of incidence. Pillar widths in the gray shaded region were excluded to ensure reasonable transmission.

To implement the optimized phase profile in an all-silicon (n = 3.47 at 10 μm [69]) meta-optic, we used square-shaped pillars, which are arranged in a square lattice, schematically shown in Figure 6.1b. Based on parameter sweeps for periodicity, height, and width of the pillar, using rigorous coupled wave analysis (RCWA) [70], we set the dimensions to a height of 10 μm and lattice periodicity of 4 μm. The phase shift and transmission of the scatterer as a function of width are shown in Figures 6.1c and 6.1d, respectively, for normal and

off-axis angles of incidence. We use pillars of widths between 1.7 and 2.4 μm to achieve the full 2π phase coverage and excluded the post widths in the grey shaded region to avoid low transmission. We find that the phase dispersion with respect to the incident angle is relatively small as shown in Figure 6.1c. Hence, we used the phase response for normally incident light to map the pillar geometry to the optimized phase distribution.

6.1.2 Fabrication

We fabricated the 3 cm diameter meta-optic in a 300 μm thick, double-side polished silicon wafer. First, we deposited an on-chip metal aperture to eliminate stray light passing through the wafer outside the meta-optic. We spin-coated a negative photoresist (NR9G-3000PY) and wrote the aperture pattern by direct laser write lithography (using Heidelberg DWL-66+) and development in AD-10 developer. We then evaporated 10 nm Cr and 100 nm Au via an e-beam evaporator (CHA Solution) and lifted off in acetone to complete the on-wafer aperture. Then, to fabricate the meta-optic pillars, we spin coated a positive photoresist (AZ-1512) and again used direct laser write lithography (Heidelberg DWL-66+) followed by development in AZ-726 developer to pattern the optic. The pattern was then transferred into the underlying silicon using deep reactive ion etching (SPTS Rapier), which was timed to etch $\sim$ 10 μm into the silicon. Finally, oxygen plasma (YES CV200 RFS) was used to strip residual photoresist. A camera image of the fabricated meta-optic wafer is shown in Figure 6.2a. A scanning electron microscope (SEM) image of the fabricated device from a top-down view is shown in Figure 6.2b, which shows a section of pillars arranged according to the design. Further inspection at an oblique angle (Figure 6.2c) shows nearly vertical sidewalls.

Both devices on the wafer have an identical design, and were fabricated for redundancy. However, in experiment, we noted that one of the optics ("Lens 1") had worse optical performance; see Figure 6.3. In particular, Lens 1 exhibits a double image. After eliminating all possible sources of the double image, such as reflections from the optical table, we concluded that the double image originates from the optic itself. Upon observing similar behavior

in other laser-written optics (but not in e-beam-written optics), it became apparent that striping inconsistencies cause the double image, as discussed earlier in Chapter 3. Due to inconsistent exposure within the width of an exposure stripe, the laser writer imprints and undesired grating which diffracts some of the light off-axis. In this case, the effect was worse in Lens 1 than in Lens 2, so all data presented in the publication was taken with lens 2.

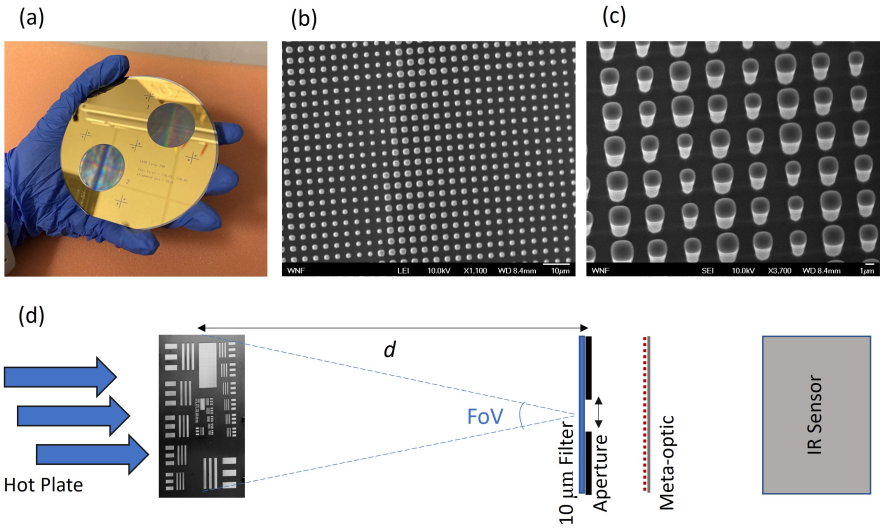

Figure 6.2: Device fabrication and characterization. (a) Photograph of the fabricated device. (b) Top-down scanning electron microscope (SEM) image of the fabricated device, and (c) the same device zoomed in and from a slightly oblique viewing angle. (d) Schematic of the experimental setup to characterize the meta-optic.

6.1.3 Measurements and Results

The measurement setup is depicted in Figure 6.2d. A thermal radiation source (hot plate at 65°C) was placed in front of a matte black paint-coated aluminum stencil target (the imaging object). For demonstrating image quality, the target pattern was the 1951 USAF resolution chart scaled up by a factor of 2.5, with the cut-out area extending 12.5 cm wide and 11.5 cm tall. Thus, to demonstrate 80° FoV imaging, we placed the object at a distance

of 7.45 cm from the aperture of the imaging system such that the light from the outermost feature was 40° relative to normal incidence. The imaging system included the 1 cm external aperture (a thin aluminum sheet with a machined hole), the fabricated meta-optic (Figure 6.2c), and a FLIR Boson thermal camera core with 12 μm/pixel resolution. For narrowband characterization, an optical filter (Thorlabs FB10000-500, IR bandpass filter with central wavelength 10.0 μm and FWHM 0.5 μm) was placed directly in front of the external aperture. For broadband characterization no filter was placed in front of the aperture and detection was limited to the response of the camera sensor (8 - 14 μm wavelength). In all imaging experiments, we adjusted the position of the imaging sensor to optimize the image quality.

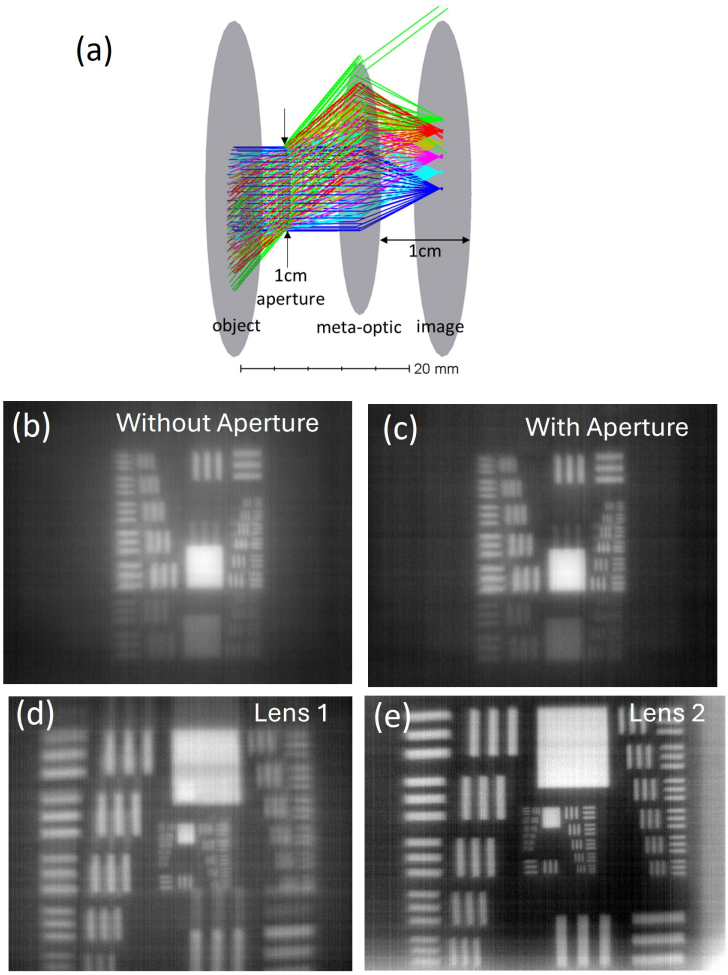

Figure 6.3: Initial measurements. (a) Ray tracing diagram, highlighting the utility of the aperture to control the rays. (b) and (c) compare Lens 1 measured without (b) and with (c) the aperture in place under unfiltered illumination. Without the aperture, there is additional noise due to uncontrolled light. The double image is due to striping issues in fabrication. (d) and (e) compare the performance of the two fabricated optics under filtered (10 μm) illumination. While Lens 1 and Lens 2 were of identical design and were fabricated on the same wafer, Lens 2 exhibited clearly better fabrication quality and, hence, better optical performance. In particular, the double images present in Lens 1 originate from striping artifacts in the fabrication.

Imaging results under narrowband illumination and 7.45 cm object distance, demonstrating the 80° FoV, and a comparison to simulations are summarized in Figure 6.5. In Figure 6.5a, ray tracing results (10 μm) for the optimized lens system are shown, based on an arrangement corresponding to the experimental setup. The experimental capture is shown in Figure 6.5b for comparison. Because the size of the large FoV image exceeded the size of the camera sensor, we translated the camera over the size of the image, collecting a 5x5 array of images which were stitched together into the final image; the 5x5 array of composite images is shown in Figure 6.4, and the composite result is shown in Figure 6.5b. In general, a qualitatively good agreement in resolution with simulation is achieved, and the image maintains acceptable quality throughout the entire FoV. In the experimental results, line features on the order of 350 μm can be resolved at the specific object distance, corresponding to angular resolution of 4.6 mrad. We note that, while the resolution is not diffraction-limited, this is qualitatively good enough for many LWIR imaging applications. The curvature of the image towards 40° is due to barrel distortion or the "fish-eye" effect, which is a correctable distortion that is due to mismatch between the displacement of the focal spot and the paraxial displacement at large FoV [4, 71, 72]. To further illustrate the aberrations present in the optical system, we show the aberration ray fan plot in Figure 6.5c. We plot the aberration with respect to the normalized pupil for both tangential (solid lines) and sagittal directions (dashed lines), which show similar aberrations over all angles of incidence.

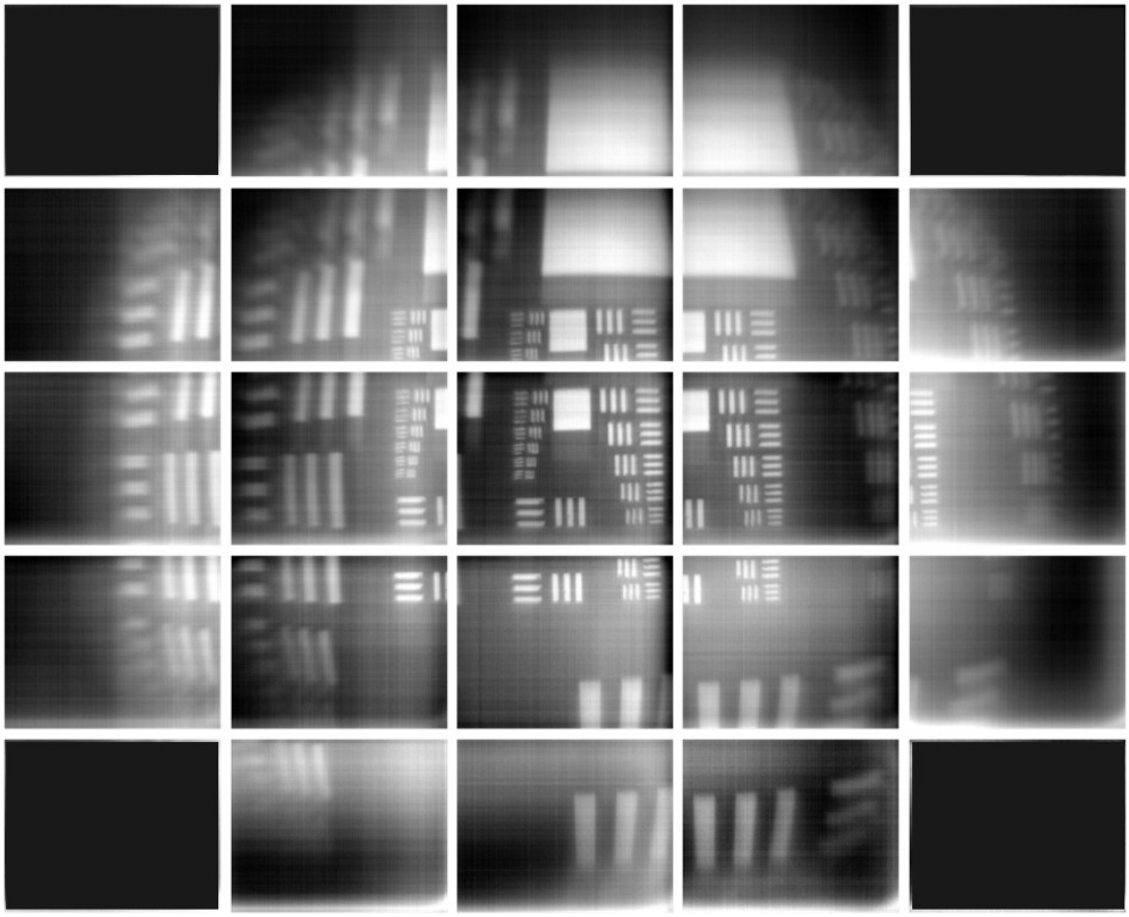

Figure 6.4: The 5×5 array of images that were combined into the composite result shown in Figure 6.5.

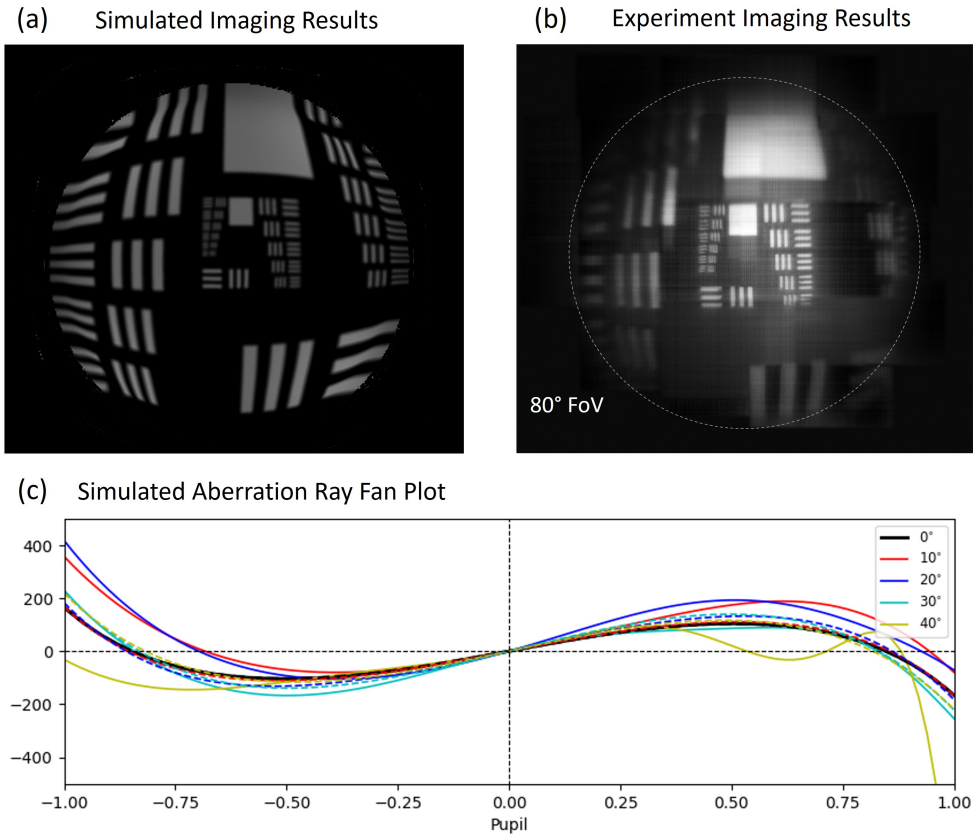

Figure 6.5: Large FoV imaging results. (a) Simulated results via ray tracing through the optimized lens system. (b) Experimental results demonstrating 80° FoV under narrowband illumination. (c) Simulated aberration ray fan plot, with the tangential aberrations plotted as solid lines and the sagittal aberrations plotted as dashed lines.

To further assess the meta-optic performance, we compared the same features across the entire field of view for the presented meta-optic system and a comparable singlet refractive lens (TECHSPEC Germanium Plano-Convex lens, 25 mm diameter and 25 mm focal length, uncoated). We placed the target at a distance of 30 cm from the imaging system and rotated the entire imaging system relative to the target in increments of 10° up to 40°. The results are shown in Figure 6.6a, for both the comparable refractive singlet and meta-optic system at 10 μm wavelength. At normal incidence, the refractive singlet produces crisper imaging

quality. However, as the angle of incidence increases beyond 20°, the performance of the meta-optic clearly exceeds that of the simple refractive lens.

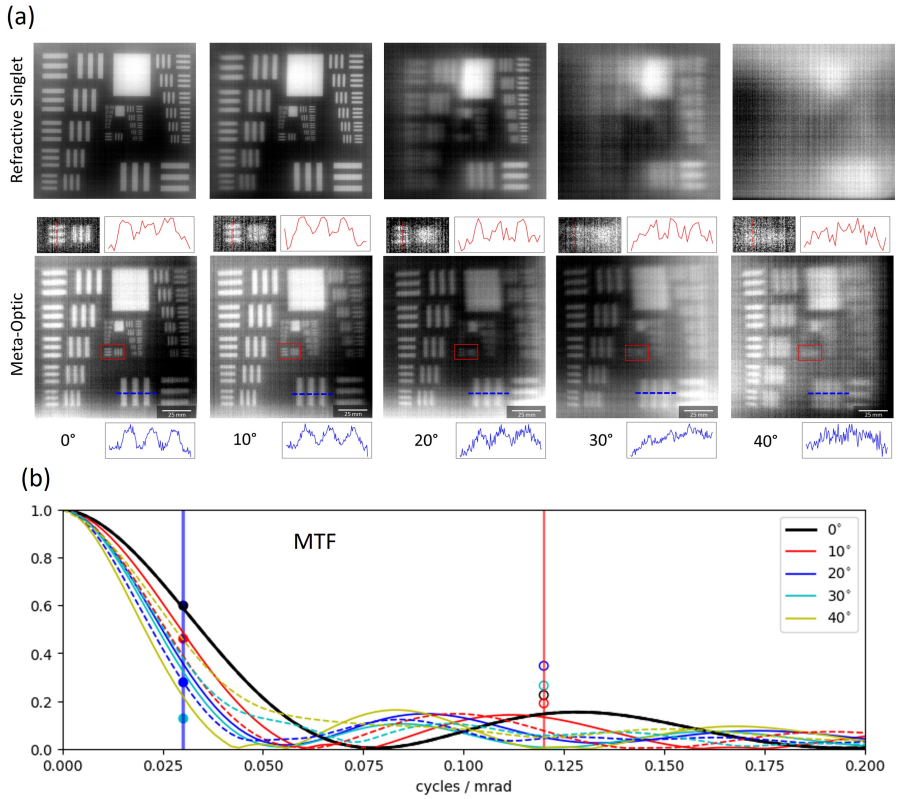

Figure 6.6: Imaging quality at angles of incidence up to 40° half-FoV. (a) Experimental results demonstrating the resolution of an image taken with a comparable refractive singlet (above) and the meta-optic system (below) at incident angles up to 40°. The insets show detail of the region denoted by the red square, with a vertical profile taken along the red dashed line and that profile plotted above. An additional profile is taken through larger line features in the lower right corner of the image and is plotted below. (b) Simulated MTF at incident angles up to 40° for both tangential (solid lines) and sagittal (dashed lines) directions. The vertical red and blue lines indicate the resolution of the groups highlighted by the insets from (a).

We note that the thermal light sources are too weak and the camera is too noisy to effectively measure the point spread function (PSF) or modulation transfer function (MTF) of the meta-optic. An LWIR laser source and cooled camera will be needed to measure them. Due to the lack of these in our experiment, we rely on directly imaging the USAF resolution chart to estimate the resolution and present these results along with the simulated MTF in 6.6b. The insets defined by the red boxes show line features with widths of 1.25 mm, corresponding to an angular resolution of 4.2 mrad per line, or equivalently, 0.12 cycles / mrad resolution. A cut is taken along the red dashed line in the meta-optic images and plotted above right for additional clarity. In experiment, we can easily resolve these groups for angles up to 20°, while for larger angles, especially at 40°, these groups are beyond what can be resolved clearly. We note that some variation in intensity across the images is apparent, which we attribute to expected changes in transmission over various angles of incidence due to the meta-atom scatterer response. In general, as shown in Figure 6.1d, the average transmission decreases for increased angle of incidence, and the transmission at 20° is particularly low, which is qualitatively consistent with the observed results. In the lower right side of the image, an additional line cut is taken along the blue dashed line through line features with widths of 5 mm corresponding to 0.03 cycles / mrad resolution.

To quantitatively corroborate the experimental results, we plot the simulated MTF of the imaging system in Figure 6.6b, at angles of incidence up to 40°, with solid lines denoting the tangential MTF and dashed lines denoting the sagittal MTF. Consistent with qualitative inspection of the experiment images, the simulated MTF is slightly higher at normal and small angles of incidence (0° and 10°) than it is for larger angles of incidence (20° and beyond). For quantitative comparison, the contrast values obtained from the experiment image line cuts, at 0.03 cycles / mrad and 0.12 cycles / mrad resolution and denoted by the blue and red lines, are plotted as circles for comparison. The chosen line features corresponding to 0.03 cycles / mrad resolution are vertically oriented, so their contrast values are comparable to the tangential MTF and are plotted as filled circles. The experimentally obtained contrast values closely match the simulated MTF at small angles of incidence (0° and 10°). At larger

angles of incidence, the measured contrast is less than the simulated contrast. At 0.12 cycles / mrad resolution, the chosen line features correspond to the sagittal MTF and are plotted as open circles, and in this case the measured contrast is higher than the simulated contrast.

Interestingly, the experimental results slightly outperform the simulated results in terms of resolution near normal incidence, both here in the sagittal MTF and in Figure 6.5 upon close inspection of the inner groups. We attribute this to the fact that the simulation assumed collimated input light, whereas the experimental illumination was not collimated, and that we manually adjusted the distances between the aperture, meta-optic, and camera (to within experimental uncertainty) to qualitatively optimize the image quality. To optimize for the human eye, we likely produced slightly better imaging at normal incidence at the expense of slightly worse imaging at larger angles of incidence as compared to the simulation, which aimed to simultaneously optimize for all angles of incidence. The estimated 4.2 mrad experimental resolution was determined from a cut near the center of the image, where we were best able to optimize our experimental conditions.

Finally, we characterized the imaging performance under conditions which exceed the nominal design constraints, namely broadband illumination (8 - 14 μm) rather than single-wavelength illumination for which the system was particularly designed. Although the system was optimized for a wavelength of 10 μm, operation over a broader spectral range may be indispensable or simply more practical in realistic applications. However, chromatic aberrations which reduce the image quality under broadband illumination are a challenge in meta-optics systems [73, 74, 30, 75]. Specifically, the focal length of a standard metalens is proportional to $1/\lambda$, which leads to focal spots at different points along the optical axis for different wavelengths [76]; this effect manifests as a haze in broadband images. To counteract this deterioration in the image quality, computational post processing steps have been shown to be useful [30, 77]. We demonstrate this capability for a moderate 30° FoV, which is the largest FoV attainable in a single image due to the limited size of our camera sensor. The results are summarized in Figure 6.7 for two test targets, a 2.5 times scaled USAF target and an artistic sketch of a husky; mobile camera images of the objects are shown in Figure

6.7a. First, we show the meta-optic images captured under broadband thermal illumination, without any computational postprocessing, in Figure 6.7b. Notably, a strong haze is apparent in the images, which reduces the image contrast for high resolution features. We then applied a computational postprocessing step on the raw images with a Gaussian sharpening filter and bm3d denoising algorithm [31], which reduced the haze and increased the contrast of the features, as apparent in Figure 6.7c. The image quality was significantly improved after these steps, and we achieve on-par imaging quality with the narrowband imaging at the design wavelength (Figure 6.7d). The inset Figure 6.7e shows the inner groups of the narrowband imaging result to demonstrate detail. The line plots above the USAF images show line cuts as denoted by the dashed red lines for additional clarity.

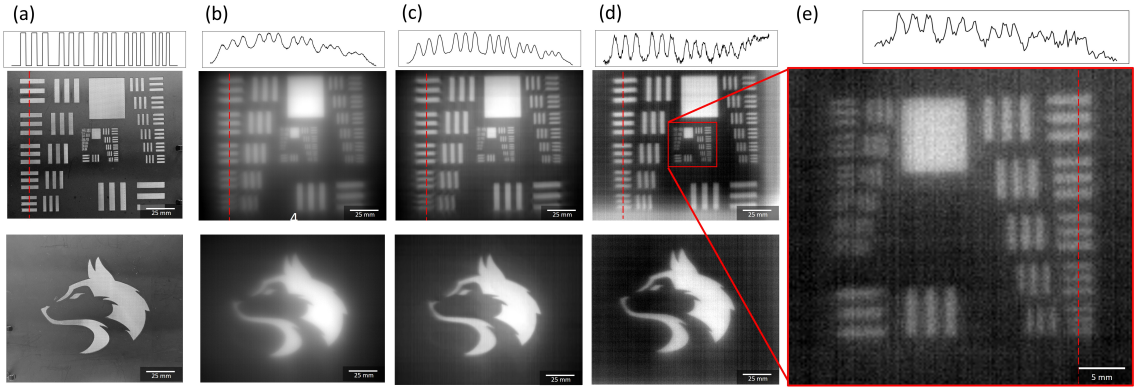

Figure 6.7: Broadband imaging and computational postprocessing. (a) Ground truth. (b) Meta-optic image under unfiltered, broadband ambient thermal illumination. (c) The images of (b) with an additional computational postprocessing step applied. (d) Capture with narrowband filter at 10 μm illumination, without any additional computational processing. The inset (e) shows the resolution of the inner groups of the imaging target.

6.1.4 Discussion

We demonstrated an all-silicon thermal meta-optic imaging system for 10 μm wavelength with 80° FoV. While the imaging resolution is not diffraction-limited, acceptable quality is

maintained over a large FoV and for relatively large entrance aperture of 1 cm ($\sim 1000\lambda$). In general, the achievable resolution of a single lens is either diffraction-limited, as in the case of a lens with large f-number and small diameter, or limited by geometric aberrations, in the case of a lens with large diameter [25, 78]. As the diameter increases, geometric aberrations become dominant because distance between rays and the optical axis increases. For an appropriately scaled system (keeping the f-number constant) based on the design in this paper, geometric aberrations become severe beyond 2 cm entrance aperture for normally incident light. However, wide FoV performance places additional constraints on lens designs, and as shown in other works [4] the constraint for diffraction-limited resolution must be relaxed to achieve a wide FoV. In an external aperture design like the one discussed in this paper, reducing the entrance aperture improves geometric aberrations for performance closer to the diffraction limit, although the diffraction-limited spot size has also increased due to the increase in f-number. Additionally, larger entrance aperture causes greater spatial overlap between light rays of different angles of incidence, and therefore the lens phase profile cannot be fully optimized for all angles simultaneously. As a result, the imaging resolution of a large FoV, large aperture lens is necessarily reduced from the diffraction limit for all incident angles. In the case of this lens, the geometric aberrations are comparable in severity over the entire FoV. Alternatively, foveated imaging, as recently demonstrated in LWIR [65], combines a narrow FoV but high-resolution lens and a large FoV, low-resolution lens to achieve high resolution at the center of an image, with low resolution over large FoV for context.

The imaging resolution could be improved by either reducing the entrance aperture or increasing the distance between the aperture and the optic to further spatially separate the incident angles. As the lens is currently designed, there are areas of the lens where the 10° and 40° incident light overlaps, and the lens cannot simultaneously be optimized for both. However, either decreasing the entrance aperture or increasing the aperture-lens distance would change the effective f-number of the system, resulting in fundamentally different characteristics. In addition, reducing the entrance aperture has the negative impact of lowering

the light throughput, and subsequently the signal-to-noise ratio. Since many LWIR applications involve imaging distant objects or low-light conditions and limited camera sensitivity, maintaining a large aperture benefits the overall image quality. Increasing the aperture-lens distance would increase the size of the system and require a larger meta-optic, both of which may be impractical for space-constrained systems. However, we still benefit from the light weight of the meta-optics over refractive lenses. Here, we aim to present a well-balanced design, which could be modified to fit specific applications as required by constraints on size, weight, resolution, and FoV. Additionally, we note that extension to even larger FoV is possible by increasing the size of the meta-optic relative to the external aperture to capture rays of larger incident angles.

The next challenge for this design would be to achieve broadband operation over the entire LWIR wavelength range (8 - 12 μm). While we demonstrate that some degree of broadband imaging is possible despite designing the lens for a single wavelength, a wide FoV lens with inherently broadband operation has not yet been shown in thermal meta-optics. However, recent works have demonstrated high-quality full-color imaging in the visible, which can be adapted for the LWIR regime as well [79].

In conclusion, we have designed and demonstrated a 1 cm aperture, 80° FoV lens system for LWIR imaging, specifically designed for 10 μm illumination. By direct measurement, we quantified the angular resolution to be better than 5 mrad, and demonstrated that this resolution degrades only slightly up to incident angles of 40°. When compared to a similar singlet refractive lens, the meta-optic system exhibits slightly worse performance at normal incidence but clearly superior performance at large angles of incidence. The light weight and compact nature of these meta-optics together with large FoV functionality can contribute significantly towards the development of highly integrated and lightweight LWIR imaging systems, for applications including night vision goggles, aerial surveillance, and thermal tomography.

6.2 Large Aperture Wide FoV Meta-optic Doublet Eyepiece

In this section, we extend our examination of doublets to a true doublet system consisting of two layers of meta-optics. While replacing the simple aperture with a second meta-optic increases the complexity of the design, it enables improved performance. This true doublet is similar to the pseudo-doublet of the previous section in that the majority of the lensing power is on the back element; however, in this case front element acts as a corrective plate in addition to an aperture. The contents of this chapter are adapted from [80]: *Anna Wirth-Singh, Johannes E. Fröch, Fan Yang, Louis Martin, Hualiang Zhang, Quentin T. Tanguy, Zhihao Zhou, Luocheng Huang, Demis D. John, Biljana Stamenic, Juejun Hu, Tian Gu, and Arka Majumdar. Wide Field of View Large Aperture Meta-Doublet Eyepiece. arXiv Preprint https://doi.org/10.48550/arXiv.2406.14725, June 2024*, with permission from the authors.

6.2.1 Introduction

Alongside advances in artificial intelligence and widespread availability of digital content, demand for augmented reality (AR) and virtual reality (VR) near-eye displays has surged. There is great commercial interest in developing such technologies for education, gaming, and social interactions, and also significant defense and national security interest for night vision and enhanced vision. However, achieving wide field of view in near-eye displays presents significant optical engineering challenges [81, 82]. In addition, near-eye optics must be thin and lightweight for user comfort and safety, especially for long-duration usage to reduce fatigue. With traditional optics, there is often a trade-off between compact form factor and performance, and the ultimate challenge of near-eye displays is that it demands both.

A comfortable reading distance is around 35 cm [83], which is much greater than the distance between a head-mounted near-eye display and the eye. Therefore, eyepiece optics are required to collimate near-eye illumination in order to project the image to a comfortable viewing distance. It is desirable to mount such optics near the head to minimize torque on the wearer and maintain a compact form factor; on the other hand, the minimum acceptable

physical distance between an optic and the surface of the eye (called eye relief) is about 1.5 cm. This provides a small amount of working space, thus requiring compact optics. Since meta-optics have demonstrated ability to achieve wide field of view in compact form-factor, they may be particularly suitable for near-eye display applications. In fact, several meta-optic systems have been proposed or demonstrated for AR/VR [84, 85, 86, 10, 87]. However, simultaneous achievement of large aperture and wide field of view is inherently challenging because monochromatic Seidel aberrations scale with aperture size and field angle [25]. In order to achieve diffraction-limited resolution over large field of view and relatively large aperture, it has been shown that doublet configurations are required [88]. In such a configuration, the first metasurface functions as both entrance aperture and a corrective plate, and the second functions a focusing lens.

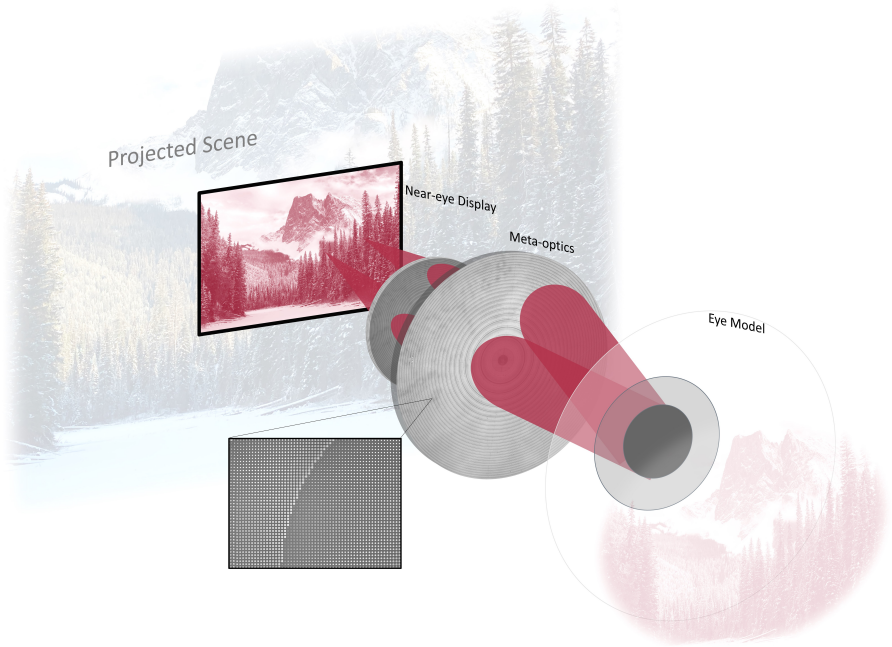

Figure 6.8: Eyepiece schematic. Illumination from the near-eye display is collimated via two meta-optics into the pupil of the eye. The inset illustrates that the metasurface is composed of arrays of nanoscale pillars.

In this work, we demonstrated high quality image projection over 60° field of view at 633 nm via a meta-optic doublet for eyepiece applications. The concept of the wide field of view eyepiece is schematically illustrated in Figure 6.8. The meta-optic is designed to collimate light from a near-eye display into the pupil with greater than 60° field of view. When the optics exhibit wide field of view functionality similar to that of the human eye, the user perceives a wide scene comfortably located at infinity, despite the display being physically located near the eye.

6.2.2 Design and Modeling

In detail, we took a step-by-step approach towards realizing large aperture (2 cm, $\approx 31500\lambda$) optics by first demonstrating the concept on a 1 cm aperture meta-optic doublet with 80° field of view. We then demonstrated the full-scale system with large aperture (2 cm) and 60° field of view.

The meta-optics were modeled using ray tracing software (Zemax OpticStudio), wherein the meta-optics were modeled as Binary-2 type surfaces in the same manner as the LWIR wide field of view optic described in Section 6.1. That is, the surfaces impart a phase delay given by the radially symmetric polynomial

$$\Phi(\rho) = \sum_{i=1}^{10} A_i (\frac{\rho}{M})^{2i} \tag{6.2}$$

where M is a normalization constant, ρ is the radial coordinate, and A_i are fitted polynomial coefficients. In this case, we defined input fields at incident angles from 0° to 40° in 5° increments and weighted them equally during optimization. In addition, the air gap between the optical windows was also allowed to vary during optimization. The optimized coefficients A_i for both 1 cm and 2 cm designs are provided in Table 6.1.

Ray tracing diagrams of the designed meta-optic doublet systems are shown in Figure 6.9. The 1 cm aperture design, shown in Fig. 6.9a, is demonstrated as a proof of concept prior to the full aperture (2 cm) design shown in Fig. 6.9b. In both cases, the system consists of a display (at the left), the two meta-optics (labeled MS1 and MS2) mounted on glass spacers

Table 6.1: Metasurface Phase Coefficients

	1 cm MS1	1 cm MS2	2 cm MS1	2 cm MS2
M	220	4.9499019	880	880
A_1	-39030668	-5396.6394	-2.5301487e+08	-5065492.6
A_2	-3.4998936e+09	-4605.9085	3.1181838e+10	3.617131e+11
A_3	1.1770126e+14	52695.076	-1.5514954e+15	-1.4121207e+16
A_4	-1.6476049e+18	-170751.14	3.9689123e+19	5.699969e+20
A_5	1.2079497e+22	165018.88	-6.00699e+23	-5.589307e+24
A_6	-5.2122204e+25	273878.4	5.5958326e+27	-1.4182956e+29
A_7	1.3689181e+29	-6511.3499	-3.211279e+31	3.0013409e+33
A_8	-2.1507485e+32	-2438339	1.0918782e+35	2.2855181e+36
A_9	1.8577437e+35	4093040.3	-1.9629298e+38	-3.7326393e+41
A_{10}	-6.7821622e+37	-2029151.3	1.3505338e+41	2.058759e+45

with a small air gap in between, and the pupil aperture. Since beams with wide field of view diverge quickly, the required size of MS1 to collect the diverging beams rapidly increases; to mitigate this, optical windows (fused silica (n = 1.46) in the 1 cm designs and BK7 glass (n = 1.52) in the 2 cm designs) are used to reduce the beam divergence. Similar to other metasurface doublet systems [76, 89], the entrance meta-optic (labeled MS2) functions as both an aperture stop and corrector plate, and the second meta-optic (labeled MS1) possesses the majority of the focusing power. We designed the system for 80 ° full field of view in the 1 cm system and 60 ° full field of view in the 2 cm system; in this case, the field of view is practically limited by the size of the second meta-optic due to fabrication constraints. From the ray tracing diagram, distortion is evident in the refractive system at wide field of view, whereas the designed meta-optic system exhibits very little distortion, even at incident angles of 30°. In Table 6.2, we summarize the key design specifications of the discussed systems,

including their effective focal length, numerical aperture, total track length, and eye relief. The effective focal length and numerical aperture were calculated from the Zemax model.

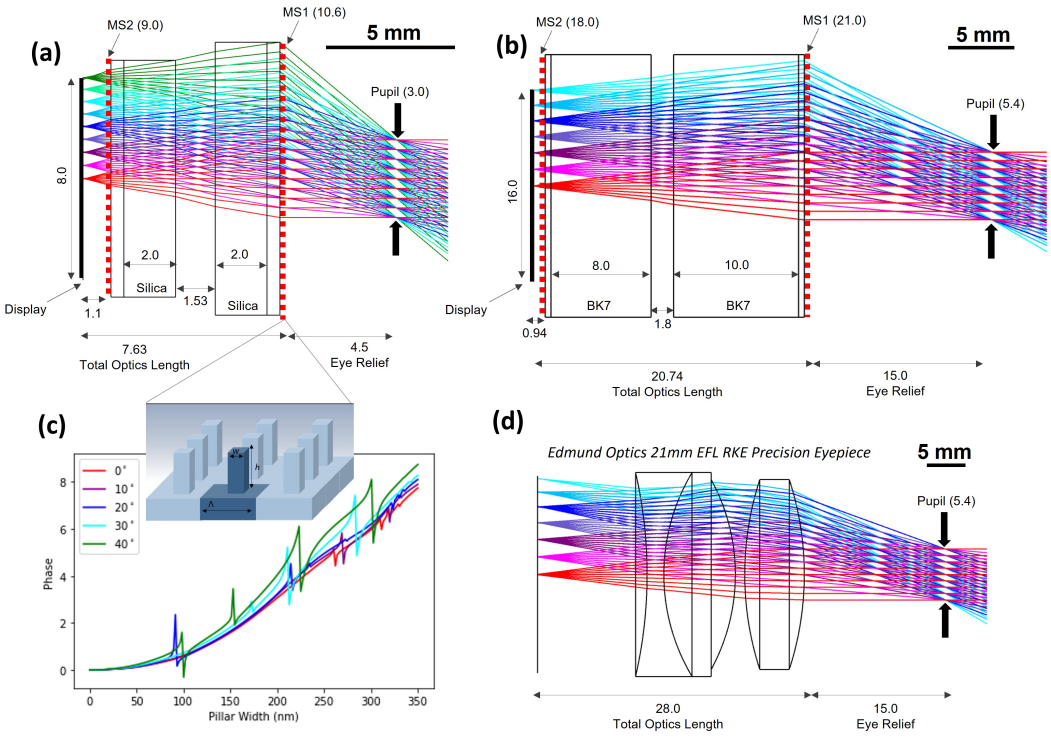

Figure 6.9: Eyepiece ray tracing diagrams. All units are in mm unless otherwise specified. (a) Ray tracing diagram for the 1 cm aperture meta-optic doublet eyepiece with 80° field of view. Rays are colored by field angle, with normally incident rays in red and rays at 40° incidence in green. (b) Ray tracing diagram for the 2 cm aperture meta-optic doublet eyepiece with 60° field of view. (c) Meta-atom design. The meta-optic consists of a periodic array (fixed periodicity Λ) of square pillars of uniform height h and variable width w. Meta-atom phase responses are calculated using rigorous coupled wave analysis for various angles of incidence. (d) Ray tracing diagram for a comparable commercial refractive eyepiece. Angles of incidence up to 60° are shown. The scale bar in (a), (b), and (d) is 5 mm.

To implement these phase profiles in a physical structure, we utilize the local phase

approximation to map between desired phase and pillar geometry as usual. In this case, the scatterers are 750 nm SiN square pillars on quartz substrate, arranged on a 350 nm periodicity lattice. Figure 6.10a and 6.10b show the simulated phase and transmission (using RCWA [70]) for the design wavelength of 633 nm. Because there is minimal variation in phase at increasing angle of incidence, we use the phase response at normal incidence to map from desired phase to pillar width. With the exception of some resonant behavior, the transmission is expected to be $> 70\%$ at all angles. In actual devices, the resonances are expected to be less prominent than predicted due to fabrication imperfections which reduce resonant quality. In Fig. 6.10c and 6.10d, we plot the desired phase profiles for both metasurfaces (MS1 in red and MS2 in blue) for both the 1 cm and 2 cm optics. MS1 performs the majority of the lensing function and is similar to a quadratic phase profile for large FoV [4]. The second metasurface acts as a corrector and entrance aperture and has a smaller phase gradient.

Table 6.2: Eyepiece Design Specifications

	1 cm Meta-Doublet	2 cm Meta-Doublet	Refractive Triplet
Entrance Aperture (mm)	10.6	21.0	20.0
Designed field of view (°)	80	60	45*
Pupil Diameter (mm)	3.0	5.4	5.4
Eye Relief (mm)	4.5	15.0	15.0
Effective Focal Length (mm)	5.84	15.17	21.61
Numerical Aperture	0.25	0.18	0.124
Total Track Length (mm)	12.1	35.7	43.0

* Reported apparent field of view

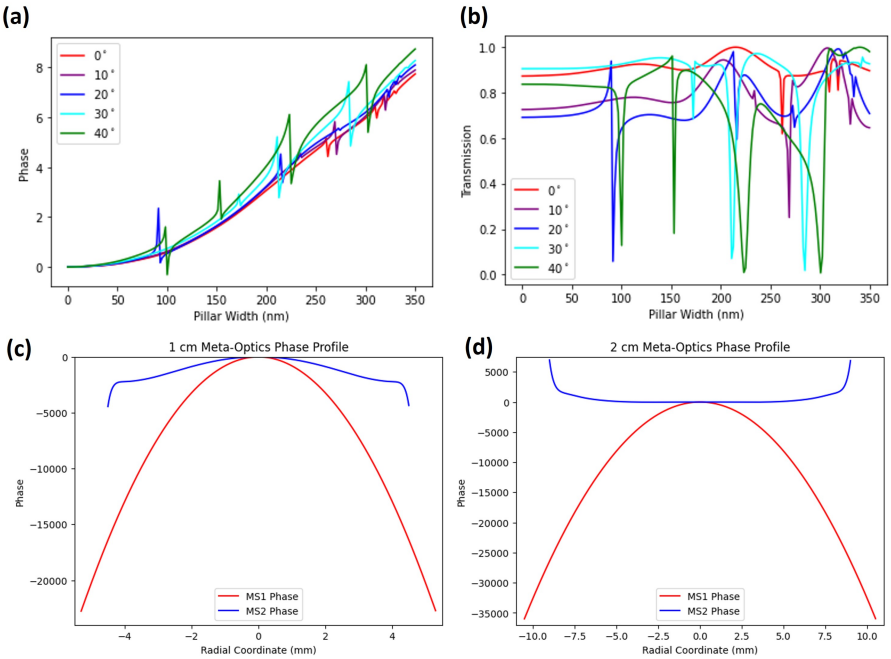

Figure 6.10: Scatterer simulations and phase profiles. (a) The simulated scatterer unit cell phase as a function of pillar width, for increasing angles of incidence. (b) The simulated scatterer unit cell transmission as a function of angle of incidence. (c) The desired phase profiles for the 1 cm meta-optics. (d) The desired phase profiles for the 2 cm meta-optics.

Due to sub-wavelength periodicity (350 nm) and large aperture (1 cm), the number of scatterers contained within each metasurface is large. Specifically, each of the 1 cm meta-optics contains on the order of 10^8 scatterers and each of the 2 cm meta-optics contains 10^9 scatterers at full aperture. Therefore, generating the GDS files for the meta-optics is a memory-consuming operation and a number of steps were taken to reduce computational burden. Firstly, the desired phase was discretized into 10 levels corresponding to 10 unique pillar geometries selected from the pillar width - phase response shown in Figure 6.10a. This discretization is expected to reduce the Strehl Ratio by only 4% [17] and allows for cell referencing which reduces the final GDS size. Secondly, the rotational symmetry of the optics were utilized. A radial slice of 1/8 of the full aperture was generated and then appropriately

rotated and copied at the last step of GDS generation to produce the full circular aperture. With these considerations, the file size of each 1 cm meta-optic is around 4 Gb.

6.2.3 Meta-Optics Fabrication and Characterization

The meta-optics were fabricated in silicon nitride on quartz using electron beam lithography and inductively coupled plasma (ICP) fluorine etching, with further details in Methods. Optical microscope and scanning electron microscope (SEM) images of the fabricated devices are shown in Figures 6.11a and 6.11b to highlight the fabrication quality. Some of the larger pillars are not fully separated due to resolution constraints. The silica and glass spacers were obtained from commercial sources (2 mm thick fused silica: Newport FSW14; 8 mm thick BK7 glass: Thorlabs WG11508; 10 mm thick BK7 glass: Newport 20BW40-30).

The fabricated optics, shown next to a ruler for scale, are shown in Figure 6.11c. The maximum aperture that we could fabricate using electron beam lithography was approximately 1 cm diameter, limited by the stability of the machine over extended write time. Therefore, the 2 cm eyepiece optics require a larger write area than realistically feasible using our methods. To circumvent this issue, we fabricated the entire aperture of the 1 cm meta-optics and only a slice of the 2 cm optics which was required to characterize the point spread function (PSF) of the optics. To measure the PSF, only the projected area of the pupil aperture (5.4 mm) is illuminated; therefore, the PSF characterization can be completed using only a slice of the metasurface with a dimension of 5.4 mm by 13.2 mm, covering the center to the outer edge. Therefore, we present PSF measurements of both the 1 cm and 2 cm optics and imaging results for the 1 cm optics only. In addition to electron beam lithography, we further describe fabrication of the full aperture 2 cm optics using deep ultraviolet (DUV) lithography; these optics are pictured at the bottom of Figure 3c. While DUV lithography is a more scalable lithography process, the resolution of our process was limited to $\approx$ 250 nm which is insufficient for sub-wavelength periodicity. The pictured full aperture 2 cm meta-optics are functional up to approximately 40° full field of view, limited by aliasing issues arising from large periodicity (see Section 6.2.4).

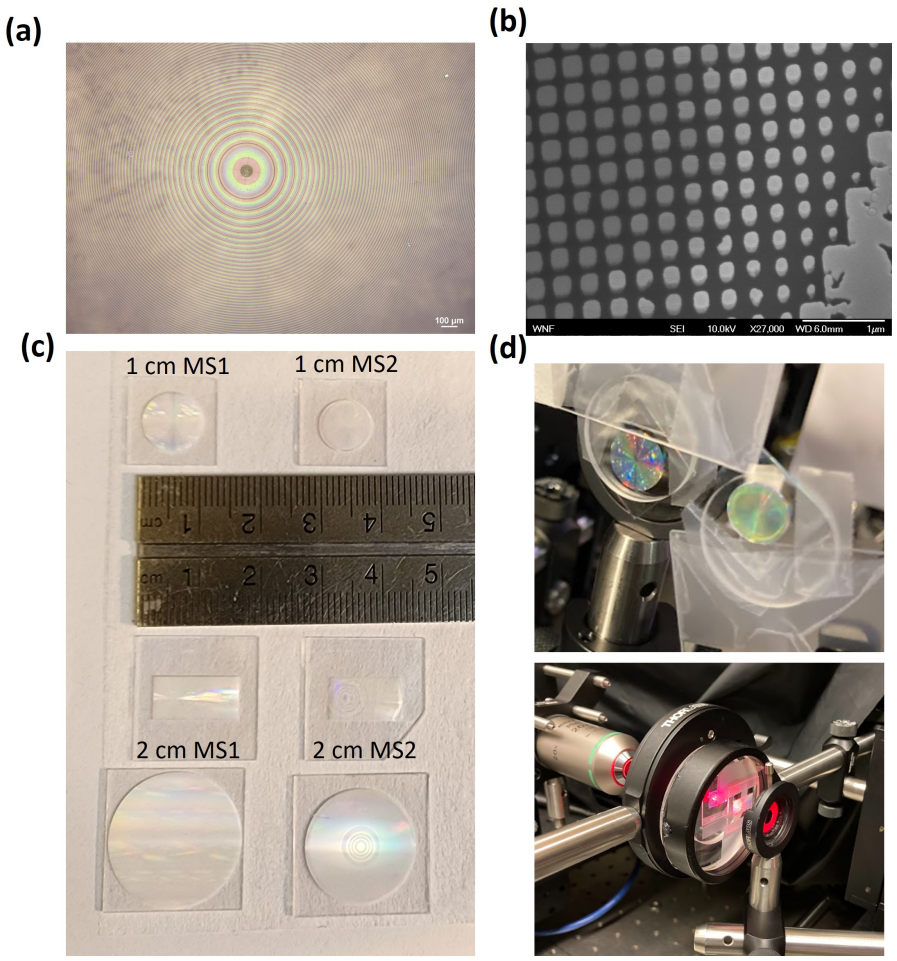

Figure 6.11: Fabricated meta-optics. (a) Optical microscope image of the fabricated meta-optics. (b) SEM image of the fabricated optics at slightly oblique (10°) viewing angle. (c) A photo of all fabricated meta-optics next to a ruler for scale. From top to bottom: the 1 cm aperture meta-optics, the 5.4 mm wide slices of the 2 cm meta-optics, and the full 2 cm aperture meta-optics fabricated using lower resolution scatterers. (d) A photograph of the 1 cm meta-optics (top) and 2 cm meta-optics (bottom) mounted on spacers in the experiment setup.

Detailed schematics of the experiment setup are shown in Figure 6.12. PSF measurements were done with the setup pictured in Fig. 6.12a and schematically depicted in 6.12b. The

illumination source was a HeNe laser (Newport N-LHP-131) at 632.8 nm wavelength with 1400 MHz linewidth (FWHM). The laser output was coupled to a single-mode fiber with approximately 300 nm diameter fiber core. A refractive lens was used to collimate the output. For measurements at various angles of incidence, the fiber output and collimator unit were mounted on a rotating arm to provide smooth rotation up to 40°. An iris placed at the axis of rotation served as the pupil aperture. Each meta-optic was mounted on 3-axis translation stage for precise alignment. The focal spot was magnified via microscope objective (Nikon Plan Fluorite 20x, NA = 0.50, WD = 2.1 mm) followed by a tube lens. The output was measured on a GT1930C camera sensor with 5.86 μm per pixel resolution. The effective pixel resolution given the relay optics was calibrated by imaging an object of known size with the relay system.

While the relay optics including the microscope objective are primarily used for magnifying the PSF, they have the additional function of aiding in the alignment of the meta-optic doublet system. By focusing the microscope objective on the surface of the meta-optic, the meta-optic surface can be precisely positioned. To successfully align the meta-optic doublet system, we first focused the microscope objective onto the surface of the iris. Using the motorized stage, we then moved the microscope objective backwards according to the designed spacing between the iris (pupil) and MS1. By then placing MS1 such that it is centered and focused in the microscope objective FoV, the metasurface has been correctly positioned. Repeating this procedure, we moved the microscope objective backwards according to the spacing between MS1 and MS2 and then place MS2 such that it is centered and in focus. Finally, by moving the camera stage backwards the desired focal plane, we are ready to measure the PSF of the aligned system.

The simulated and measured PSFs are summarized in Figure 6.13. In both the 1 cm and 2 cm aperture designs, the PSF (Figure 6.13a and 6.13b, respectively) remains mostly undistorted as the angle of incidence is increased. A horizontal line cut through each PSF is shown below, in Fig 6.13c and 6.13d, with the simulated PSF overlain in dashed black line, showing excellent agreement with the theory. For both the 1 cm and 2 cm systems,

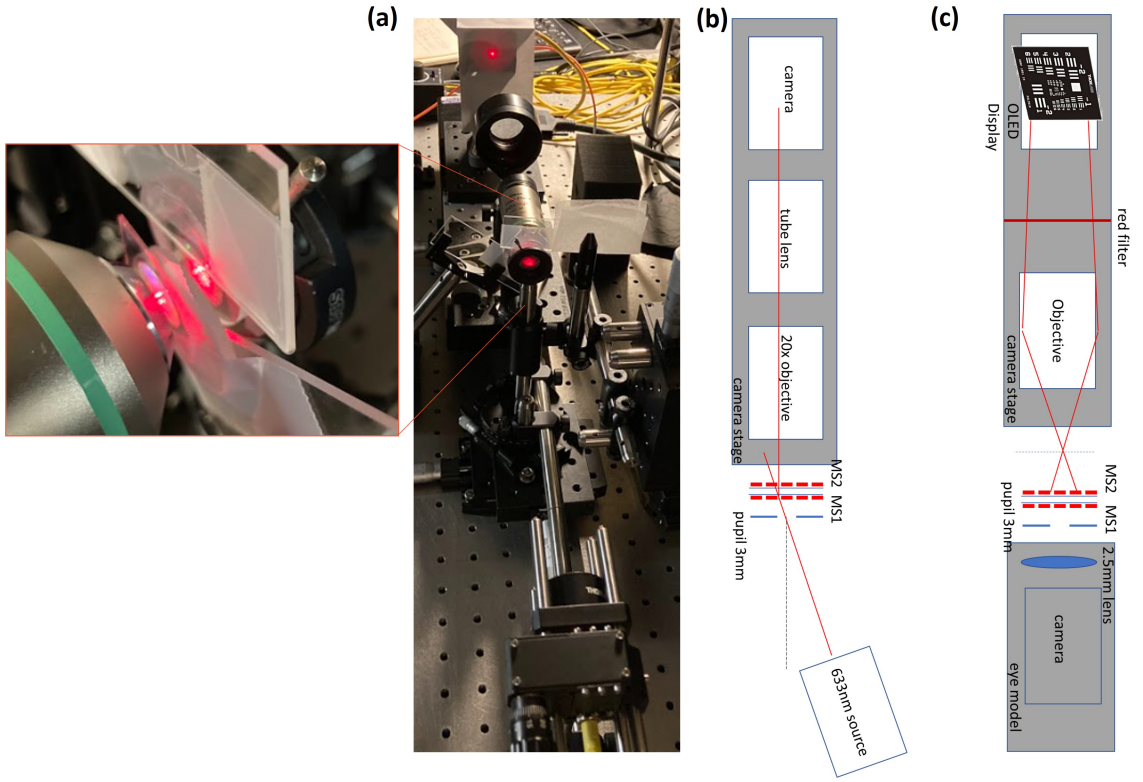

Figure 6.12: Meta-optics characterization setup. (a) Photograph of the PSF measurement setup, with the inset (left) showing the mounted meta-optics and collecting objective. (b) Schematic of the PSF measurement setup. (c) Schematic of the imaging setup.

the PSF is normalized to the maximum measured intensity of that system. Some reduction in PSF intensity at larger angle of incidence is expected and observed, with the measured PSF intensity at 20 degrees off axis being 82% and 64% of that at normal incidence for the 1 cm and 2 cm designs, respectively. However, the PSF width remains mostly undistorted, highlighting the utility of the lens system over wide field of view. In addition, the measured transmission through the optics is consistent with that predicted by RCWA. At normal incidence, the measured transmission through the 1 cm optics were measured to be 70% through MS1 alone, 83% through MS2 alone, and 63% through the system of both optics.

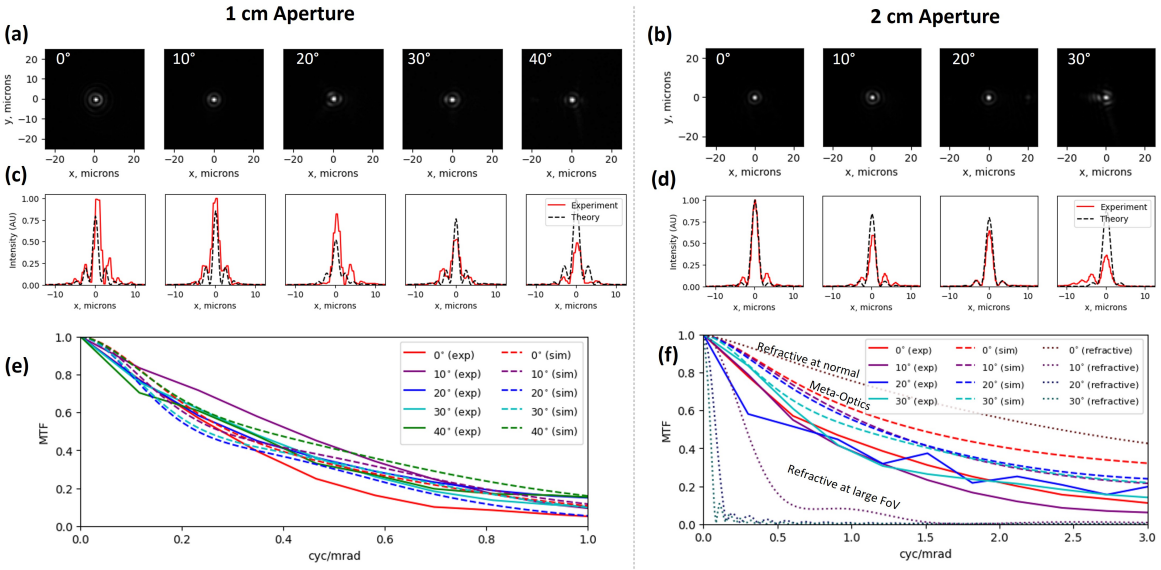

Figure 6.13: Lens point spread function measurements. (a,b) Measured PSFs of (a) the 1 cm aperture optics from 0° to 40° degree angle of incidence, and (b) the 2 cm aperture optics from 0° to 30° degree angle of incidence. (c,d) Line cuts from the PSFs in (a) and (b) comparing the experimental results (solid red lines) to the theoretical results from the ray tracing model (dashed black lines). The camera exposure time was kept constant in each case. The simulated and experimental PSF results were normalized with respect to the maximum intensity value in the set. (e,f) The experimentally measured (solid lines) and simulated (dashed lines) MTF for (e) 1 cm meta-optics and (f) 2 cm meta-optics at increasing angles of incidence. In (f), the MTF of the comparable commercial refractive eyepiece is plotted as dotted lines.

As another measure of optical performance, the modulation transfer function (MTF) describes the image contrast as a function of frequency. For an eyepiece optic with the function of projecting a displayed image to infinity, it is more appropriate to characterize the performance in terms of angular resolution (in cycles/mrad) rather than spatial resolution. From the measured point spread functions, we calculate the MTF at various angles of incidence in Figures 6.13e and 6.13f. The experiment results (solid lines) show consistent performance

over the entire field of view and good agreement with the simulated MTF (dashed lines). While the spatial resolution is similar for the 1 cm and 2 cm optics, the angular resolution of the 2 cm optics is much higher due to its longer effective focal length. For comparison, we plot the simulated MTF of the exemplary commercial refractive system (the same system depicted in Figure 6.9d) as darker dotted lines in Figure 6.13f. While the refractive system has higher MTF at normal incidence, it drops rapidly at increasing angles of incidence, showing a true FoV of less than 20 degrees. This is in contrast to the designed meta-optics, which exhibit similar performance across the entire field of view.

In general, the meta-optics experiment results exhibit excellent agreement with the ray tracing simulation. Upon close inspection, it is noted that under some conditions (namely 10° through 30° in the 1 cm optics) the experiment appears to slightly outperform the simulation. However, it should also be noted that the experimental performance is worse than the simulation at normal incidence. Therefore, we attribute the unexpectedly higher experimental performance to be due to slight misalignment which favors slightly off-axis angles. In the case of the 2 cm optics, the simulated results are consistently better than the experiment.

In Figure 6.14, we demonstrate the imaging quality of the 1 cm optics at wide field of view. We displayed the imaging pattern on a micro-LED display and re-imaged the pattern using a high NA objective (Nikon Plan Fluorite 20x) followed by a 633 nm narrowband filter (Thorlabs FLH632.8-1, FWHM 1 nm). After passing through the objective, the size of the imaging object was approximately 3 mm wide. The displayed pattern was a checkerboard in Figure 6.14(a) and a USAF resolution chart in Figure 6.14(b). To assess performance across a wide field of view, the imaging object was rotated relative to the imaging system at the specified angle of incidence. In the insets in Figure 6.14(c), we show exemplary line cuts through the red (left) and cyan (right) dashed lines to illustrate image contrast. Due to the slightly broad linewidth of the illumination source (FWHM 1 nm), the resolution is negatively affected by chromatic aberrations. In particular, off-axis performance is negatively affected by chromatic aberrations as the meta-optic phase gradient disperses illumination of

different wavelengths. To elucidate this effect, we plot simulated polychromatic PSFs in the insets to Fig. 6.14(a). These PSFs were simulated for 20 wavelengths between 630.5 nm and 635.0 nm, appropriately weighted to match the transmission spectrum of the narrowband filter. Lateral distortion of the PSF is apparent and worsens at increasing angle of incidence. Nonetheless, we demonstrate high-quality imaging up to 30° angle of incidence corresponding to 60° full field of view.

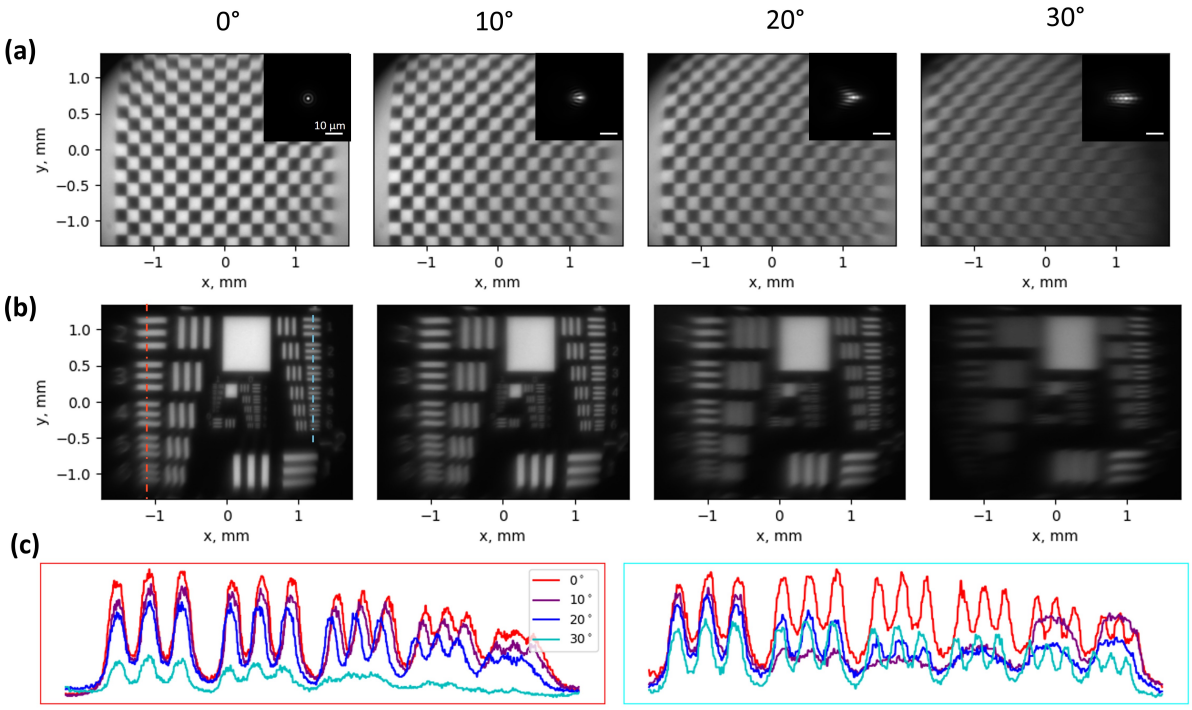

Figure 6.14: Imaging results for the 1 cm aperture optics. (a) A checkerboard pattern was displayed on a micro-LED screen and imaged at angles from 0° to 30°. The width of the re-imaged pattern is 3 cm. In the insets, we show the simulated PSF under for 632.8 nm illumination with 1 nm FWHM bandwidth. (b) The USAF resolution chart pattern was displayed on the micro-LED screen. The dashed red and cyan lines indicate where exemplary line cuts were taken. (c) Exemplary line cuts for each angle of incidence, illustrating the image contrast.

6.2.4 Full Aperture 2 cm Optics at Low Resolution with DUV Lithography

Electron beam lithography is one of the highest resolution nanofabrication techniques, capable of writing features only a few tens of nanometers in diameter. However, the technique is expensive and difficult to scale, making it unsuitable for commercial applications. To progress towards the goal of realizing large aperture meta-optics with commercially viable fabrication techniques, we designed and fabricated a full-aperture version of the 2 cm eyepiece doublet compatible with mass production-friendly deep ultraviolet (DUV) stepper lithography. While DUV is a rapidly improving technology, at present it cannot provide the same resolution as electron beam lithography.

The minimum feature size of our DUV lithography process is around 250 nm. Therefore, we adjusted the meta-optic unit cell to be compatible with the resolution limitations of DUV. For SiN-based visible meta-optics, the desired lattice periodicity is around $\lambda/2$ [90]; for the meta-optics presented in the main results, we use $\Lambda = 350$ nm, which requires a minimum feature (smallest pillar or gap) size around 80 nm to fully cover 0 to 2π phase range. For DUV lithography capable of producing 250 nm features, we identified a suitable set of scatterers with lattice periodicity of 1100 nm and pillar widths ranging from 300 nm to 600 nm. In addition, we increased the pillar height to 1750 nm to achieve the required 0 to 2π phase diversity. The phase and transmission responses of the 350 nm period and 1100 nm period scatterers are shown in Figure 6.16a and 6.16d, respectively. Due to the large periodicity relative to the wavelength in the 1100 nm case, the phase is not as well controlled. This results in an irregular phase response and reduced transmission as compared to the 350 nm case.

The DUV fabrication described herein was developed and carried out at the UCSB Nanofabrication Facility using an ASML 5500 DUV Stepper at 248 nm wavelength. The maximum die size was 21 mm by 21 mm square. In this process, a chrome-on-glass mask is made at 4x magnification. In the stepper, DUV light is flooded through the mask and focused onto the sample. The mask is then "stepped" over the surface of the wafer, in relatively

quick exposures, to rapidly produce copies of the desired optic. With the initial investment of a high-quality mask, the subsequent copies can be made quickly and at a relatively low cost. In addition, to provide better etching uniformity over a larger area, we chose sapphire (n = 1.77) substrate due to its better thermal conductivity as compared to quartz for this large-aperture fabrication.

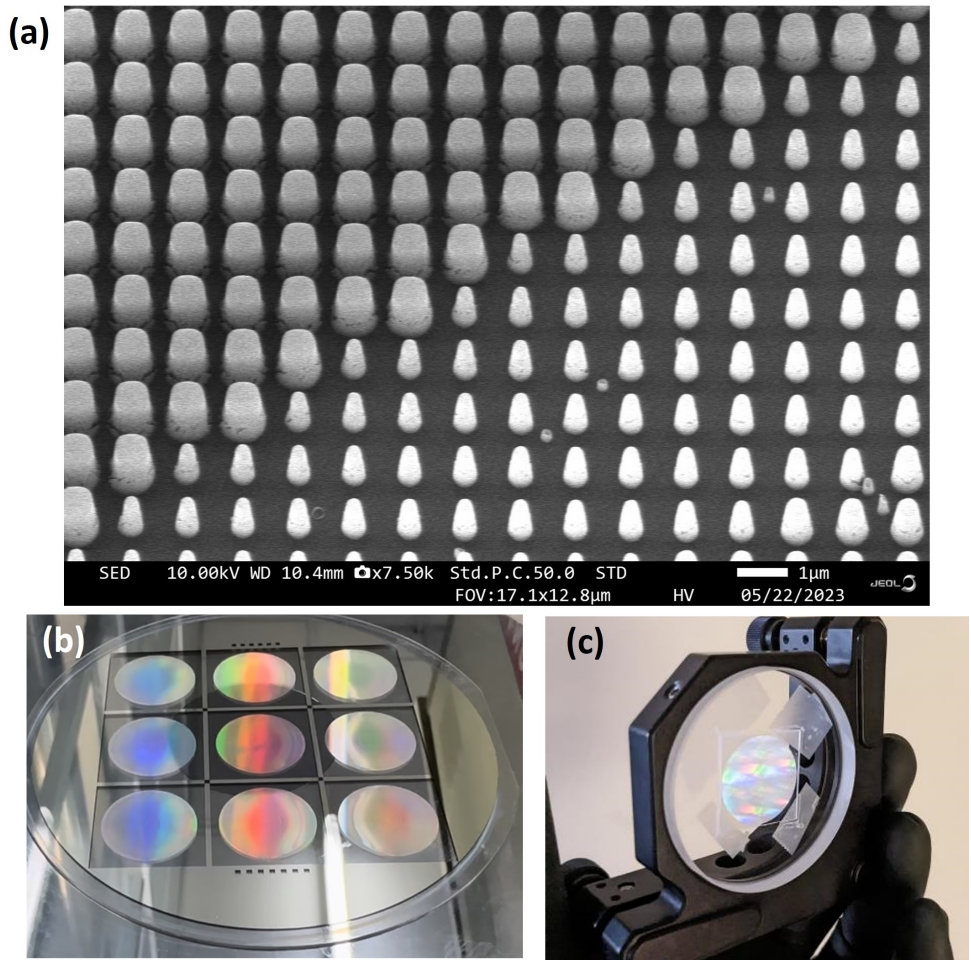

Figure 6.15: Full 2 cm aperture meta-optics fabricated with DUV stepper lithography. (a) Scanning electron microscope image of the fabricated optics. (b) A wafer containing several fabricated meta-optics prior to dicing. (c) The 2 cm diameter MS2 mounted on BK7 spacer in a 2" mirror mount.

In detail, the sapphire substrates (650 μm thickness) were obtained from a commercial source and we deposited 1.75 μm SiN via PECVD at a temperature of 350C. Following this, a layer of Ruthenium (Ru) and silicon dioxide (SiO2) were deposited as a hard mask according to an established process [91]. Lithography was performed using an ASML 5500 DUV Stepper with photomasks from Digidat, Inc. The SiO2 and Ru were subsequently etched to complete the hard mask. Next, the SiN was etched to the desired 1750 nm thickness. Finally, the SiO2 and Ru hardmasks were removed via dry etch. The fabricated wafers were diced to separate the individual meta-optics.

An additional negative consequence of the larger lattice periodicity is provides insufficient phase sampling to support the large phase gradient required of large FoV metasurfaces without introducing aliasing issues. While this does introduce undesirable effects, the meta-optics are still functional over a modest 40° full FoV. These issues and results are discussed below.

Wide FoV meta-optics require a large phase gradient in order to modulate light at steep incident angles. An additional limitation on attainable FoV arises from the maximum phase gradient which can be supported by the meta-optics for a given lattice periodicity. If the required phase difference between adjacent meta-atoms becomes greater than π, aliasing effects occur. To avoid aliasing, the phase sampling of the meta-optic must satisfy the Nyquist-Shannon sampling theorem:

$$\Lambda < \frac{\pi}{|\Delta\phi(x,y)|_{max}} \tag{6.3}$$

where Λ is the sampling periodicity and $|\Delta\phi(x,y)|_{max}$ is the maximum absolute difference between adjacently sampled points in the spatial phase profile $\phi(x,y)$ [92]. To relate this to geometric optics, the generalized Snell's Law relates the phase gradient along the surface to the deflection angle:

$$n_1 sin(\theta_1) - n_0 sin(\theta_0) = \frac{\lambda}{2\pi}\frac{d\phi}{dx} \tag{6.4}$$

where n_1 and n_0 are the refractive indices of the input and output medium (in this case, for air, $n_1 = n_0 = 1$), θ_1 and θ_0 are the input and output deflection angles, λ is the incident

wavelength, and $\frac{d\phi}{dx}$ is the phase gradient. From these two expressions, we can determine the maximum deflection angle of a metasurface for a given lattice periodicity:

$$\theta_{max} = sin^{-1}(\frac{\lambda}{2\Lambda}) \tag{6.5}$$

Equivalently, with numerical aperture (NA) defined as the sine of the maximum angle θ_{max} which can enter the optical system, we can directly relate the attainable NA to the wavelength and lattice periodicity:

$$NA \leq \frac{\lambda}{2\Lambda} \tag{6.6}$$

For lattice periodicity Λ which is smaller than half the wavelength ($\frac{\lambda}{2}$), angles up to nearly 90° can be supported. The maximum deflection angle supported by $\Lambda = 350$ nm is 65° (130° full FoV) for a single meta-optic. For the 1100 nm periodicity meta-optics, the maximum aliasing-free deflection angle is about 17° per optic. However, in a doublet system such as this one, this limitation can be mitigated by utilizing the additional degrees of freedom provided by the second surface. By stacking multiple metasurfaces, the overall deflection angle can be increased.

In Figure 6.16, we plot the desired and effective phase profiles for each 2 cm meta-optic for the high-resolution ($\Lambda = 350$ nm) and low-resolution ($\Lambda = 1100$ nm) scatterers. The desired continuous phase profiles for MS1 and MS2 are shown in black, the sampled phase profile modulo 2π is shown in red, and the effective phase profile given the phase sampling Λ is shown as a red dashed line. MS1, which accomplishes most of the lensing, has a phase gradient which increases approximately quadratically with the radial coordinate. The high-resolution scatterer periodicity provides sufficiently high phase sampling over the entire optic, so the effective phase gradient matches the desired phase gradient as shown in Fig. 6.16b. In MS2, the rapid increase in phase at the very edge is due to defining the optic diameter slightly larger than necessary; no rays interact with the outer edge, and as such the phase here is inconsequential to the performance of the system. For both MS1 and MS2, the lattice periodicity of 350 nm is sufficient to avoid any aliasing effects.

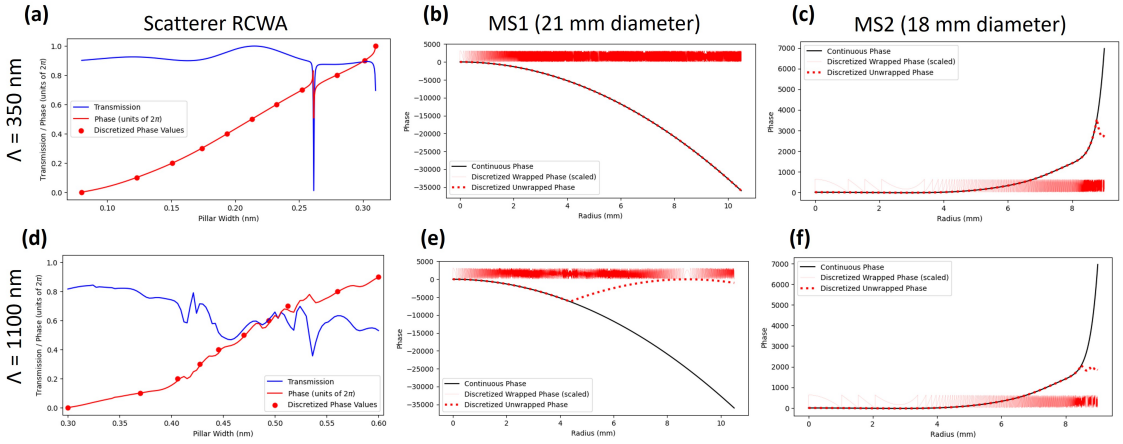

Figure 6.16: High-resolution and low-resolution scatterer simulations and phase profiles. (a) The simulated high-resolution ($\Lambda = 350$ nm) scatterer unit cell phase and transmission versus pillar width. The SiN pillars are 750 nm tall. The dots indicate the discretized pillar values used in fabrication. (b) and (c) The desired (solid black line) and effective (dashed red line) phase profiles for the 2 cm meta-optics MS1 and MS2, respectively, using $\Lambda = 350$ nm. Since the periodicity is sufficiently small to support the desired phase gradient, the effective phase is the same as the desired phase. (d) The simulated low-resolution ($\Lambda = 1100$ nm) scatterer unit cell phase and transmission versus pillar width. The SiN pillars are 1750 nm tall. (e) and (f) The desired and effective phase profiles using $\Lambda = 1100$ nm. Aliasing effects are observed when the phase gradient becomes too large for the periodicity to support, indicated by the divergence of the desired phase profile (solid black line) and effective phase profile (dashed red line).

In contrast, the aliasing effect is significant in MS1 when sampling with 1100 nm lattice periodicity. In Figure 6.16(e), these effects are observed where the effective phase profile (red dashed line) diverges from the desired phase profile. Specifically, around $\rho = 4.2$mm, the desired phase difference between adjacently sampled points becomes greater than π. Near $\rho = 8.0$mm, the phase difference becomes 2π, resulting in an effective phase profile which is significantly different from the desired phase profile. Experimentally, this generates

additional unwanted focal spots.

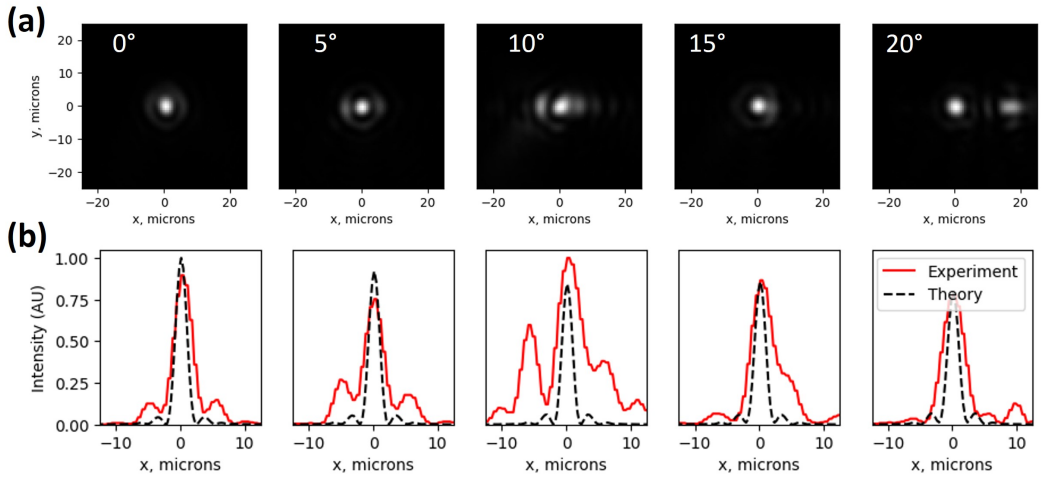

Figure 6.17: PSF measurements of the full 2 cm aperture meta-optics fabricated using DUV lithography. (a) Experimental PSF measurements from 0° to 20° angle of incidence. (b) Horizontal line cuts of the PSFs shown in (a), with the experiment results shown as solid red lines and simulated results as dashed black lines. The simulated and experimental PSFs were normalized to their respective maximum intensity values.

Using the same experimental setup as for the other optics, we measured the PSF of the low-resolution 2 cm meta-optics up to an incident angle of 20° corresponding to 40° full FoV. These results are summarized in Figure 6.17. As expected, the performance is a bit worse than for the 2 cm meta-optic slice fabricated with electron beam lithography, but the PSFs are still relatively high-quality.

6.2.5 Discussion

The specifications of 80° field of view for the 1 cm optics and 60° field of view for the 2 cm optics were chosen considering the tradeoffs between form-factor, aperture size, and field of view. In this work, the primary limitation on field of view is the maximum diameter

of meta-optics which can be reasonably fabricated. By increasing the diameter of MS1, the meta-optic can capture light at larger angles of incidence, which would increase the attainable field of view. As shown in several works, meta-optics achieving nearly 180° field of view have been demonstrated, but only for small entrance aperture [4, 63]. In fact, it has been shown that in order to simultaneously achieve large aperture and diffraction-limited performance over wide field of view, it is necessary to increase the thickness of the optical system [93, 94, 88]. Intuitively, this occurs because light of different angles of incidence must be spatially separated, which is easily achieved using a small entrance aperture to restrict light of different angles to interacting with different sections of the lens. In the case of large aperture, greater distance between the aperture and the lens is required to provide sufficient separation between the beams of different angles of incidence.

We note that the presented meta-optic doublet is designed for single-wavelength illumination at 633 nm, suitable primarily for monochromatic applications such as night vision. While much progress has been made in recent years to develop meta-optics with broadband operation in the visible regime [20, 21, 19], simultaneous achievement of broadband operation and wide field of view has yet to be demonstrated. For single-layer meta-optics, there are fundamental tradeoffs between device thickness, NA, and bandwidth [28].

In conclusion, we demonstrated a large aperture, wide field of view meta-optic doublet eyepiece for near-eye display applications. Our design considers realistic constraints such as eye relief, pupil size, and display size. In incremental steps towards a large aperture meta-optic eyepiece, we designed a smaller system with 1 cm entrance aperture as a proof of concept as well as a full-scale 2 cm entrance aperture system. In both cases, the experimental performance of the system closely agrees with the design and exhibits consistent performance over at least 60° full field of view. These findings represent promising results for the integration of meta-optics into full-scale near-eye display systems, including AR/VR and night vision.

6.3 Beam Aggregator

Meta-optics have numerous applications beyond imaging. In this section, I present our work on using meta-optics as a beam aggregator for a spatial light modulator (SLM). These meta-optics are featured in [95]: *Rui Chen, Virat Tara, Anna Wirth-Singh, Abhi Saxena, Johannes E. Fröch, Matthew S. Reynolds, and Arka Majumdar. A hybrid solution for spatial light modulators with a large space-bandwidth product: opinion. Optical Materials Express* ***13****, 8, https://doi.org/10.1364/OME.500078, July 2023*, with permission from the authors.

6.3.1 The Beam Aggregator Concept

A spatial light modulator (SLM) is a reconfigurable device that imprints an amplitude or phase (or both) modulation to control light. Similar to a meta-optic, the spatial light modulator consists of pixels that locally adjust the phase or transmission. In contrast to meta-optics, SLMs have an active modulation mechanism such as a digital micromirror device [96] or thermo-optic phase shifters [97]. A digital micromirror device acts on free-space light, while a thermo- or electro-optic phase shifter is directly integrated into a photonic integrated circuit (PIC) and then coupled to free space using grating couplers. The trade-off for tunability, however, is pixel pitch. Even in the most compact, state-of-the-art SLMs, the modulation pixel size is several times the order of the wavelength (on the order of 10 μm pixel pitch for operating wavelength of 1550 nm). This places limitations on an SLM's beamforming performance and its power consumption.

Meta-optics have sub-wavelength pixel pitch, but pixel-by-pixel tunable meta-optics have not been realized. So far, researchers have succeeded only in developing meta-optics with global tuning via stretchable substrates [98], electrical tuning [99], or phase change material [100].

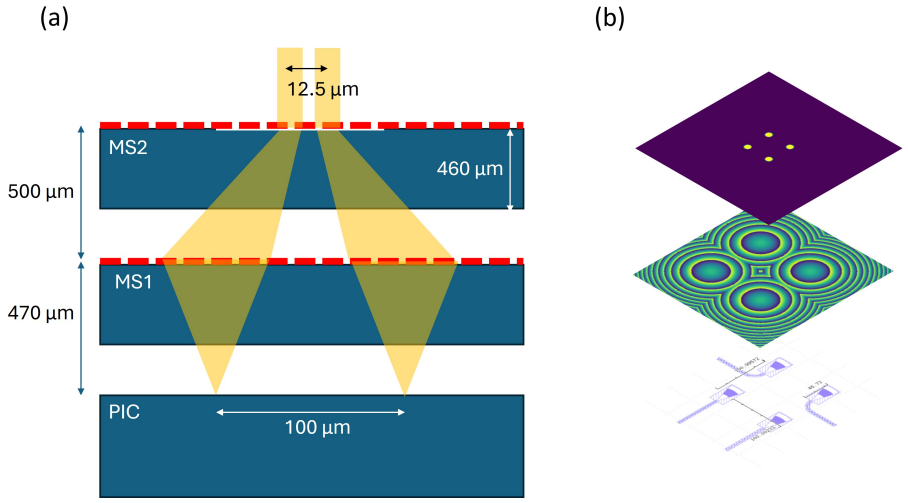

Figure 6.18: The beam aggregator schematic. (a) Side view of hybrid device. Light originating from the PIC (at the bottom) is coupled to free space via grating couplers. After passing through MS1, the light is lensed and steered towards the center. MS2 consists of an aperture array so that the light diffracts upwards into free space. (b) Schematic at each layer. The bottom shows the grating couplers, which are spaced 100 μm apart. The middle shows MS1, which is a meta-optic consisting of a lensing phase and a steering phase. MS2 at the top is an aperture array, with 12.5μm spacing between each aperture.

To resolve these issues, in this work we proposed and demonstrated a hybrid SLM wherein the tuning mechanism is accomplished in a PIC and then meta-optics are used to aggregate the beams, thereby decoupling the modulation mechanism from the spatial constraints. The meta-optics are used to aggregate the beams, thereby decreasing the pixel pitch and increasing the fill factor. This concept is schematically illustrated in Figure 6.18. Light from a PIC is coupled to free-space via grating couplers spaced 100 μm apart. The tuning mechanism can be accomplished anywhere on the chip, and then the light is routed to the couplers via waveguides. The goal is to bring these beams together such that they form an array with smaller pixel pitch. To accomplish this, the light is collected by a first meta-optic, labeled MS1, which lenses and steers the light beams towards the center. In the absence of a second

meta-optic, the beams will eventually cross each other and diverge in an uncontrolled way. Therefore, a second surface is required to collimate the beams and direct them upwards.

In greater detail, the meta-optic (MS1) phase consists of a steering phase ϕ_S plus a lensing phase ϕ_L, given by

$$\begin{cases} \phi_S = k \cdot x \cdot sin(\theta_x) + k \cdot y \cdot sin(\theta_y) \\ \phi_L = -k \cdot (\sqrt{f^2 + x^2 + y^2} - f) \end{cases} \tag{6.7}$$

where x and y are the spatial coordinates on each lens, $k = \frac{2\pi}{\lambda}$ is the wavenumber with $\lambda = 1.55$ μm, and θ_x and θ_y are the desired steering angles in the x and y directions, and f is the focal length. Due to the small size of the waveguides, the light diverges quickly; therefore, it is optimal to minimize the propagation distance by placing the meta-optics as close together as experimental constraints allow. In this case, the substrates are 460 μm thick, so we design for a propagation distance of 500 μm between MS1 and MS2. Therefore, the steering phase is designed to bring the beams together from 100 μm spacing to 12.5 μm spacing at the surface of MS2.

The required steering phase is well-known given the desired steering angle, which is calculated from initial and desired final locations of the beam. However, the optimal lensing phase depends on how quickly the beams are diverging from the gratings. Therefore, we fabricated a set of five meta-optics with focal lengths f = 200, 300, 400, 500, 600 μm and chose to use the one that provided the best results in experiment.

To design and model the meta-optics, I modeled the optics as phase masks and used angular spectrum method [6, 7] to propagate the beams. I modeled the grating output as Gaussian beams with $\sigma = 3.5$ μm. In the absence of any meta-optics, the beams expand quickly, as shown in Figure 6.19a. At a distance of 1 mm, the beams interfere strongly in an uncontrolled manner. However, when MS1 is used as shown in Figure 6.19b, the beams are effectively focused down and steered together. In Figure 6.19, the simulated results are shown in the top row for comparison with the experimental results in the bottom row. The simulated and experimental results are in excellent agreement.

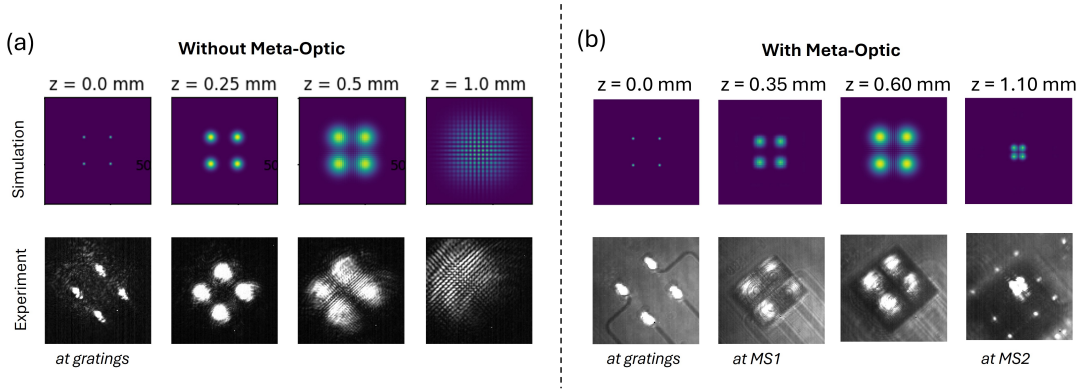

Figure 6.19: The beam aggregator simulation and experiment results. The top row is simulation and the bottom row is experient. (a) The propagated beams in the absence of any meta-optics. (b) Results with meta-optics placed at z = 0.35 mm.

In the final experiment, we used an aperture in place of a second metasurface that was designed to collimate the beams. Due to the small size of the beams at MS2, it would be very difficult if not impossible to collimate them. Firstly, tightly confined beams tend to expand quickly (following the physics of Gaussian beam propagation). Secondly, with a meta-optics pixel pitch around 500 nm, the beam is only around 20 pixels wide so only a limited amount of phase modulation can be performed. Therefore, we opted to replace the second metasurface with an array of apertures that cause the light to diffract upwards. This does reduce the amount of light through the system overall, but accomplishes the task of controlling the beam direction.

6.4 Broadband Thermal Imaging Doublets

I report briefly on our efforts to develop an inverse-designed doublet for broadband thermal imaging. Despite several iterations of design and fabrication and promising results with inverse-designed singlets for broadband imaging, we never succeeded in experimentally demonstrating a broadband doublet with performance significantly exceeding that of a single meta-optic.

The doublets herein were designed by Zhihou Zhou using Luocheng Huang's MTF-engineering code [29], and I verified myself that the designs work in theory. Ignoring losses in transmission from two layers (phase propagation only), the doublets are expected to achieve slightly higher intensity at the focal spot and slightly narrower PSFs. However, this improvement was not apparent in experiment.

6.4.1 Experiment Results

We designed and tested two sets of doublets: one in cSi on Sapphire platform, and one in all-Si platform. cSi on Sapphire has higher transmission and better fabrication quality (due to the use of e-beam lithography and a hard etching stop), but the pillar thickness is limited to 1.5 μm due to what is commercially available. For broadband meta-optics, where control of unit cell dispersion is required, this thickness is a significant limitation. Therefore, we also designed and tested a design in all-Si platform wherein the pillars are 5 μm thick for greater phase diversity.

The experimental results are summarized in Figure 6.20. For both platforms, we compare an MTF-engineered singlet, the doublet with only the back optic, and the doublet with both optics. The doublets were designed using the previously optimized singlet as the initial condition for the back optic, therefore, the back optic largely retains its ability to focus alone and the addition of the front optic acts as a corrector that is supposed to improve performance. The imaging target is illuminated by broadband hot plate illumination.

In cSi on Sapphire, the results of all three configurations are similar; see Figure 6.20a-c. All cSi on Sapphire optics are 1 cm in diameter and have 1 cm effective focal length. The designed singlet and back lens only of the designed doublet exhibit very similar results. When the front lens of the doublet was also added, we noticed an overall reduction in transmission through the optics but otherwise no significant change. I suspect that the second layer acts as a filter to reduce some strongly scattering light, but otherwise the image recorded on the camera is primarily a function of the back optic only.

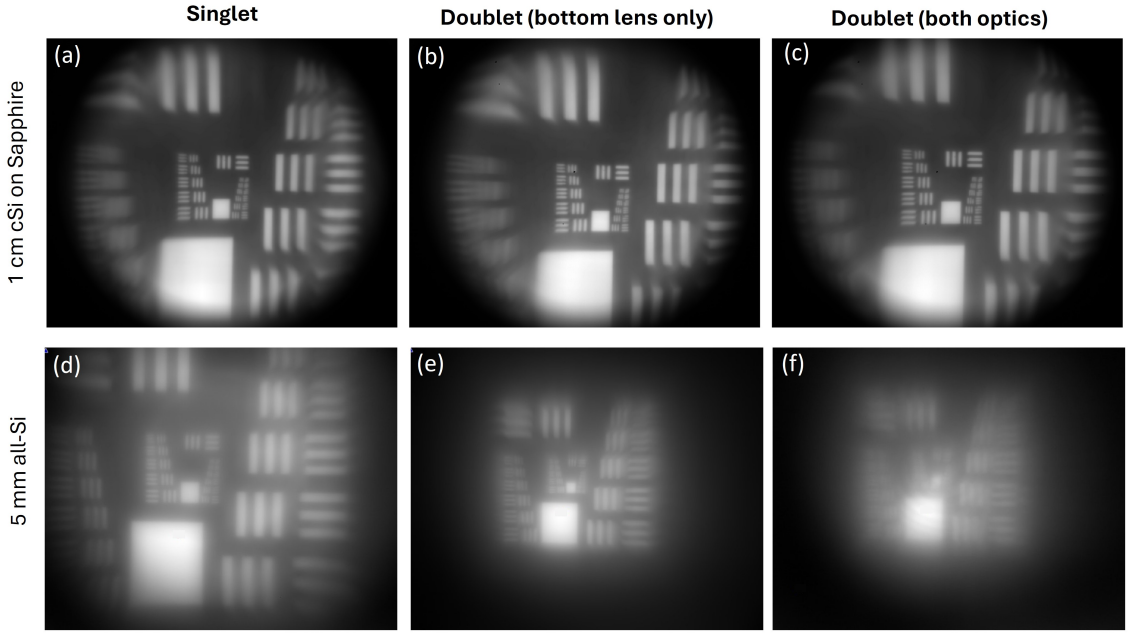

Figure 6.20: The MTF-engineered broadband doublet experiment results. The top row (a-c) shows the results for 1 cm aperture cSi on Sapphire optics, and the bottom row (d-f) shows the results for the 5 mm aperture all-Si optics. For both sets, we show the imaging result for the MTF-engineered singlet, the main focusing lens of the doublet alone, and the doublet with both optics.

We noticed a modest improvement in the image towards wider field of view, so we designed a set of all-Si doublets for wide FoV performance. To achieve wide FoV performance, some aperture restriction is required; therefore, the entrance aperture for the all-Si optics is reduced to 5 mm. In addition to the reduction in aperture, the decreased transmission of all-Si as compared to cSi on Sapphire is expected to reduce the signal to noise ratio. The all-Si results are shown in 6.20d-f. In this case, the effective focal length of the doublets (5 mm) differs from that of the singlet (1 cm), so the image sizes are different. For a true comparison, this set should be re-designed to have consistent effective focal length. Similar to the cSi set, the MTF-engineered singlet and bottom lens only of the doublet exhibit similar results.

However, in this case the addition of the front lens noticeably reduced performance. Despite attempts to tune the alignment, we were unable to improve the image quality beyond the image shown in Figure 6.20f.

6.5 Conclusions Regarding Meta-optic Doublets

From the results of this chapter, I conclude that doublets composed of meta-optics with smooth phase profiles work well in experiment, but those with irregular phase do not. The wide field of view doublet eyepiece that worked well was composed of forward-designed meta-optics with smooth phase profiles, and it worked very well. However, the inverse-designed broadband doublet did not work well, neither did two additional inverse-designed doublets that we tried for other applications.[1][2] This is in contrast to inverse-designed singlets, which often have performance exceeding that of their forward-designed counterparts. I believe the reason for the failure of inverse-designed doublets is primarily practical rather than fundamental; the inverse-designed doublets work in theory, and there is no reason to believe that they would not work as designed under perfect fabrication and alignment conditions. However, the fact that the second layer is on a separate substrate greatly increases the number of ways that the optics can be misaligned. Most of the inverse-designed doublets are designed for pixel-by-pixel accuracy. An incident plane wave is assumed, which is expected to diffract off the first optic at some angle and intersect the second optic at some particular location. For a second optic with smooth phase profile, small perturbations to this position would result in only a small change to the phase shift from the design. However, for inverse-designed meta-optics, misalignment by only a pixel may result in an entirely different phase

[1] *James' 1D to 2D SLM meta-optics:* James used TensorFlow to design a doublet to map a 1D array of point sources to a 2D array, thereby extending a 1D spatial light modulator to two-dimensions. After several unsuccessful fabrication and experiment iterations, I was tasked with verifying the design. I located one critical error - that the unit cell simulations had been performed for Si on Sapphire, but the optics were fabricated in SiN. We corrected this error and re-fabricated the device. While it worked in theory, the experimental results were still mediocre at best and the project was terminated.

[2] *Romil's Inverse Visibility Doublet:* Romil inverse-designed a doublet system that would form an image in one direction but not the other. The point spread function measurements were promising, but I was not able to experimentally demonstrate imaging with the doublet.

shift than desired. In my opinion, it is not the physical modeling or inverse design itself that is the problem; it is the design's intolerance to alignment and fabrication errors. The inverse-designed doublets do work in theory, but this seems to not translate to experiment.

An additional conclusion is that doublet meta-optics are most useful for achieving wide field of view; doublets are less useful for broadband operation. For field of view, spacing between the layers is required, which naturally leads to a doublet system. However, for chromatic aberration correction, multiple layers may simply exacerbate unwanted chromatic effects. The advantage of a second layer is that it provides additional degrees of freedom for the design. However, we hypothesize that a single layer of double the thickness or a single double-sided optic would be more effective for correcting chromatic aberrations than two separate layers.

One strategy that we have not yet employed would be to combine one forward-designed layer with one inverse-designed layer. I think that this would be interesting to try, since the forward-designed layer would provide robustness in the system. Hybrid systems consisting of one refractive optic and an inverse-designed meta-optic have shown some promise [27], so we may be able to achieve similar results with one forward- and one inverse-designed meta-optic.

Chapter 7

TRIPLETS

Meta-optics consisting of more than two layers are not common in the literature. I am aware of only two reports of meta-optic triplets. Shrestha et al [101] use a triplet to demonstrate imaging in the near-infrared with 50° field of view and $1.3 - 1.6$ μm operating bandwidth, but only 1 mm aperture and the imaging quality is qualitatively not much better than that of other meta-optics consisting of fewer layers. Pan et al. [102] use 3D printing to fabricate a multi-layer achromatic meta-optic for visible wavelengths, but for extremely small aperture (30 μm) and limited imaging quality. Therefore, the practical applications of these demonstrations would be limited.

In this chapter, I report our work on a 50° full FoV meta-optic triplet for zoom imaging at the mid-wave infrared. With relatively large aperture (8 mm), we achieved good imaging quality. We were initially skeptical that this project would work, given our difficulties with broadband doublets in the past and concerns about transmission efficiency through multiple layers; however, this project was highly successful.

7.1 MWIR Zoom Lens

The contents of this section are adapted from [103]: *Anna Wirth-Singh, Arturo Martin Jimenez, Minho Choi, Johannes E. Fröch, Rose Johnson, Tina Le Teichmann, Zachary Coppens, and Arka Majumdar. Meta-Optics for Zoom Imaging at Mid-Wave Infrared. arXiv Preprint https://arxiv.org/abs/2407.11255v1, July 2024*, with permission from the authors.

7.1.1 Introduction

MWIR imaging is especially attractive for long-range imaging and sensing due to its superior penetration in high-humidity atmospheric conditions [104]. In these applications, wide field of view and high resolution are often desirable. For imaging dynamic targets, it is particularly helpful to have both wide field of view images for context and narrow field of view for zoomed-in detail, with rapid switching mechanism between the views. However, achieving both qualities simultaneously requires a large, high-resolution camera sensor, and such sensors are particularly expensive at MWIR wavelengths. Alternatively, these applications can benefit from zoom functionality, wherein the image magnification is changed by repositioning optics within the lens system so that a range of image magnifications can be captured using a single aperture and sensor.

Most conventional zoom systems are composed of a series of refractive lenses, some of which are axially translated to change the zoom state. While effective, stacked refractive lenses quickly become heavy, which is undesirable for many applications where zoom functionality is required, such as airborne scopes and cameras. Due to the long total track length of zoom imaging systems, excess weight can cause significant torque on the mechanical support system. In addition, to achieve high quality imaging with zoom constraints, aspheric lenses are often used [105, 106] that are difficult to manufacture due to non-constant curvature across the surface. Combined with the limited availability of suitable materials for MWIR refractive lenses, such as germanium and calcium fluoride, this contributes to the increased cost of thermal zoom imaging systems.

In this work, we demonstrated an 8 mm aperture, 50° full field of view (FoV) zoom imaging meta-optic triplet at 3.4 μm wavelength. We followed the traditional approach by varying the position of two of the three meta-optic elements to increase the image magnification from 1x to 5x. Additionally, our zoom imaging system is parfocal, meaning that the focal plane remains fixed while achieving the intermediate zoom states. For optimal transmission through the triplet lens system, we realize the meta-optics in a silicon-on-sapphire

material platform. We demonstrate high-quality imaging performance up to 50° FoV in the wide field of view configuration.

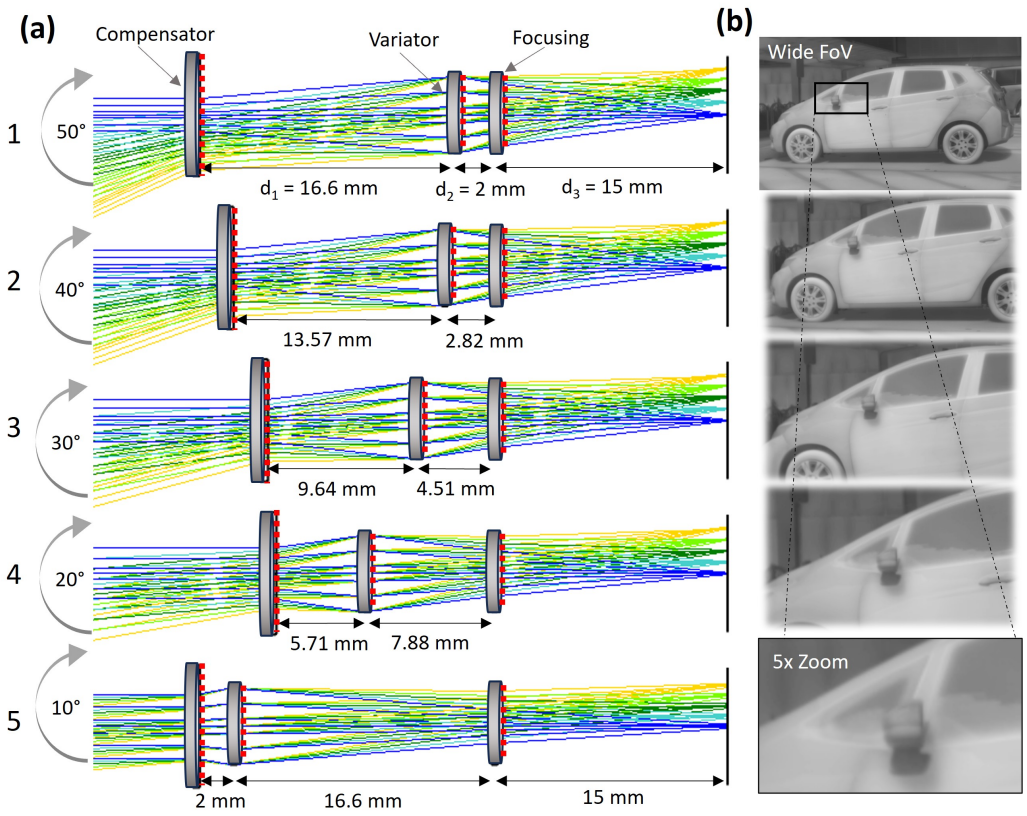

Figure 7.1: The zoom lens concept. (a) Ray tracing diagrams for all five configurations. By translating the compensator and variator optics, the effective focal length of the system is changed from wide field of view (top) to narrow field of view (bottom). The blue lines represent normally incident rays, while the yellow rays represent 25° and 5° angle of incidence for the wide and narrow configurations, respectively. Intermediate angles are shown in shades of green. (b) Illustration of zoom imaging on a car. Under 5x zoom, the details of the side mirror and windows become clear.

7.1.2 Zoom Lens Design

At minimum, most optical zoom systems consist of a mechanically adjustable afocal frontend and imaging backend. In order to keep a fixed back focal length, the front part of the system must be composed of two moving groups [107], resulting in a triplet lens system. The design for the meta-optic zoom lens follows this standard three-group zoom structure (consisting of a compensator, a variator, and a focusing optics) and the zoom behavior is schematically depicted in Figure 1. The system is optimized for five discrete zoom states, denoted configurations 1 through 5, with this change accomplished by varying the axial distances between the metasurfaces. Specifically, the meta-optic nearest the sensor, termed the focusing optic, remains a fixed 15 mm distance from the sensor while the positions of the other two optics (denoted as the compensator optic nearest the object and the variator optic in the middle) are adjusted to change the zoom state. This change is primarily accomplished by axially translating the variator optic, which is adjusted within a range of 14.6 mm. The compensator optic has negative power to defocus the light and its axial position is adjusted within a smaller range of 5.21 mm to correct for aberrations. Ray tracing diagrams of all configurations are shown in Figure 7.1a.

The designed F-number, effective focal length (EFL), and full field of view of each configuration are summarized in Table 7.1. Configuration 1, also called the "wide" configuration, provides the widest field of view at 50° full FoV and F-number of 3.7. Configuration 5, also called the "tele" configuration, provides the most zoomed-in image with 10° full FoV at an F-number of 8.0. The intermediate Configurations 2 through 4 provide equally spaced intermediate zoom states.

The phase profiles of the meta-optics were optimized using commercial ray tracing software (Zemax OpticStudio). Each meta-optic was modeled as a Binary-2 phase profile according to the equation

$$\Phi(\rho) = \sum_{i=1}^{6} A_i \left(\frac{\rho}{M}\right)^{2i} \tag{7.1}$$

where M is a normalization constant, ρ is the radial coordinate, and A_i are polynomial

Table 7.1: System Design Specifications

Configuration	1 (Wide)	2	3 (Mid)	4	5 (Tele)
F Number	3.71	3.94	4.40	5.33	7.98
EFL (mm)	8.78	10.53	14.19	21.74	43.89
Full FoV	50°	40°	30°	20°	10°
d_1 (mm)	16.60	13.57	9.64	5.71	2.00
d_2 (mm)	2.00	2.82	4.51	7.88	16.60

coefficients. To optimize the zoom system, we initially varied the phase profile coefficients A_i to optimize performance at both the tele and wide configurations at predetermined positions. Specifically, wavefront error (with respect to an ideal spherical wavefront) was defined as the merit function during optimization. Once the phase for each metasurface was determined, the spacings between the surfaces were varied to obtain the desired intermediate zoom states. As labeled in Figure 7.1a, the distance between the compensator and variator optics is denoted d_1 and the distance between the variator and the focusing optics is denoted d_2. The distance between the focusing lens and the image plane, denoted d_3, was held constant at 15 mm while d_1 and d_2 were allowed to vary.

7.1.3 Meta-Optics Design and Fabrication

The meta-optics are physically realized as crystalline silicon pillars on sapphire substrate (commercially available from UniversityWafer). While silicon is transparent at MWIR wavelengths, bulk silicon incurs significant Fresnel reflections due to its high index of refraction (n = 3.5) as compared to the air (n = 1) [15]. Therefore, to provide increased transmission efficiency in the multi-layer system, we chose sapphire (n = 1.7) substrate. Transmission through the sapphire substrate is expected to be 93%. The silicon pillars are 1.5 μm tall arranged on a lattice with periodicity 1.5 μm, and the sapphire substrate thickness is 460

μm. Using rigorous coupled wave analysis [70], we simulated the phase and transmission of silicon pillars as a function of pillar width as shown in Figure 7.2c. From these results, we selected ten pillars with widths ranging from 500 nm to 1.0 μm to comprise the pillar library.

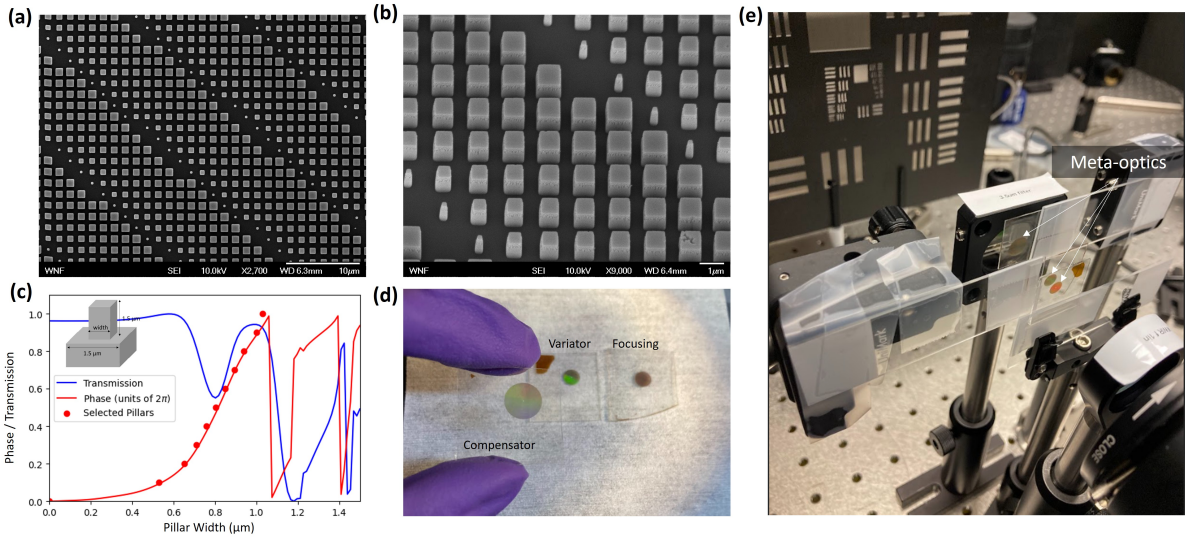

Figure 7.2: Metasurface design and fabrication. (a) Top-down SEM image of a fabricated optic. (b) SEM image of a fabricated optic taken at a slightly oblique (10°) angle, illustrating fabrication quality. (c) The simulated phase (red) and transmission (blue) of the unit cell. The widths selected for the pillar library are denoted by red circles. (d) A photograph of the fabricated optics. A person is holding the compensator optic in the foreground while the variator (left) and focusing (right) optics are resting on the table in the background. (d) A photograph of the meta-optics in the experiment setup.

The meta-optics were fabricated using electron beam lithography and inductively coupled plasma etching. All three meta-opics were fabricated from a single 1.5 μm thick silicon-on-sapphire wafer that was diced into chips. Each sample was cleaned in acetone and isopropyl alcohol before an oxygen plasma treatment to promote resist adhesion. Next, we spin-coated ZEP-520A resist and exposed the resist by electron beam lithography. After writing the pattern, we developed the resist in amyl acetate followed by a short oxygen plasma treatment

to remove residue. In order to achieve a large etching depth of 1.5 μm, we deposited a hard mask for etching. Specifically, we deposited 70 nm of alumina on top of the patterned samples via electron beam evaporation. To form the hard mask, we lift-off the resist with N-Methyl-2-pyrrolidone. Finally, the silicon was etched via reactive ion etching with SF6 and C4F8 gas chemistry.

Top-down and oblique scanning electron microscope (SEM) images of the fabricated optics are shown in Figure 7.2a and b, respectively, illustrating the fabrication quality. A photograph of the fabricated optics is shown in Figure 7.2d. Except for the meta-optic area, the thin silicon layer has been etched away, revealing the transparent substrate. The surface of the optic, while appearing opaque brown under visible illumination, is transparent under infrared illumination.

7.1.4 Experiment Imaging Results

The imaging quality of the meta-optical system was characterized in a simple experimental setup consisting of an illumination source and target object, a narrowband filter, the meta-optics, relay optics, and a camera sensor. A photograph of the fabricated optics in the measurement setup is shown in Figure 7.2e. As the source of MWIR illumination, we use a hot plate (Torrey Pines Scientific HP50) set to 130°C. This provides broadband infrared radiation that we filter to a narrower band near the design wavelength using a narrowband filter (Thorlabs FB3500-500, with 3.5 μm center wavelength and FWHM bandwidth of 500 nm). A matte black anodized aluminum target projecting the USAF 1951 resolution chart is placed just after the hot plate to form the imaging object. In order to demonstrate imaging up to 50° FoV, we place the target at a distance D from the first meta-optic such that the edges of the target are 25° from normal incidence. For our target which is 12.5 cm wide, this corresponds to $D = 13.4$ cm in imaging experiments. Images were collected on a FLIR A6751 MWIR InSb camera sensor with 640 $\times$ 512 pixels at 15 μm per pixel resolution. Due to the camera sensor being located further than the designated 15 mm back focal length inside the protective camera housing, it was necessary to use relay optics to re-image the meta-optics

image onto the sensor. For this purpose, we used an F/1 MWIR-coated, germanium plano-convex singlet lens (Edmund Optics #69-649, 25 mm focal length) with an F/2.5 compound refractive lens assembly (FLIR #4218538, 25 mm focal length). To ensure that the relay optics do not restrict measurement of the meta-optics, we ensure that the numerical aperture (NA) of the relay optics ($NA > 0.45$) exceeds the maximum NA of the meta-optic zoom system ($NA = 0.42$). The relay optics additionally aid in precise alignment of the system, as described below.

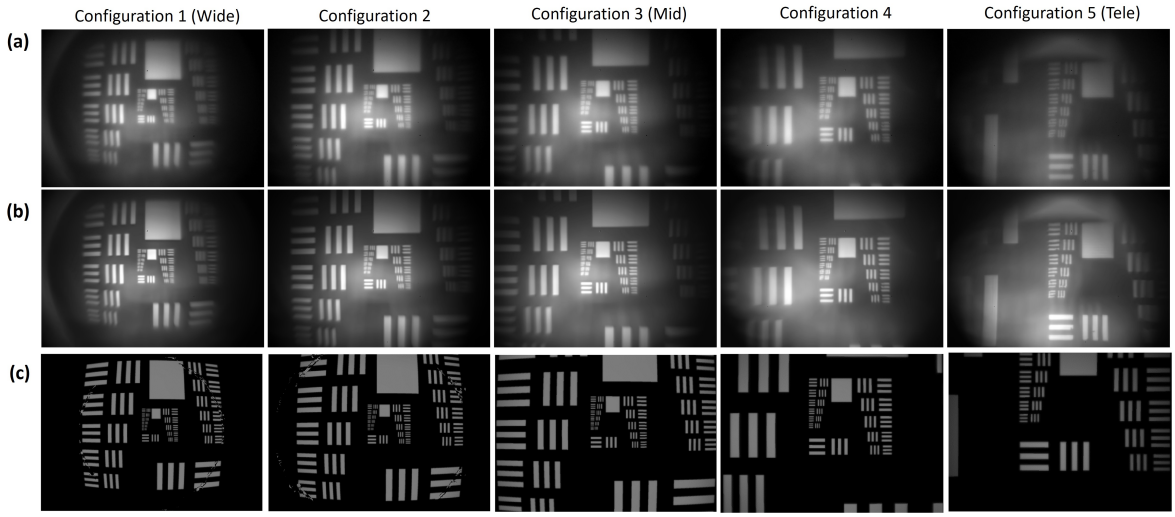

Figure 7.3: Simulated and experimental imaging results. (a) Experiment imaging results for Configurations 1 (left) through 5 (right). The imaging object, a hot plate and USAF resolution chart, is placed such that the edges of the target cover 50° FoV with respect to the meta-optics. (b) Experimental results that have been computationally enhanced with sharpening and denoising. (c) Simulated imaging results via ray tracing.

To place and align the meta-optics, we first mounted each meta-optic on a glass microscope slide as shown in Figure 2e in the main text. Due to the small distances separating the optics (a minimum of 2 mm), care must be taken to mount the surfaces in a way that provides fine control but does not hinder axial motion. In future efforts, a 3D printed holder

could be utilized to facilitate alignment. In this work, we developed a procedure to manually align the meta-optics triplet in the laboratory. First, the relay optics in front of the camera sensor are focused onto the surface of the focusing optic, which is aligned such that the meta-optic surface is in focus and centered in the camera's field of view. Similarly, the variator meta-optic is placed just behind the focusing optic; the outline of the variator optic can be seen through that of the focusing optic and adjusted to achieve alignment. The alignment of the variator meta-optic is most critical to the operation of the triplet system, so the variator meta-optic is mounted on a 3-axis stage for independent control of X, Y, and Z translation as well as tilt. Once the positions of the focusing and variator optics are fixed, the camera system (mounted on a micrometer translation stage) is translated back 15 mm, which is the fixed back focal length of the triplet meta-optics, for measurement in the desired focal plane. Finally, the compensator optic was placed manually to optimize the image quality in each configuration.

The simulated and experimental imaging results for all five configurations are shown in Figure 7.3, with the USAF resolution target positioned such that the horizontal edges of the imaging target correspond to 50° full FoV. To correct for noise due to ambient radiation on the sensor, we performed a flat field correction on all experimental results by collecting an image with the object blocked and subtracting that background image from the signal; the resulting image captures are shown in Figure 7.3a. We observe good imaging quality and close agreement with the simulated results shown in Figure 7.3c. However, the somewhat broad linewidth of the illumination source (approximately 500 nm FWHM with the narrowband filter) introduces chromatic aberrations that reduce the sharpness of the image as compared to a single-wavelength measurement. To mitigate this effect, simple computational postprocessing techniques can be introduced to improve the image quality. In Figure 7.3b, we show the experiment imaging results after postprocessing with a Gaussian kernel sharpening filter and bm3d denoising algorithm [31]. While there still exists some diffuse noise that we attribute primarily to reflections from the narrowband filter, the USAF groups are effectively sharpened for close qualitative agreement with the simulated single-wavelength

results in Figure 7.3c. Moving from left to right, the system exhibits clear zoom functionality and qualitatively good imaging performance in Configurations 1 through 5, as well as close agreement between the simulation and experiment.

7.1.5 Discussion

While this zoom lens system was optimized for single wavelength illumination at 3.4 μm, we demonstrate high-quality imaging over a wavelength band of approximately 500 nm. In meta-optics (and other forms of diffractive optics) with set phase wraps, the focal length is inversely proportional to the optical wavelength [19]. Therefore, light of different wavelengths does not focus in the same plane, leading to chromatic aberrations. Despite this effect, we demonstrate relatively good imaging quality with the addition of a narrowband filter. While single-wavelength rather than broadband illumination is predicted to improve imaging performance in simulation, further filtering ambient light to a narrower range would also reduce the signal to noise ratio (SNR) due to the reduced light entering the system, unless some active illumination source (such as an LED or laser) is used to illuminate the target. However, such active illumination would be impractical for many applications of this zoom system, such as remote sensing. Therefore, we present imaging results over a broader band, for higher SNR, coupled with computational postprocessing to regain some quality lost due to undesirable chromatic effects. Extension to broader bandwidth operation may be possible using dispersion engineering [10] to match the required phases over a range of wavelengths or applying inverse design techniques [29] to extend the operating wavelength range.

In multi-element optical systems such as this one, misalignment can have deleterious effects on lens performance. To quantify the effects of misalignment on the performance of the system, we conducted a tolerance analysis of Configuration 1 in Zemax at the design wavelength of 3.4 μm, shown in Figure 7.4. The nominal MTF is shown in Figure 7.4a. In the absence of misalignment, the imaging performance is nearly diffraction limited at normal incidence and decreases slightly at larger angles of incidence. As a metric of lens system performance, we report the average (sagittal and tangential) MTF at 20 lp/mm

resolution as a function of alignment tolerances.

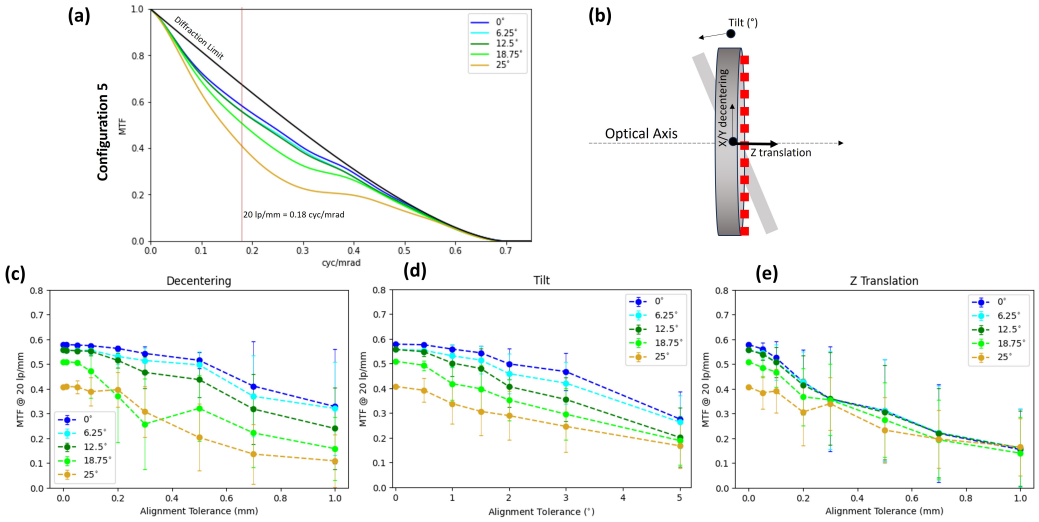

Figure 7.4: Tolerance to meta-optic misalignment. (a) Nominal MTF for Configuration 1 for angles of incidence up to 25°. The reported MTF is the average over both sagittal and tangential directions. The diffraction limit is plotted in black for comparison. The vertical red line indicates the 20 lp/mm = 0.18 cyc/mrad resolution that was chosen as a metric for the tolerance analysis. (b) Schematic depicting the categories of misalignments that were considered. In the Monte Carlo analysis, all three metasurfaces were misaligned according to the specified tolerances. (c)-(e) Tolerance analysis for the wide configuration. For each field (up to 25°), we plot the MTF at 20 lp/mm as a function of allowed misalignment. The misalignment is decentering in (c), tilt in (d), and axial translation in (e). The error bars represent one standard deviation from Monte Carlo analysis consisting of 20 trials.

As illustrated in Figure 7.4b, we specifically consider the effects of translation in Z (axial displacement), translation in X/Y (decentering), and rotation about the X axis (tilt). We varied each category of misalignment separately in this analysis. In detail, we conducted a Monte Carlo analysis comprising 20 trials wherein each element was misaligned by a random amount within the specified tolerance along the horizontal axis. We considered reasonable

experimental alignment tolerances of up to 1 mm of translation and up to 5° of tilt in each element. In Figure 7.4c through 7.4e, we report the average MTF value as a function of worsening misalignment for angles of incidence up to 25°. As expected, the average MTF decreases with increasing misalignment, however this decrease is approximately linear. This indicates robustness in the system that we attribute to the relatively small phase gradient of each metasurface.

Our meta-optics-based zoom lens system achieves a zoom range of 5x, which is sufficient for many applications. To further increase the zoom range, it would generally require decreasing the NA of the system, which results in reduced imaging quality and field of view [105]. Similarly to refractive optics, additional layers of optics provide degrees of freedom that can be used to improve performance and achieve additional functionalities, such as increased zoom range. This successful demonstration of a meta-optic triplet system highlights the potential for meta-optics to replace refractive elements in increasingly complex multi-layer and multi-functional imaging systems. In particular, we envision meta-optical systems like this one finding utility in weight-constrained systems requiring zoom functionality and wide field of view, such as airborne remote sensing applications.

Chapter 8

CONCLUSION AND FUTURE WORK

In this final chapter, I summarize my findings about multi-layer meta-optics and remark on directions for future work.

8.1 Singlets, Doublets, and Triplets

Having worked on several multi-layer meta-optical systems, I can draw some empirical conclusions about those that worked well versus those that did not work well. The systems I reference to draw these conclusions are summarized in Figure 8.1.

Project	Design Strategy	Success
Doublet eyepiece	Forward design (Zemax)	Excellent match with theory
MWIR zoom triplet	Forward design (Zemax)	Excellent match with theory
Beam aggregator	Forward design to accomplish 2D beam steering	Achieved expected results
Inverse visibility doublet	Inverse design – effectively hyperboloid + noise	Good PSFs but unable to accomplish imaging
1D to 2D SLM	Inverse design (TensorFlow) to accomplish 2D beam steering	Not working as designed
Broadband MWIR doublet	Inverse design (MTF engineering)	Doublets worse than singlets

Figure 8.1: Experimental success of multi-layer meta-optic designs.

The projects are listed in descending order by their experimental success. Upon inspecting this table, a pattern emerges: multi-layer meta-optics that were forward-designed worked quite well, whereas those that were inverse-designed did not work as well. In particular, both

the eyepiece doublet and the MWIR zoom triplet were highly successful projects requiring only one round of fabrication and resulting in a publication. I do note that forward-designed doublet and triplet systems seem more sensitive to chromatic aberrations than their single-layer counterparts, but at the design wavelength they functioned exactly as designed. The beam aggregator also worked as designed but was a less ambitious target than the eyepiece or zoom triplet.

Moving down the list, the inverse visibility doublet is an ongoing project that has so far yielded mixed results. The idea was a doublet system that performed imaging in one direction but not the other. While inverse design techniques were used, in retrospect the optics function like two hyperboloid meta-optics whose focal lengths coincide in one direction but not the other. We hypothesize that added randomness from inverse design increases the contrast between the forward and background directions. However, if local averaging over the phase profiles is performed, ordinary lens phase profiles are recovered. The initial point spread function measurements of these optics were promising but so far our attempts to perform imaging have been unsuccessful. This indicates to me that practical rather than fundamental issues are limiting these optics from functioning as desired. Similarly, the 1D to 2D SLM exhibited some indications that it was working in experiment, but this indication was extremely weak. The goal of this doublet was to steer and collimate a 1D array of beams into a 2D array; in retrospect, this could have been accomplished with a forward-designed lenslet array similar to the beam aggregator, and I suspect that approach would have worked. Finally, the broadband MWIR doublet effort has exhibited the least amount of success (and also the greatest amount of effort). Given the empirical observation that chromatic aberrations are worse in multi-layer than single-layer meta-optics, it is not surprising that a poorly-aligned inverse-designed doublet for chromatic aberration correction exhibits poor performance. I emphasize that all of these designs perform well in simulation, but for reasons not fully understood this is difficult to realize experimentally.

An additional conclusion that can be drawn from these projects is that multi-layer systems are most useful for increasing the field of view of an optical system. The successful doublet

eyepiece and MWIR zoom triplet were focused on achieving wide field of view imaging, and the beam aggregator was for beam steering which is highly related to field of view. For chromatic aberration correction, we hypothesize that there is no theoretical benefit to spatially separating the layers. We hypothesize that a single layer of pillars with double the height (for greater control over chromatic dispersion) would exceed the performance of two separate layers for narrow field of view broadband imaging.

8.2 The Particular Advantages of Meta-Optics for Thermal Imaging

An additional area of focus in this thesis is meta-optics for thermal (MWIR and LWIR) imaging. This is largely due to funding for projects in this wavelength range, but for good reason. The MWIR and LWIR wavelength ranges indispensable for applications spanning consumer electronics to defense, including night vision, non-contact thermography, and long-range atmospheric, geological, and agricultural sensing. In most, if not all, thermal imaging applications, the size and weight of the imaging system may be highly constrained. For example, night vision goggles require compact form-factor and light weight because an excess of size or weight can cause fatigue and discomfort for the user. In many long-range sensing applications, the imaging system is mounted on an airborne unit or drone, where excess weight is unacceptable. Many defense applications require discreet and compact imaging systems that can be integrated into larger, multi-functional devices. However, high-quality imaging typically requires compound lens assemblies, so there is a trade-off between form-factor and optical performance. Especially for thermal wavelengths, these complex assemblies are also expensive and difficult to manufacture due to the limited availability of suitable refractive lens materials. Therefore, improving the form-factor and utility of thermal imaging systems is an active area of research.

Significant work has been undertaken in the field of meta-optics for imaging at visible wavelengths in particular, motivated by consumer-facing applications in compact cameras and augmented/virtual reality. While the physical principles guiding design and operation of thermal meta-optics are the same as those that apply to visible meta-optics (with ad-

justments to physical size scaling and material platforms), investigation into thermal meta-optics specifically is especially warranted because meta-optics are extremely well-suited to the unique imaging applications of this wavelength range. Compared to the visible imaging range, applications in the thermal range are more defense-focused, emphasizing compact form-factor and multi-functionality over high-quality full-color imaging. In addition, while advancements in sensor technologies have made thermal imaging accessible to local governments and commercial entities, thermal imaging sensors are still significantly more expensive than visible sensors. Therefore, it is practical to design multifunctional optics rather than purchase additional sensors for different applications. Due to the limited resolution of the sensor itself, the requirements of thermal imaging optics are typically less stringent on resolution and place greater emphasis on functions such as magnification factor and field of view. Large aperture is an another frequently desired aspect of thermal imaging systems in order to increase the signal-to-noise ratio over long range or low-signal environments. These are all areas in which meta-optics can excel, so we argue that meta-optics are naturally aligned with the needs of thermal imaging applications.

8.3 Concluding Remarks

The future of multi-layer meta-optical systems is promising, but to fully leverage the utility of meta-optics there are some issues that need to be resolved. Specifically, pixel-by-pixel phase control is a key strength of meta-optics that has not been successfully implemented in multi-layer systems. Especially for doublet systems where it is more difficult to argue for advantages related to the thinness of meta-optics, it would be advantageous to utilize their sub-wavelength phase control. However, doublet systems attempting to leverage this aspect have not yet worked as well as expected. More work is required to investigate the reason for this discrepancy. My hypothesis is that it is a practical issue related to extremely narrow alignment tolerance, but this hypothesis is yet to be tested.

To investigate this issue more fully, I suggest studying intermediate cases between forward-designed doublets and inverse-designed doublets. It is critical to determine where and why

the discrepancy between simulation and experiment emerges. To probe this, I suggest two studies:

1. A doublet consisting of one smooth phase meta-optic and one discontinuous phase meta-optic. Alternatively, a hybrid system consisting of one refractive lens and one inverse-designed meta-optic could be investigated. In this study, it would also be interesting to investigate whether the order of the smooth and non-smooth meta-optics is important.

2. A series of doublets exhibiting increasing randomness in both layers. For example, two hyperboloids could be designed as an initial condition for optimization and then the performance of optics at intermediate stages of inverse design could be experimentally tested.

It has been a great joy to contribute to research in meta-optics. Working in this field has provided opportunities probe the light-matter interaction at a fundamental level, develop electromagnetic design and simulation tools, and apply state-of-the-art nanofabrication and measurement techniques. Meta-optics is an exciting field with great promise, and I am excited to see what will come in the future of meta-optics.

BIBLIOGRAPHY

[1] Nanfang Yu and Federico Capasso. "Flat optics with designer metasurfaces". In: *Nature Materials* 13 (2014), pp. 139–150.

[2] Francesco Aieta et al. "Aberration-Free Ultrathin Flat Lenses and Axicons at Telecom Wavelengths Based on Plasmonic Metasurfaces". In: *Nano Letters* 12.9 (2012), pp. 4932–4936. DOI: 10.1021/nl302516v.

[3] Mingbo Pu et al. "Nanoapertures with ordered rotations: symmetry transformation and wide-angle flat lensing". In: *Optics Express* 25.25 (2017). DOI: 10.1364/OE.25.031471.

[4] Augusto Martins et al. "On metalenses with arbitrarily wide field of view". In: *ACS Photonics* 8.7 (June 2020), pp. 2073–2079. URL: https://pubs.acs.org/doi/10.1021/acsphotonics.0c00479.

[5] Nanfang Yu et al. "Light Propagation with Phase Discontinuities: Generalized Laws of Reflection and Refraction". In: *Science* 334.6054 (Sept. 2011), pp. 333–337. URL: https://doi.org/10.1126/science.1210713.

[6] J. W. Goodman. *Introduction to Fourier Optics*. Englewood, Colorado: Robers & Company Publishers, 2005.

[7] K. Matsushima and T. Shimobaba. "Band-Limited Angular Spectrum Method for Numerical Simulation of Free-Space Propagation in Far and Near Fields". In: 17.22 (2009), pp. 19662–19673.

[8] R. W. Gerchberg. "A Practical Algorithm for the Determination of Phase from Image and Diffraction Plane Pictures." In: *Optik* 35 (1972), pp. 237–246.

[9] Maoxiong Zhao et al. “Phase characterisation of metalenses”. In: *Light: Science and Applications* 10.52 (2021). URL: https://doi.org/10.1038/s41377-021-00492-y.

[10] Wei Ting Chen, Alexander Y. Zhu, and Federico Capasso. “Flat optics with dispersion-engineered metasurfaces”. In: *Nature Reviews Materials* 5 (2020), pp. 604–620. DOI: 10.1038/s41578-020-0203-3.

[11] V. Liu and S. Fan. “S4: A free electromagnetic solver for layered periodic structures”. In: *Computer Physics Communications* 183 (2012), pp. 2233–2244.

[12] Maksym Zhelyeznyakov et al. “Large area optimization of meta-lens via data-free machine learning”. In: *Communications Engineering* 2.60 (2023).

[13] Lucas H. Gabrielli. “gdstk”. In: *Python Package* (2020). URL: https://heitzmann.github.io/gdstk/.

[14] Joon-Suh Park et al. “All-Glass 100 mm Diameter Visible Metalens for Imaging the Cosmos”. In: *ACS Nano* 18.4 (2024), pp. 3187–3198.

[15] J. T. Cox and G. Hass. “Antireflection Coatings for Germanium and Silicon in the Infrared”. In: *JOSA* 48.10 (1958), pp. 677–680. DOI: 10.1364/JOSA.48.000677.

[16] Halil Can Nalbant et al. “Transmission optimized LWIR metalens”. In: *Applied Optics* 61.33 (2022). DOI: 10.1364/AO.469805.

[17] Francesco Aieta et al. “Aberrations of flat lenses and aplanatic metasurfaces”. In: *Optics Express* 21.25 (Dec. 2013), pp. 31530–31539. URL: https://doi.org/10.1364/OE.21.031530.

[18] Elyas Bayati et al. “Inverse designed extended depth of focus meta-optics for broadband imaging in the visible”. In: *Nanophotonics* (2021).

[19] Luocheng Huang et al. “Full-Color Metaoptical Imaging in Visible Light”. In: *Advanced Photonics Research* 3.5 (2016). DOI: 10.1002/adpr.202100265.

[20] Johannes E. Fröch et al. "Beating bandwidth limits for large aperture broadband nano-optics". In: *Arxiv Preprint* (Feb. 2024). URL: https://doi.org/10.48550/arXiv.2402.06824.

[21] Ethan Tseng et al. "Neural nano-optics for high-quality thin lens imaging". In: *Nature Communications* 12.6493 (Nov. 2021). URL: https://doi.org/10.1038/s41467-021-26443-0.

[22] Johannes E. Fröch et al. "Dual band computational infrared spectroscopy via large aperture meta-optics". In: *ACS Photonics* (2022).

[23] Shane Colburn et al. "An optical frontend for a convolutional neural network". In: *Applied Optics* 58.12 (2019), pp. 3179–3186.

[24] Hanyu Zheng et al. "Meta-optic accelerators for object classifiers". In: *Science Advances* 8.30 (2022).

[25] Adolf W. Lohmann. "Scaling laws for lens systems". In: *Applied Optics* 28 (Dec. 1989), pp. 4996–4998.

[26] Feng Zhao et al. "Synthetic aperture metalens". In: *Photonics Research* 9.12 (2021), pp. 2388–2397. URL: https://doi.org/10.1364/PRJ.440185.

[27] Samuel Pinilla et al. "Miniature color camera via flat hybrid meta-optics". In: *Science Advances* 9.21 (May 2023). DOI: 10.1126/sciadv.adg7297.

[28] Federico Presutti and Francesco Monticone. "Focusing on bandwidth: achromatic metalens limits". In: *Optica* 7.6 (June 2020), pp. 624–631. URL: https://doi.org/10.1364/OPTICA.389404.

[29] Luocheng Huang et al. "Broadband thermal imaging using meta-optics". In: *Nature Communications* 15.1662 (2024). DOI: 10.1038/s41467-024-45904-w.

[30] Luocheng Huang et al. "Design and analysis of extended depth of focus metalenses for achromatic computational imaging". In: *Photonics Research* 8.10 (Sept. 2020), pp. 1613–1623.

[31] Ymir Mäkinen, Lucio Azzari, and Alessandro Foi. "Collaborative filtering of correlated noise: exact transform-domain variance for improved shrinkage and patch matching". In: *IEEE Transactions on Image Processing* 29 (Aug. 2020), pp. 8339–8354. URL: https://ieeexplore.ieee.org/document/9165941.

[32] Anna Wirth-Singh et al. "Compressed Meta-Optical Encoder for Image Classification". In: *arXiv Preprint* (June 2024). URL: https://doi.org/10.48550/arXiv.2406.06534.

[33] Alex Krizhevsky, Ilya Sutskever, and Geoffrey E Hinton. "Imagenet classification with deep convolutional neural networks". In: *Advances in neural information processing systems* 25 (2012).

[34] X. Li et al. "Performance analysis of gpu-based convolutional neural networks." In: *45th ICPP* (2016), pp. 67–76.

[35] P. L. McMahon. "The Physics of Optical Computing." In: *Nat. Rev. Physics* 5 (2023), pp. 717–734.

[36] J. Chang et al. "Hybrid optical-electronic convolutional neural networks with optimized diffractive optics for image classification." In: *Scientific Reports* 8 (2018), p. 12324.

[37] S. Colburn et al. "Optical frontend for a convolutional neural network." In: *Applied Optics* 58.12 (2019), pp. 3179–3186.

[38] M. Yang et al. "Optical convolutional neural network with atomic nonlinearity." In: *Optics Express* 31.10 (2023), pp. 16451–16459.

[39] L. Cutrona et al. "Optical data processing and filtering systems." In: *IRE Trans. Inf. Theory* 6.3 (1960), pp. 386–400.

[40] J. N. Mait, G. W. Euliss, and R. A. Athale. "Computational imaging." In: *Adv. Opt. Photon.* 10 (2018), pp. 409–483.

[41] Carlos Mauricio Villegas Burgos et al. “Design framework for metasurface optics-based convolutional neural networks”. In: *Appl. Opt.* 60.15 (May 2021), pp. 4356–4365.

[42] Z. Hu et al. “High-Throughput Miltichannel Parallelized Diffraction Convolutional Neural Network Accelerator.” In: *Laser Photonics Rev.* 16 (2022), p. 2200213.

[43] W. Lohmann and W. T. Rhodes. “Two-pupil synthesis of optical transfer functions”. In: *Appl. Opt.* 17.7 (1978), pp. 1141–1151.

[44] J. N. Mait and W. T. Rhodes. “Two-pupil synthesis of optical transfer functions: 2: Pupil function relationships”. In: *Appl. Opt.* 25.12 (1986), pp. 2003–2007.

[45] J. N. Mait. “Pupil-function design for complex incoherent spatial filtering”. In: *JOSA* 4.7 (1987), pp. 1185–1193.

[46] K. Wei et al. “Spatially Varying Nanophotonic Neural Networks.” In: *Arxiv* (2023), p. 2308.03407.

[47] Alex Krizhevsky, Ilya Sutskever, and Geoffrey E Hinton. “ImageNet Classification with Deep Convolutional Neural Networks (AlexNet) ImageNet Classification with Deep Convolutional Neural Networks (AlexNet) ImageNet Classification with Deep Convolutional Neural Networks”. In: ().

[48] Jinlin Xiang et al. “Knowledge distillation circumvents nonlinearity for optical convolutional neural networks”. In: *Applied Optics* 61.9 (2022), pp. 2173–2183.

[49] A. Ryou et al. “Free-space Optical Neural Network Based on Thermal Atomic Nonlinearity.” In: *Photon. Res.* 9 (2021), B128–B134.

[50] T. Wang et al. “Image sensing with multilayer nonlinear optical neural networks.” In: *Nature Photonics.* 17 (2023), pp. 408–415.

[51] H. Zheng et al. “Meta-optic accelerators for object classifiers.” In: *Science Advances* 8.30 (2022).

[52] T. Zhou et al. “Large-scale Neuromorphic Optoelectronic Computing with a Reconfigurable Diffractive Processing Unit.” In: *Nature Photonics* 15 (2021), pp. 367–373.

[53] L. Huang et al. “Photonic advantage of optical encoders.” In: *Nanophotonics.* (2023).

[54] S. B. Damelin and W. Miller. *The Mathematics of Signal Processing.* Cambridge, UK: Cambridge University Press, 2011.

[55] *Phase Retrieval II: Iterative Transform Algorithms.* https://www.retrorefractions.com/blog/phase-retrieval-02/. 2023.

[56] *PRAISE.* https://github.com/brandondube/praise/tree/master. 2019.

[57] Ji Ma and Yuyu Yuan. “Dimension reduction of image deep feature using PCA”. In: *Journal of Visual Communication and Image Representation* 63 (2019), p. 102578.

[58] Gordana Ivosev, Lyle Burton, and Ron Bonner. “Dimensionality reduction and visualization in principal component analysis”. In: *Analytical chemistry* 80.13 (2008), pp. 4933–4944.

[59] H. Zheng et al. “Multichannel meta-imagers for accelerating machine vision.” In: *Nature Nanotechnology.* 59 (2024).

[60] Anna Wirth-Singh et al. “Large field-of-view thermal imaging via all-silicon metaoptics”. In: *Applied Optics* 62.20 (2023), pp. 5467–5474.

[61] James Kumler and Martin Bauer. “Fish-eye lens designs and their relative performance”. In: *Proc. SPIE 4093, Current Developments in Lens Design and Optical Systems Engineering* 4093 (Oct. 2000).

[62] Felix Bettonvil. “Fisheye Lenses”. In: *WGN, the Journal of the IMO* 33.1 (Mar. 2005), pp. 9–14.

[63] Mikhail Y. Shalaginov et al. “Single-Element Diffraction-Limited Fisheye Metalens”. In: *Nano Letters* 10.20 (Sept. 2020), pp. 7429–7437. URL: https://pubs.acs.org/doi/full/10.1021/acs.nanolett.0c02783.

[64] Luocheng Huang et al. "Long wavelength infrared imaging under ambient thermal radiation via an all-silicon metalens". In: *Optical Materials Express* 11.9 (Sept. 2021), pp. 2907–2913. URL: https://opg.optica.org/ome/fulltext.cfm?uri=ome-11-9-2907&id=456070.

[65] Vishwanath Saragadam et al. "Foveated Thermal Computational Imaging in the Wild Using All-Silicon Meta-Optics". In: *Arxiv* (Dec. 2022). URL: https://arxiv.org/abs/2212.06345.

[66] Qingbin Fan et al. "A high numerical aperture, polarization-insensitive metalens for long-wavelength infrared imaging". In: *Applied Physics Letters* 113.201104 (2018). DOI: 10.1063/1.5050562.

[67] Hung-I. Lin et al. "Wide-Field-of-View, Large-Area Long-Wave Infrared Silicon Metalenses". In: *ACS Photonics* 11.5 (2024), pp. 1943–1949. DOI: 10.1021/acsphotonics.4c00013.

[68] Fan Yang et al. "Wide field-of-view metalens: a tutorial". In: *Advanced Photonics* 5.3 (May 2023), p. 033001. URL: https://doi.org/10.1117/1.AP.5.3.033001.

[69] Deane Chandler-Horowitz and Paul M. Amirtharaj. "High-accuracy, midinfrared refractive index values of silicon". In: *Journal of Applied Physics* 97.123526 (Apr. 2005). URL: https://aip.scitation.org/doi/full/10.1063/1.1923612.

[70] Victor Liu and Shanhui Fan. "S4: A free electromagnetic solver for layered periodic structures". In: *Computer Physics Communications* 183 (May 2012), pp. 2233–2244.

[71] Amir Arbabi et al. "Miniature optical planar camera based on a wide-angle metasurface doublet corrected for monochromatic aberrations". In: *Nature Communications* 7 (Nov. 2016), p. 13682. URL: https://www.nature.com/articles/ncomms13682.

[72] Milton Laikin. "Wide Angle Lens Systems". In: *Proc. SPIE 0237, 1980 International Lens Design Conference* (Sept. 1980). URL: 10.1117/12.959125.

[73] Ehsan Arbabi et al. “Controlling the sign of chromatic dispersion in diffractive optics with dielectric metasurfaces”. In: *Optica* 4.6 (June 2017), pp. 625–632.

[74] Sajan Shrestha et al. “Broadband achromatic dielectric metalenses”. In: *Light: Science and Applications* 7.85 (Nov. 2018), pp. 2047–7538.

[75] Wei Ting Chen et al. “A broadband achromatic metalens for focusing and imaging in the visible”. In: *Nature Nanotechnology* 13 (Jan. 2018), pp. 220–226.

[76] Amir Arbabi et al. “Miniature optical planar camera based on a wide-angle metasurface doublet corrected for monochromatic aberrations”. In: *Nature Communications* 7 (2016), p. 13682.

[77] Shane Colburn, Alan Zhan, and Arka Majumdar. “Metasurface optics for full-color computational imaging”. In: *Science Advances* 4 (Feb. 2018).

[78] Haldun M. Ozaktas, Hakan Urey, and Adolf W. Lohmann. “Scaling of diffractive and refractive lenses for optical computing and interconnections”. In: *Applied Optics* 33.17 (June 1994), pp. 3782–3789.

[79] Luocheng Huang et al. “Full-Color Metaoptical Imaging in Visible Light”. In: *Advanced Photonics Research* 3.5 (Feb. 2022).

[80] Anna Wirth-Singh et al. “Wide Field of View Large Aperture Meta-Doublet Eyepiece”. In: *ArXiv Preprint* (2024).

[81] Jianghao Xiong et al. “Augmented reality and virtual reality displays: emerging technologies and future perspectives”. In: *Light Sci Appl* 10.216 (Oct. 2021). URL: https://doi.org/10.1038/s41377-021-00658-8.

[82] Chenliang Chang et al. “Toward the next-generation VR/AR optics: a review of holographic near-eye displays from a human-centric perspective”. In: *Optica* 7.11 (Nov. 2020), pp. 1563–1578. URL: https://doi.org/10.1364/OPTICA.406004.

[83] Kong-King Shieh and Der-Song Lee. "Preferred viewing distance and screen angle of electronic paper displays". In: *Applied Ergonomics* 38.5 (Sept. 2007), pp. 601–608. URL: https://doi.org/10.1016/j.apergo.2006.06.008.

[84] Zhaoyi Li et al. "Meta-optics achieves RGB-achromatic focusing for virtual reality". In: *Science Advances* 7.5 (Jan. 2021). URL: https://doi.org/10.1126/sciadv.abe4458.

[85] Zhaoyi Li et al. "Inverse design enables large-scale high-performance meta-optics reshaping virtual reality". In: *Nature Communications* 13.2409 (May 2022). URL: https://doi.org/10.1038/s41467-022-29973-3.

[86] Gun-Yeal Lee et al. "Metasurface eyepiece for augmented reality". In: *Nature Communications* 9.4562 (Nov. 2018). URL: https://doi.org/10.1038/s41467-018-07011-5.

[87] Elyas Bayati et al. "Design of achromatic augmented reality visors based on composite metasurfaces". In: *Applied Optics* 60.4 (Jan. 2021), pp. 844–850. URL: https://doi.org/10.1364/AO.410895.

[88] Augusto Martins et al. "Fundamental limits and design principles of doublet metalenses". In: *Nanophotonics* 11.6 (Feb. 2022), pp. 1187–1194. URL: https://doi.org/10.1515/nanoph-2021-0770.

[89] Benedikt Groever, Wei Ting Chen, and Federico Capasso. "Meta-Lens Doublet in the Visible Region". In: *Nano Letters* 8.17 (2017), pp. 4902–4907.

[90] Alan Zhan et al. "Low-Contrast Dielectric Metasurface Optics". In: *ACS Photonics* 3.2 (2016), pp. 209–214. DOI: 10.1021/acsphotonics.5b00660.

[91] William J. Mitchell et al. "Highly selective and vertical etch of silicon dioxide using ruthenium films as an etch mask". In: *Journal of Vacuum Science and Technology A* 4.39 (July 2021), p. 043204. URL: https://doi.org/10.1116/6.0001030.

[92] Alan Zhan et al. “Metasurface Freeform Nanophotonics”. In: *Scientific Reports* 7.1673 (May 2017). URL: https://doi.org/10.1038/s41598-017-01908-9.

[93] Junwei Li et al. “Largest aperture metalens of high numerical aperture and polarization independence for long-wavelength infrared imaging”. In: *Optics Express* 30.16 (2022), p. 28882. DOI: 10.1364/OE.462251.

[94] David A. B. Miller. “Why optics needs thickness”. In: *Science* 379.6627 (Jan. 2023), pp. 41–45. URL: https://doi.org/10.1126/science.ade3395.

[95] Rui Chen et al. “A hybrid solution for spatial light modulators with a large space-bandwidth product: opinion”. In: *Optical Materials Express* 8 (2023), p. 13.

[96] Dana Dudley, Walter M. Duncan, and John Slaughter. “Emerging digital micromirror device (DMD) applications”. In: *Proceedings Volume 4895, MOEMS Display and Imaging Systems* (2003).

[97] Jie Sun et al. “Large-Scale Silicon Photonic Circuits for Optical Phased Arrays”. In: *IEEE Journal of Selected Topics in Quantum Electronics* 20.4 (2014), pp. 264–278.

[98] Ho-Seok Ee and Ritesh Agarwal. “Tunable Metasurface and Flat Optical Zoom Lens on a Stretchable Substrate”. In: *Nano Letters* 16.4 (2016), pp. 2818–2823.

[99] Ghazaleh Kafaie Shirmanesh et al. “Electro-optically tunable multifunctional metasurfaces”. In: *ACS Nano* 14.6 (2020).

[100] Yifei Zhang et al. “Electrically reconfigurable non-volatile metasurface using low-loss optical phase-change material”. In: *Nature Nanotechnology* 16 (2021).

[101] Sajan Shrestha et al. “Multi-element metasurface system for imaging in the near-infrared”. In: *Applied Physics Letters* 122.20 (May 2023), p. 2001701.

[102] Cheng-Feng Pan et al. “3D-printed multilayer structures for high-numerical aperture achromatic metalenses”. In: *Science Advances* 9.51 (Dec. 2023).

[103] Anna Wirth-Singh et al. “Meta-Optics Triplet for Zoom Imaging at Mid-Wave Infrared”. In: *arXiv Preprint* (2024). URL: https://arxiv.org/abs/2407.11255v1.

[104] Vikram Dhar and Zafar Khan. “Comparison of modeled atmosphere-dependent range performance of long-wave and mid-wave IR imagers”. In: *Infrared Physics and Technology* 51.6 (2008), pp. 520–527. DOI: https://doi.org/10.1016/j.infrared.2008.05.001.

[105] Jianchao Zhang et al. “A Fully Metaoptical Zoom Lens with a Wide Range”. In: *Nano Letters* 24.16 (2024), pp. 4893–4899.

[106] *Optical design of a continuous zoom MWIR lens system with large field of view*. 1293505. SPIE, 2023.

[107] *MWIR continuous zoom with large range*. 77601X. SPIE, 2010.